ADVANCED REFLECTION SEISMIC STUDIES

OF PHASE I WEYBURN CO_2 SEQUESTRATION MONITORING

A Thesis Submitted to the

College of Graduate and Postdoctoral Studies

In Partial Fulfillment of the Requirements

For the Degree of Doctor of Philosophy

In the Department of Geological Sciences

University of Saskatchewan

Saskatoon

By

YICHUAN WANG

PERMISSION TO USE

In presenting this thesis in partial fulfilment of the requirements for a Postgraduate degree from the University of Saskatchewan, I agree that the Libraries of this University may make it freely available for inspection. I further agree that permission for copying of this thesis in any manner, in whole or in part, for scholarly purposes may be granted by the professor or professors who supervised my thesis work or, in their absence, by the Head of the Department or the Dean of the College in which my thesis work was done. It is understood that any copying or publication or use of this thesis or parts thereof for financial gain shall not be allowed without my written permission. It is also understood that due recognition shall be given to me and to the University of Saskatchewan in any scholarly use which may be made of any material in my thesis.

Requests for permission to copy or to make other use of material in this thesis in whole or part should be addressed to:

Head of the Department of Geological Sciences
Geology Building, 114 Science Place
University of Saskatchewan
Saskatoon, Saskatchewan (S7N 5E2)

OR

Dean of the College of Graduate and Postdoctoral Studies
116 Thorvaldson Building, 110 Science Place
University of Saskatchewan
Saskatoon, Saskatchewan (S7N 5C9)

ABSTRACT

Three-dimensional, time-lapse (TL) reflection seismic datasets and well logs collected for Phase I CO_2 sequestration project in Weyburn oilfield (southern Saskatchewan, Canada) are utilized for developing new approaches in three research areas: 1) estimation of seismic source waveforms, 2) evaluation of TL acoustic impedance (AI) variations for monitoring CO_2 propagation, and 3) rigorous modeling of seismic waves propagating through finely layered rock. All three study areas are interconnected and important for accurate analysis of seismic data and TL monitoring of this and other oil reservoirs undergoing fluid injection.

The first approach focuses on estimating the source waveforms from reflection seismic data, which is critical for evaluating accurate well-to-seismic ties as well as in other applications. A simple and effective method is proposed, based on iterative identification of the strongest and sparse reflections in seismic records, which allows estimation of source waveforms through an optimization approach, without well-log control and statistical hypotheses. The method allows correcting for coherent noise which seems to occur in stacked Weyburn data, consisting in (de)amplification and time shifts of the low-frequency components of the records. The method is tested on real and self-similar synthetic well-log models and applied to the Weyburn seismic data.

For the second topic, a post-stack waveform-calibration processing procedure is developed in order to achieve accurate consistency of TL datasets. Time shifts between the monitor and baseline records are also measured during this procedure, and an improved method for calculating the TL reflectivity differences is proposed. Further, instead of subtraction of the baseline and monitor AIs, TL AI variations are evaluated directly from the reflectivity differences and baseline AI. AI inversion is performed by an accurate and stable method using

the stacked reflection and well-log data, and also seismic velocities measured during data processing. The inverted time shifts and TL AI variations correlate with CO_2 distributions within the reservoir and allow estimating parameters of the reservoir.

In the third research area, a completely new approach to seismic wave modeling is proposed. Rigorous first-principle continuum mechanics is used instead of the conventional viscoelastic approximation. This modeling considers the existence of internal variables, body-force internal friction, and boundary conditions for internal variables. These factors are disregarded in the viscoelastic model, but they should cause dominant effects on seismic-wave attenuation and velocity dispersion in layered media. Numerical modeling of seismic wave propagation is performed in a model of the Weyburn Field. The resulting wavefield and seismic attenuation parameters are found to strongly depend on the internal boundary conditions between layers. Several types of quality (Q) factors are measured in the modeled synthetic waveforms.

ACKNOWLEDGEMENTS

No matter how, I should and also sincerely want to show my first and deepest gratitude to my supervisor Dr. Igor Morozov. I still remember clearly the scene of the first time that I met with Igor and the first talk with him in his office. Since then, for these almost five years of my PhD study and research at University of Saskatchewan, Igor would always be there to patiently offer timely help, informative suggestions and instructive guidance. I can deeply feel how much I have learnt with him during these years. I also recall my lack of experience in scientific research when I first started my PhD. However, luckily, I got the most responsible supervisor who is always passionate and rigorous in research, and motivated and guided me to overcome all the difficulties. I have set Igor as a model for myself since a long time ago. Maybe I will never have the chance, intelligence and ability to research that height as Igor, but I will always remind myself that how long the way that I still need to go and how many knowledge and skills that I still need to work hard to achieve in the future.

These years of PhD life at our department are just so great and amazing and I am also glad to know different other brilliant experts in different areas of Geoscience. I want to show my thanks to Dr. Zoltan Hajnal for the different nice talks and building and maintaining the SEG student chapter in our department, which also made me have the chance to apply different travel grant and education program from SEG. I would like to thank Dr. Jim Merriam, who is also on my thesis committee. His course about geophysics inversion which I took in the first year of my PhD indeed helps me a lot for my following research. I would also show my gratitude to the rest of my thesis committee: Drs. Alexey Shevyakov, Kevin Ansdell, and external examiner Kristopher Innanen (University of Calgary). I also thank Dr. Samuel Butler for being the

Committee Chair for my defense. For other people in our department, I thank Jinru Lin, Rafael Gonzalez and Sandor Sule for generously sharing their precious experience and thank all the students in our group for these years of learning and working together.

Life in Saskatoon is not always easy, sometimes just like the long and brutal winter at here. However, I was lucky enough and there are close friends helped me to go through it. I would specially thank Nancy Williams. Nancy always took good care of every student in our group and encouraged us about our study and research. Every year's Thanksgiving and Christmas, Nancy would prepare the best meal in my mind for us to celebrate, which helped me to avoid the loneliness and helplessness during each festival. I want to thank Xin Zhang for offering the nice and cozy place to live and his mother Xiuli Pan for making delicious food for us from time to time. I thank Fengrui Zhang, Tian Xia, Wanting Feng and other friends for the good time we have gone through together. I also just realized that nearly all my Saskatoon friends have "abandoned" me by starting their new life and careers in Calgary, Vancouver and other places. I wish I can as successful as you in the future and I also wish all of you all the best.

At last but not least, I want to show my sincere gratitude to my parents Jian Wang and Xiumei Wu. All these years, my parents would always firmly support me. I have owed them too much and since 2014, the total time that I have spent with them is just about two months. Dear father and mother, thank you so much. Without your substantial love and supports, I would never have the courage to start and finish this PhD. I also want to show my thanks to my dear love Siyu Ru. With you, life in Saskatoon has become much easier and no matter how and when I was anxious about my work and research, you always had the way to make me relax. Thanks so much for your understanding and helping me to become a better myself. I will do my best to give us the best life and take good care of you. I also wish the success of your PhD in the near future.

How I wish I could have another five years to continue the research with Igor at University of Saskatchewan, but time cannot go back and life needs to go on. Thanks again to all the people who have helped me during my PhD. I will keep on working hard in the future and I will not let you down.

TABLE OF CONTENTS

LIST OF TABLES

LIST OF FIGURES

SYMBOLS AND ABBREVIATIONS

Symbol	Definition
1-D	One-Dimensional
3-C	Three-Component
3-D	Three-Dimensional
AI	Acoustic Impedance
AVO	Amplitude Variation with Offset
BC	Boundary Condition
CDP	Common Depth Point
CMP	Common Midpoint
CO_2	Carbon Dioxide
DEVM	Dynamically-Equivalent Viscoelastic Model
DUT	Drained/Undrained Transitions
EI	Elastic Impedance
EOR	Enhanced Oil Recovery
FWI	Full-Waveform Inversion
GLS	Generalized Linear Solid
GSLS	Generalized Standard Linear Solid
KB	Kelly Bushing
NMO	Normal Moveout
REV	Reference Elementary Volumes
RI	Reflection Impedance
RMS	Root-Mean-Square
SLS	Standard Linear Solid
SNR	Signal-to-Noise Ratio
TL	Time-Lapse
VE	Viscoelastic
VSP	Vertical Seismic Profile
WIFF	Wave-Induced Fluid Flow
WIID	Wave-Induced Internal Deformation
WILFF	Local WIFF (Wave-Induced Fluid Flow)

WMMS	Weyburn-Midale Monitoring and Storage
ZD	Zero Deformation
ZP	Zero Pressure

CHAPTER 1

INTRODUCTION

This dissertation contains three advanced topics related to analyzing the seismic and well-log data from a carbon dioxide (CO_2) sequestration project in Weyburn oilfield in southern Saskatchewan, Canada. The topics are relatively independent and represent aspects of a very broad area of 3-D reflection data processing, modeling, interpretation for physical properties of the subsurface, and imaging subtle variations in physical properties during enhanced oil recovery and geological CO_2 sequestration. Broadly, the work continues a number of previous studies of the Weyburn project data at the University of Saskatchewan (Baharvand Ahmadi et al., 2011; Baharvand Ahmadi, 2016; Gao, 2016), In this dissertation, I explore three new subjects not included in these previous studies (listed in the order of significance for conventional seismic-data analysis):

I) Detecting CO_2 variations by inversion for 3-D, time-lapse Acoustic Impedance (AI) images;

II) Estimation of seismic source waveform, which can be used for accurate tying of seismic data to well logs and reflection data processing;

III) An innovative approach to seismic wave modeling in layered reservoir and non-reservoir rock.

The rationale for studying each of these topics and their relations to the broader seismic, CO_2 sequestration, and Weyburn-oilfield studies are briefly summarized below, and the specific

objectives are given in section 1.1. This dissertation is based on several publications (Wang and Morozov, 2016, 2017, 2018, 2019, submitted I, submitted II, and submitted III).

The time-lapse (TL) seismic method (topic I) above, described in Chapters 4 and 5 of this dissertation) is the most commonly used and most accurate geophysical tool for detecting variations of physical properties occurring within the subsurface over intervals of time. By repeating seismic surveys with close acquisition and processing parameters, TL seismic monitoring adds an extra dimensionality of time to the conventional two-dimensional (2-D) or three-dimensional (3-D) seismic surveys conducted only once. The TL time intervals can vary from days (in modern micro-earthquake monitoring using permanent source-receiver arrays) to several months or years, as in the case of the Weyburn project of this study. The TL seismic method is able to image the distributions of injected fluids (water, gas, steam, CO_2, etc.) within the subsurface and provides a spatially-continuous assessment of physical properties within the reservoir and/or CO_2 storage site. The first application of TL seismic monitoring to geological CO_2 sequestration was performed at the Sleipner Field in the North Sea, and soon after that, TL seismic imaging was conducted for the Weyburn Field of this study.

The application of TL reflection seismic monitoring to Weyburn reservoir (thin and firm carbonates) meets with substantial challenges, because the injection of CO_2 is expected to create only a few percent of P-wave velocity variations and only 1-2 ms of TL effects on reflection times, which is near the seismic-noise level (Lumley, 2010). In recent PhD studies at the University of Saskatchewan, Baharvand Ahmadi (2016) analysed TL vertical seismic profiling (VSP) records, and Gao (2016) used a number of methods for standard and TL imaging using three-component (3-C) 3-D reflection seismic data. The results from both of these authors showed promising TL signatures correlated with CO_2 injection patterns; however, it also seemed

that the detail of these correlations could be improved by using more accurate data processing and more sophisticated imaging. In order to improve these results, in this dissertation, I perform additional waveform calibration of monitor records in order to achieve an accurate consistency of stacked images, so that the changes due to CO_2 injection can be observed and analyzed. As an imaging approach, I selected the acoustic impedance (AI), and the TL variations of AI are directly related to the injected CO_2. For P-waves at normal incidence, the AI has a clear physical meaning of the product of rock density and wave velocity, and consequently it can be related to CO_2 content within rock. However, sufficiently accurate AI inversion and particularly evaluation of TL differences also requires some improvements of the existing methods, which are proposed in this dissertation. By using well-log data and seismic processing velocities, I develop AI and TL AI inversion approaches that overcome the lack of low-frequency information and scaling uncertainties, which are well-known in the conventional AI images.

Regarding topic II) above, as shown in this dissertation, the above waveform calibration of monitor records requires accurate tying the stacked seismic records to well logs. The well-to-seismic tying procedure requires accurate estimation of input source waveforms. In addition to tying well logs to reflection seismic sections, knowledge of seismic source waveforms is critical for many other types of seismic data analysis, such as deconvolution, forward modeling, and inversion of seismic wavefields. Depending on the expected accuracy, assumptions about the character of the source and wave propagation, and availability of well-log data, numerous source estimation techniques have been developed (see Introduction in Chapter 3). However, there still exists no universal solution to this problem. In this dissertation (Chapter 3), I develop a simple method, which (at least) for Weyburn records, allows accurate estimation of the source waveforms without well-log control and sophisticated statistical hypotheses.

Finally, in topic III) of this study, I consider seismic wave modeling in layered anelastic media. Although the application of this modeling is carried out specifically for the Weyburn reservoir, the method is general and should apply to all types of rock and materials, and it should have a significant impact in many applications of seismic waveform modeling. Numerous studies of this subject over the past 70 years and most of the existing seismic-modeling software are based on the so-called viscoelastic (VE) model. This model represents the anelasticity of any medium by a single frequency-dependent quality factor denoted Q. The concept of Q for Earth's solids is based on the so-called correspondence principle, which replaces all mechanical interactions within the medium with a hypothetical "material memory" in time. However, in a number of recent publications, for example, Morozov (2019) argued that the VE model is physically inaccurate and incomplete, and it generally incorrectly accounts for rock rheology and boundary conditions. In this dissertation (Chapter 6), I describe an alternate wave modeling method based on first-principle continuum (macroscopic) mechanics. I show that rigorous mechanics-based wave modeling in practical cases is feasible and relatively straightforward, but it requires knowledge of rock properties (physical parameters of internal friction) other than its Q-factors.

1.1 Objectives

Corresponding to the research scope and topics outlined above, the specific objectives and contributions of this study are as follows:

1) Proposing a simple and effective source-waveform estimation method by using only a single stacked reflection record and based on user-specified optimization criteria;

2) Developing a waveform-calibration processing flow for post-stack TL seismic data analysis. The objectives of this processing flow are:

   a. Achieving accurate consistency of stacked monitors and baseline datasets;

   b. Accurate measurement of time shifts and potentially other differential attributes between the baseline and monitor datasets;

   c. Evaluating TL reflectivity differences by using the results of waveform calibration;

3) Evaluating the TL acoustic impedance (AI) differences between monitor and baseline datasets. The specific tasks here are:

   a. Deriving a continuous interval-velocity model from stacking velocities measured during initial reflection data processing;

   b. AI inversion from seismic, velocity-model, and well-log data. This task includes deriving both the baseline AI and relative AI variations related to TL differences.

4) By using the AI and TL AI sections, interpreting and analyzing the variations in physical properties and the distribution of CO_2 and/or pressure within the reservoir.

5) Rigorous modeling of wave propagation within the layered Weyburn oil reservoir by first-principle continuum mechanics without VE approximations:

   a. Giving the differential equations and wavemode solutions for an arbitrary layered medium with non-VE phenomena;

b. Modeling wave transmission and reflection with several types of boundary conditions between the anelastic properties of the layers;

c. Illustrating several types of empirical *Q*-factors arising from the synthetic records modeled in the layered structure.

1.2 Structure of this Dissertation

This dissertation is organized as follows. In the present Chapter 1, I give the general introduction and outline the objectives of this study. Chapter 2 gives an overview of Weyburn CO_2 sequestration project, a summary of the geology of the Weyburn oilfield, and describes the available seismic and well-log datasets.

In Chapter 3, I introduce a new non-stationary source waveform estimation method (topic II) above) based on iterative identification of the strongest and sparse reflections in seismic records. The well-to-seismic tie built from the estimated source waveform is advantageous for accurately locating the reservoir zone of Weyburn Field in seismic data in this study.

Chapters 4 and 5 are devoted to the TL acoustic impedance (AI) topic I) above. In Chapter 4, I describe the waveform-calibration approach of TL seismic datasets and evaluate TL reflectivity difference by using the attributes measured during this waveform calibration. In Chapter 5, I describe an approach for obtaining AI variations from TL reflectivity differences and baseline AI. The AI variations calculated from this approach provide a clear analysis of the CO_2 distribution within the Weyburn oilfield.

In Chapter 6, I present the first-principle, mechanics-based seismic-wave modeling (topic III) above). Well logs from the Weyburn project are used in order to create a detailed model of

Weyburn reservoir and to evaluate viscoelastic (VE) and non-VE wave-attenuation effects in this realistic layered structure.

Each of the Chapters 3 to 6 contains an introduction to the specific topic and conclusions. Finally, in Chapter 7, I summarize the results of this dissertation, draw general conclusions and make suggestions for future research.

CHAPTER 2

DATA AND GEOLOGY OF THE STUDY AREA

This Chapter gives an overview of the Weyburn Project, geology of the Weyburn Field and the available seismic and well-log data in this study. The description of the seismic datasets is based on the following papers:

***Wang, Y.**, and I. B. Morozov, 2017, Time-lapse acoustic impedance variations after CO_2 injection in Weyburn field, 87th Annual International Meeting, SEG, Expanded Abstracts, 5890-5894, doi: 10.1190/segam2017-17752011.1.*

***Wang, Y.**, and I. B. Morozov, submitted II, Time-lapse acoustic impedance variations during CO_2 injection in Weyburn oilfield, Canada, submitted to Geophysics, accepted.*

 The texts and figures were modified and reformatted for inclusion in this dissertation.

2.1 Weyburn Geological CO_2 Sequestration Project

Weyburn oilfield is a field of 1.4 billion barrels located in southeastern Saskatchewan, Canada (Figure 2.1). This reservoir was discovered in 1954, and since the mid-1960s, it has been water-flooded as part of enhanced oil recovery (EOR). In October 2000, injection of CO_2 for geological storage and EOR was started by EnCana (presently Cenovus Energy), concurrently with a multi-disciplinary monitoring study called the International Energy Agency Greenhouse

Gas CO_2 Weyburn-Midale Monitoring and Storage project (hereafter WMMS project; White et al., 2004a).

The initial CO_2 injection rate at Weyburn is $2.69 \cdot 10^6$ m^3/day. By 2002, the rate increased to $3.39 \cdot 10^6$ m^3/day which includes $0.71 \cdot 10^6$ m^3/day of CO_2 recycled from oil production. By September 2007, about 9800 tonnes/day of CO_2 was being injected within the entire Weyburn unit (White, 2008). One of the primary goals of the WMMS project was to study and monitor the geological CO_2 sequestration by numerous techniques including single-component (1-C) and three-component (3-C) surface and vertical seismic profiling (VSP) seismic imaging. The WMMS project produced extensive 3-D time-lapse seismic datasets, including the baseline survey in 1999 and four monitor surveys in 2001, 2002, 2004, and 2007. Of these datasets, three 3-C 3-D surveys acquired in 1999, 2001, and 2002 (Phase I of the WMMS project) were available in this study (section 2.3).

After the completion of the WMMS project, another major CO_2 storage and monitoring project was started near Estevan, and it is currently ongoing. This project named Aquistore has been receiving CO_2 from SaskPower Boundary Dam Capture facility since 2015 (Aquistore Working Group, 2016). In the Aquistore project, CO_2 is injected into deep saline sandstone of about 3400 m with an injection-zone thickness of over 100 m. About 250–300 kilotonnes of CO_2 is anticipated to be received at the Aquistore storage site (White et al., 2016). Over 30 different geotechnical and geophysical technologies for monitoring and measurement were employed in this project including passive seismic, VSP, time-lapse reflection seismic with a permanent array, crosswell seismic, and other (Aquistore Working Group, 2016). The experience gained in the WMMS project was useful for formulating the methodology of Aquistore. Thus, I hope that the

results of the present dissertation may also contribute to Aquistore and and other CO_2 monitoring projects.

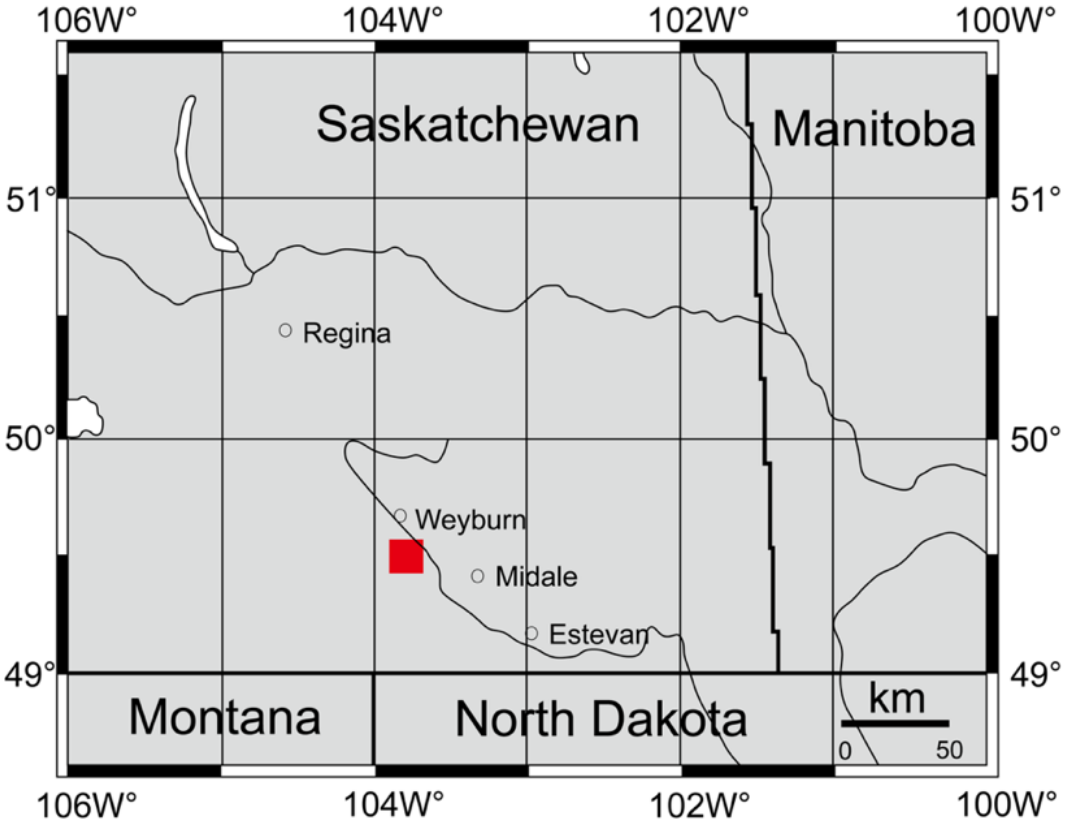

Figure 2.1. Location map of Weyburn oilfield (red square) in SE Saskatchewan, Canada.

2.2 Geology

The Weyburn Field covers an area of about 180 km^2 and is one of several large oilfields located along the Mississippian subcrop belt on the northeast flank of the intracratonic Williston Basin, which contains shallow marine sediments from the Cambrian to Tertiary age. Weyburn oil reserves lie within a thin zone (< 30 m) of fractured carbonates in the Midale Beds of the Mississippian Charles Formation (Figure 2.2a) at a depth of about 1450 m, which were deposited

in a shallow carbonate shelf environment. The reservoir is composed of vuggy limestone (8 to 22-m thick "Vuggy zone") and overlying marly dolostone (2 to 12-m thick "Marly zone"; Figure 2.2b). The Marly zone is sealed from above by anhydritic dolostones and anhydrites of the Midale Evaporite. The evaporite caprock impedes upward migration of the CO_2, which is also overlain by a series of aquitards, including the Lower Watrous Member, which forms the most extensive primary seal to the Weyburn system (White et al., 2004b). Below the Midale reservoir are the similar Frobisher Beds, which are also composed of carbonates overlain by evaporite deposit. Such evaporite is missing in the monitoring area (White, 2013). From core and imaging logs, it was determined that the dominant fracture set within the reservoir strikes NE-SW (Bunge, 2000), which is subparallel to the regional trajectories of maximum horizontal stress and also to the inlines of the CMP grid. Along with the small thicknesses of the reservoir zone, another important characteristic of the Weyburn-Midale reservoir is that the porosity of the Marly zone is high (29%) but its permeability is low (about 10 mD on average) whereas within the Vuggy zone, porosity is lower (about 10%) but the average permeability is high (about 50 mD) (Brown, 2002). Most oil production prior to the CO_2 injection focused on the Vuggy zone, but CO_2 is mainly injected into the Marly zone, with the horizontal injection wells generally located within this zone (Figure 2.2b, trajectory in red).

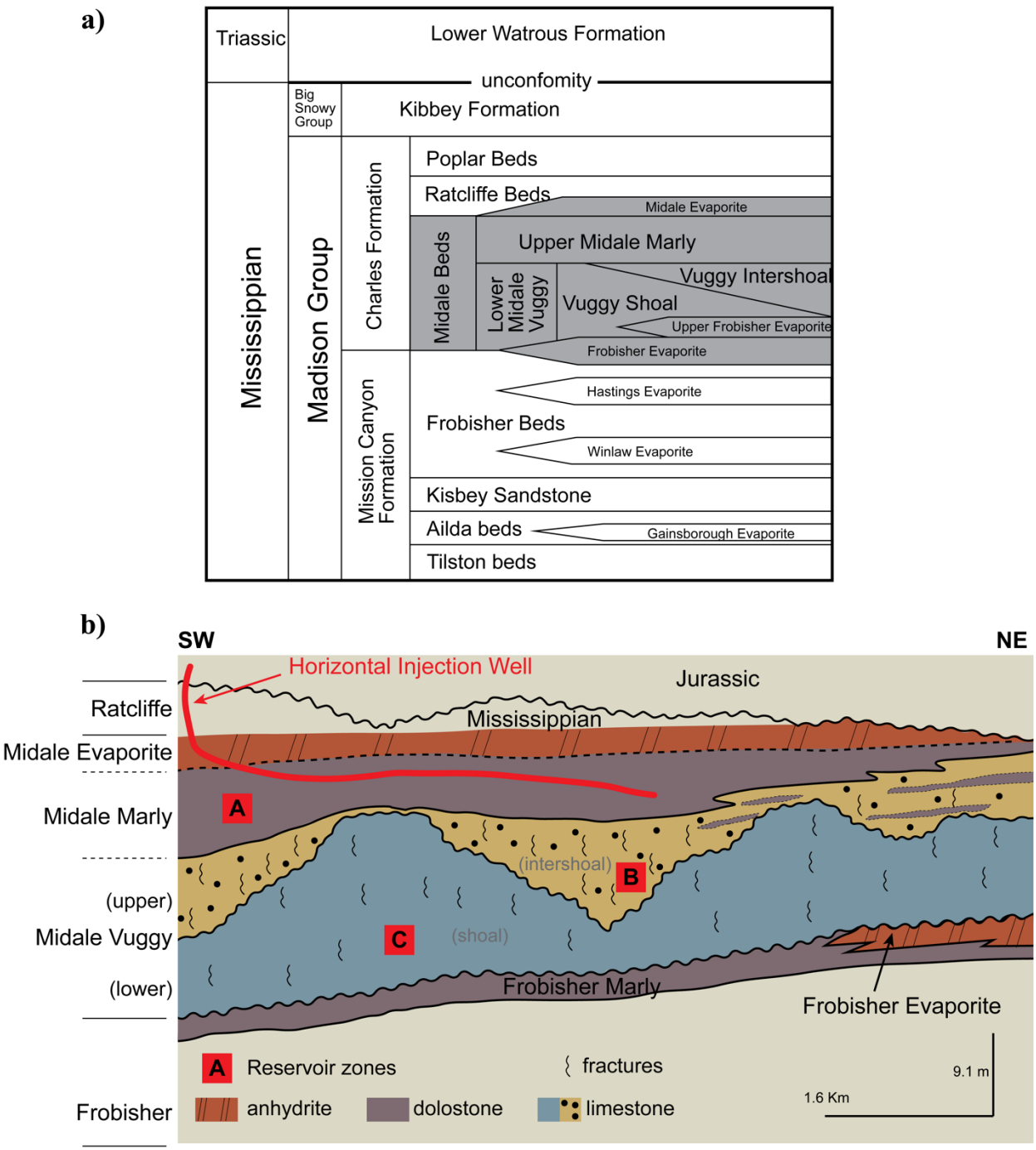

Figure 2.2. Schematic geology of Weyburn Field: a) Stratigraphic column (Modified after Wegelin, 1984); b) Major lithologies within the Midale reservoir (Modified after White et al., 2004a). Gray area in a) highlights the reservoir zone.

2.3 Time-Lapse Seismic and Well-Log Data

Five three-component (3-C) three-dimensional (3-D) reflection seismic datasets were acquired for the WMMS project: a baseline survey in December 1999 and monitor surveys in 2001, 2002, 2004, and 2007. These datasets were used to evaluate the feasibility of CO_2 sequestration and to monitor physical changes in the Weyburn Field caused by the CO_2 injection (White et al., 2004a; White, 2009; Ma and Morozov, 2010). Of these datasets, the baseline 1999 and monitors 2001 and 2002 datasets acquired during Phase I of the project (red rectangle in Figure 2.1) are available to the present study. These datasets were also used in the previous studies by Baharvand Ahmadi et al. (2011), Baharvand Ahmadi (2016), and Gao (2016).

The seismic acquisition consistency of Weyburn TL datasets is considered good (Table 2.1) due to careful survey design and close source-receiver configurations, although some differences in shot numbers and geophone types are still present, particularly for monitor 2001. Another significant difference between these TL datasets is in using MEMS geophones in 2002, which led to significant challenges for accurate amplitude and waveform calibration (Chapter 4). Figure 2.3 shows the shot and receiver-layout maps of the baseline 1999 dataset. Identical common midpoint (CMP) grids were used for the three vintages, each covering approximately 39.7 km^2, with 73 northeast-southwest inlines and 85 perpendicular crosslines (Figure 2.3b).

The 3-D/3-C data were initially processed by Gao (2016), and I re-processed them with Gao's trace edits, refraction statics and stacking-velocity picks. The processing was performed by using ProMAX software by Halliburton, and horizon picking, well-log analysis, and displays were performed by using OpendTect software by dGB Earth Sciences. The baseline 1999 and monitors 2001 and 2002 datasets were processed separately by using the same processing flows

and velocity models (Table 2.2). Figure 2.4 shows a crossline cross-section of the stacked seismic data of the baseline dataset, in which the key interpreted horizons are indicated. This cross-section (Figure 2.4) shows that the stacked seismic dataset is of high quality and resolution. At the same time, note that the entire reservoir zone occupies only about two dominant wave periods in these data, and therefore the requirements to accurate TL imaging are high.

In order to tie well to seismic and calculate the well-log calibrated AI, I use the P-wave velocity and density logs from well 102042300614 located near the SW border of Phase 1A area (green dot in Figure 2.3a). This well contains the most complete sets of geophysical logs (Figure 2.5) and is considered to be a representative of the reservoir. The P-wave velocity log is available from about 113 m to 2000 m from Kelly bushing (KB), whereas the density log is limited to the depth range from about 1349 m to 1439 m from KB (Figure 2.6). Rock-physics properties of rock specimens from this well were extensively studied by Brown (2002) in the laboratory.

Table 2.1. Seismic acquisition parameters of Weyburn monitoring project (Baharvand Ahmadi et al., 2011)

Parameters	**Baseline (1999)**	**Monitor (2001)**	**Monitor (2002)**
Number of shots	630	882	630
Number of receivers	986	986	986
Sample rate (ms)	2	2	2
Maximum offset (m)	2153	3446	2106
Source type	Dynamite, 1 kg, 12 m depth	Dynamite, 1 kg, 12 m depth	Dynamite, 1 kg, 12 m depth
Receiver type	Mitcham, 3-C, 10 Hz, Damping 70%	OYO, 3-C, 10 Hz, Damping 1%	I/O, VectorSeis, 3-C, MEMS
Source interval (m)	160	160	160
Receiver interval (m)	160	160	160
Swath	19 lines × 39 stations	19 lines × 39 stations	19 lines × 39 stations

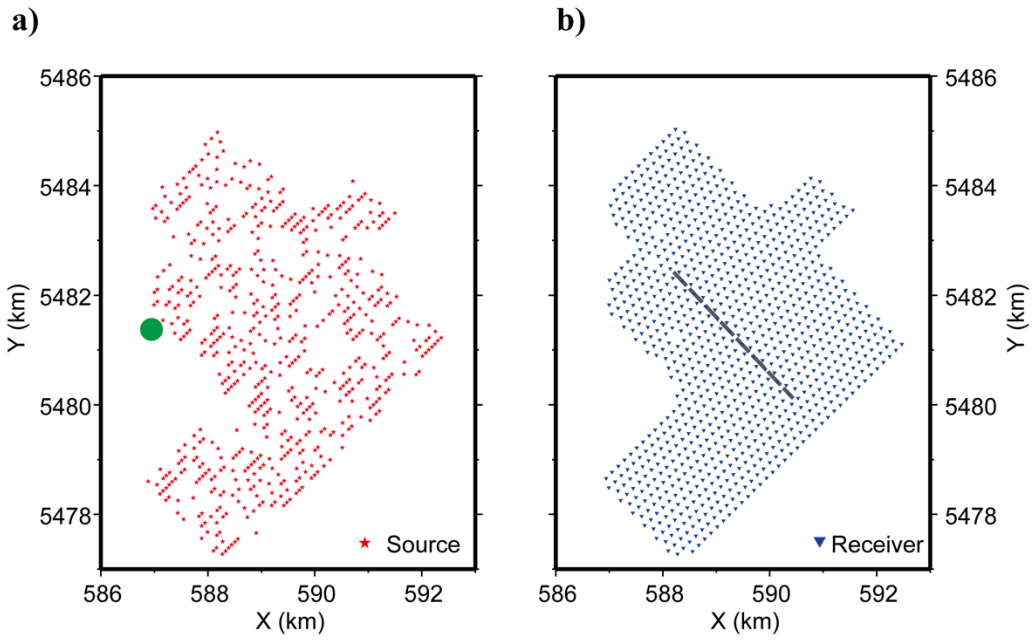

Figure 2.3. a) Source and b) receiver layouts for baseline 1999 dataset. Green dot in plot a) is the location of well 102042300614. Gray dashed line in plot b) shows the segment of crossline 40.

Table 2.2. Seismic processing flow for the baseline 1999 and monitors 2001 and 2002 datasets of Weyburn monitoring project.

Trace kill and mute
Refraction statics (common velocity model)
True amplitude recovery (spherical divergence)
Bandpass filter (single Ormsby bandpass, 0-3-90-100 Hz)
Minimum phase predictive deconvolution (110-ms decon operator, 90-ms prediction distance)
Minimum phase spiking deconvolution (90-ms decon operator length)
Time variant spectral whitening (100-ms spectral balancing scalar length, time-variant filter)
Trace equalization (root-mean-square (RMS) scaling)
Normal moveout correction (common stacking velocities)
Trace top muting
CDP stacking
Bandpass filter (time- and space-variant Ormsby bandpass)
F-X deconvolution

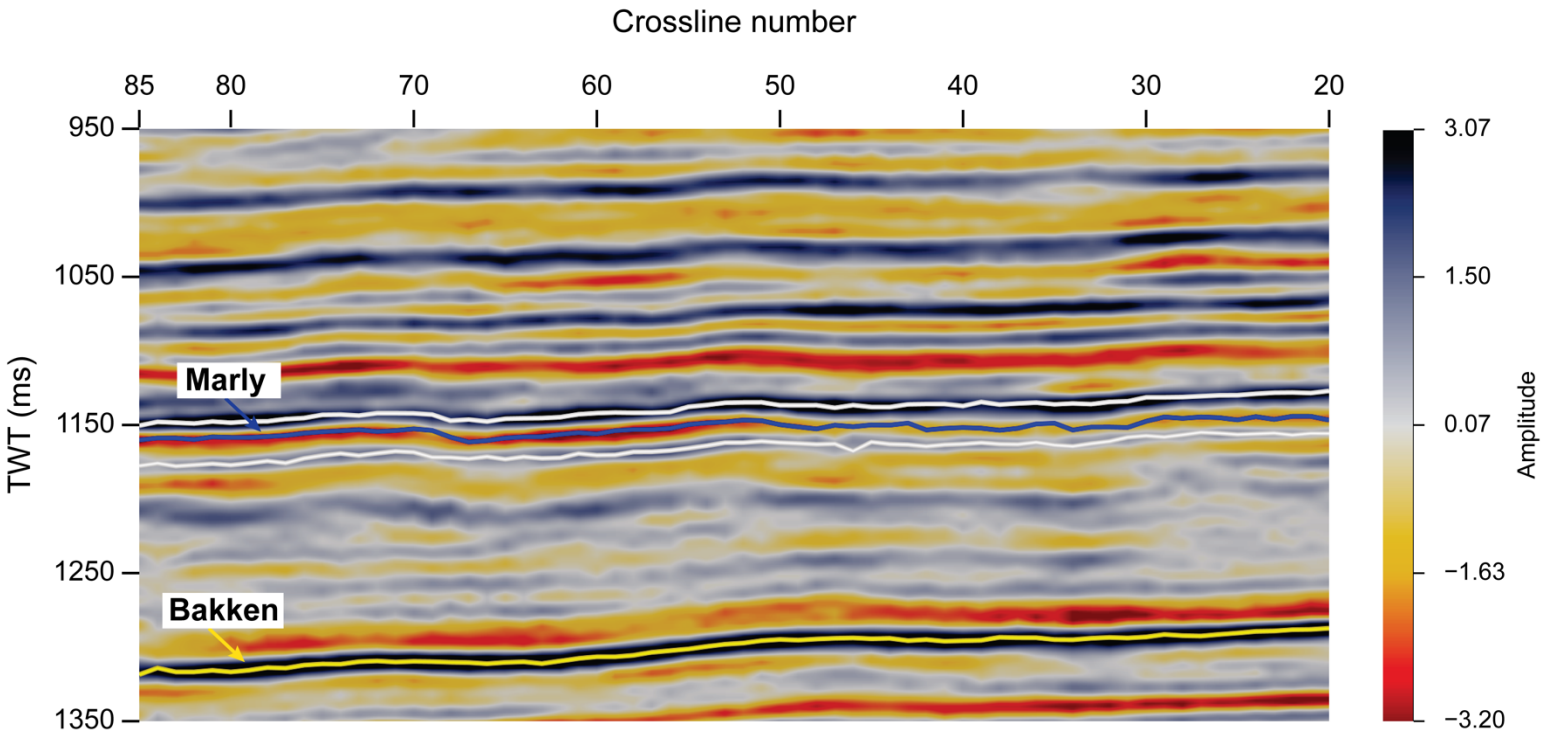

Figure 2.4. Seismic cross-section of baseline 1999 along inline 20: The caprock and bottom horizons of the reservoir zone (white lines), and Marly (blue line) and Bakken (gold line) horizons are indicated.

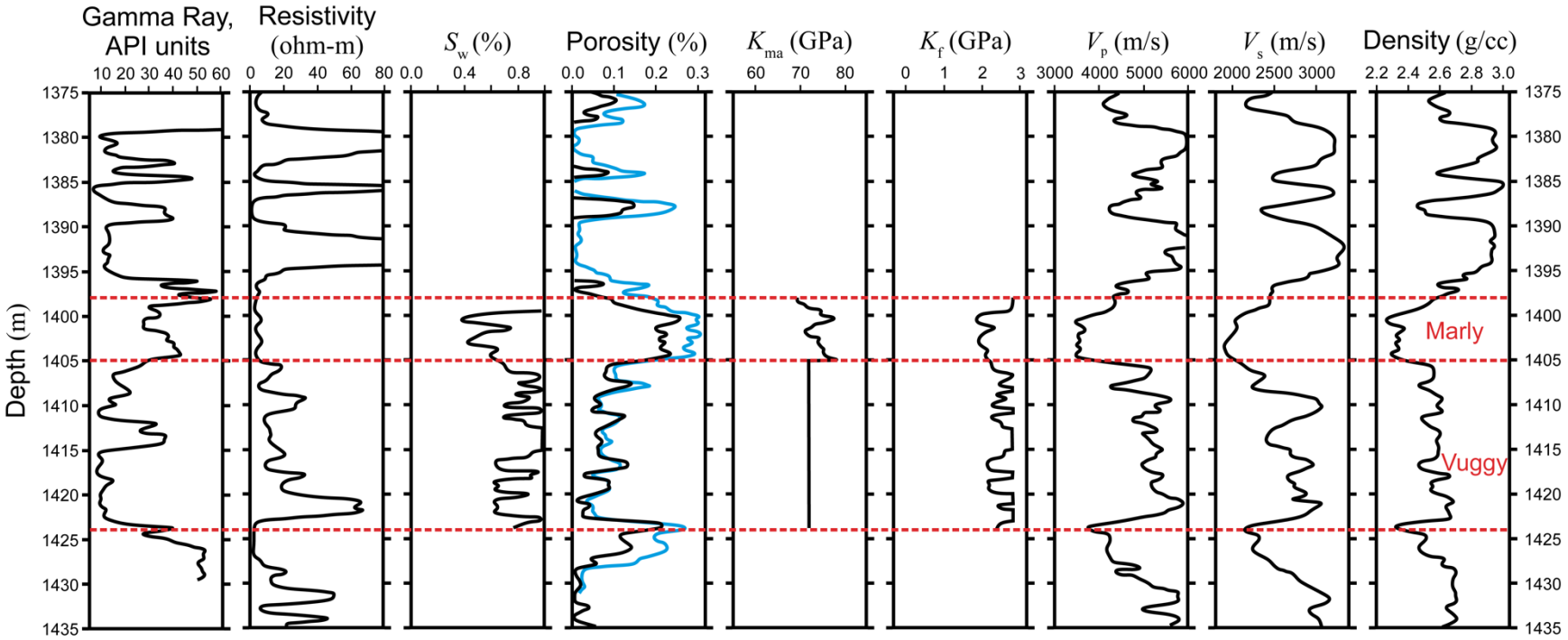

Figure 2.5. Geophysical logs in well 102042300614 (Baharvand Ahmadi et al., 2011). S_w denotes the water saturation. The total and effective porosities are respectively shown by blue and black curves.

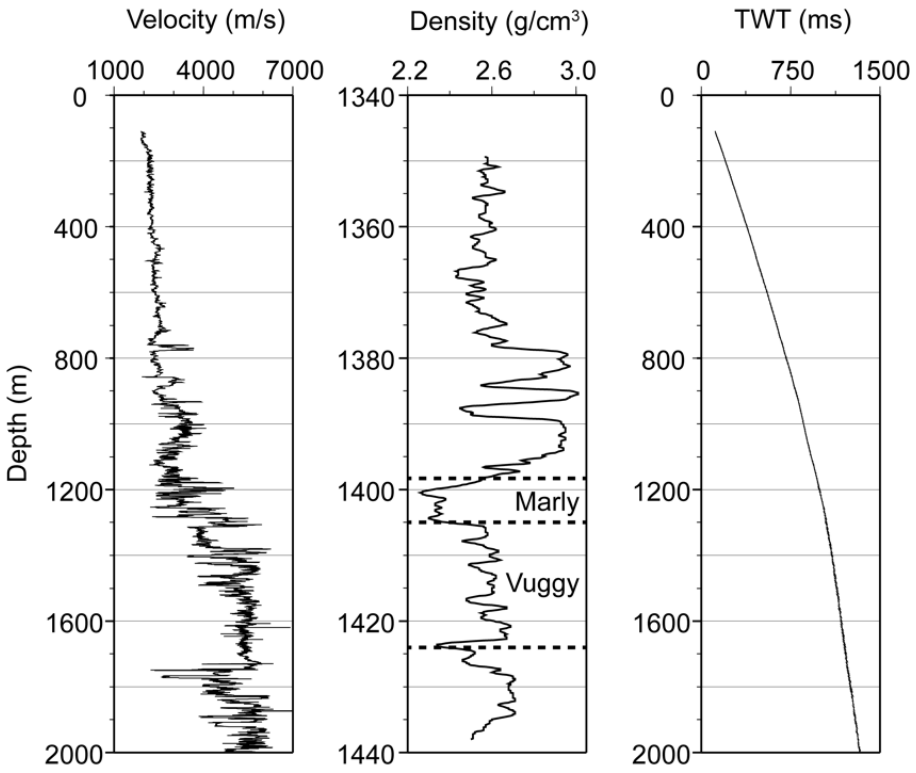

Figure 2.6. P-wave velocity (left) and density (middle) logs measured from well 102042300614, and the P-wave time-depth relationship (right) within this well. Reservoir zones are indicated in the density log.

CHAPTER 3

SOURCE WAVEFORM ESTIMATION

In this Chapter, I describe a simple non-stationary source-waveform estimation approach. Source waveform estimation is a basic step of many types of seismic data analysis, ranging from identifying major reflectors and fine layering to measuring attenuation and seismic-source properties. In this project, I employed the source estimation to perform accurate well-to seismic ties, which further helped locating the reservoir zone and further guide the data analysis. The presentation in this Chapter is based on the following papers:

***Wang, Y.**, W. Deng and I. B. Morozov, 2018, A simple wavelet-estimation approach for well-log to seismic tying: GeoConvention 2018, CSPG/CSEG/CWLS, Abstract, https://www.geoconvention.com/archives/2018/207_GC2018_A_Simple_Wavelet-Estimation_Approach_for_Well-Log%20to_Seismic_Tying.pdf.*

***Wang, Y.**, and I. B. Morozov, submitted I, A simple approach to non-stationary source waveform estimation in seismic records, submitted to Geophysics, in revision.*

 The texts and figures of the above papers were modified and reformatted for inclusion in this dissertation, and additional tests (section 3.4) were added. In the following section, I introduce the problem of source wave estimation, describe existing methods, and further outline the remaining sections of this Chapter.

3.1 Introduction

Some forms of source-waveform signatures are inherently present in all seismic recordings. Knowledge of seismic source waveforms is critical for many types of seismic data analysis, such as deconvolution, tying well logs to reflection seismic sections, and forward modeling and inversion of seismic wavefields. However, source wavelets are often difficult to measure and even to rigorously define. In the convolutional model (Ricker, 1953), the source waveform is defined in the far field (at the point of observation), as a filter that is convolved with the earth's impulse response to produce the observed seismic records. Because of the complexity of the near-field zone, wave attenuation and scattering, this far-field source signature cannot be measured directly and has to be determined from seismic data.

The principal difficulties of estimating the far-field source waveform from seismic data consists in differentiating it from the (generally) arbitrary character of the earth's response and in accounting for the effects of noise. In dealing with these difficulties, the existing methods for wavelet estimation can be subdivided into two broad groups: deterministic and statistical (Edgar and van der Baan, 2011). Deterministic methods (e.g., Danielson and Karlsson, 1984; Lines and Treitel, 1985; Buland and Omre, 2003) are based on known earth's responses (usually, reflectivities determined from well logs) and derive the source waveforms by minimizing the differences between the synthetic and observed seismograms. However, well logs are not always available, and their use for capturing the phase of the source waveform requires accurate well-log to seismic ties, for which the source wavelet is again essential. Due to the variability of the wells and effects of noise, and also variable accuracy of synthetic modeling, the resulting deterministic source waveforms may also be non-unique.

In this study, I propose a new wavelet-estimation method belonging to the statistical group. Statistical methods do not require well logs and estimate source waveforms from seismic data alone. Compared to the deterministic methods, there exists a much broader variety of statistical approaches depending on the assumptions made about the spectral properties of either the earth's filter or about the source waveform (e.g., Lines and Ulrych, 1977). Constraints on the source waveforms are often inferred from their expected zero-phase, minimum-phase, or near-constant phase characters (Longbottom et al., 1988; van der Baan, 2008). Alternatively, the unknown earth's response time series can be approximated by requiring its minimum-entropy character (Wiggins, 1978; Oldenburg et al., 1981; Sacchi et al., 1994) or assuming that it is stationary or pseudo-random (Robinson, 1957; Angeleri, 1983). An elegant statistical method (homomorphic deconvolution) extracts wavelets from the complex cepstrum of the recorded signal (Ulrych, 1971), assuming that the wavelet and seismic reflectivity occupy different portions of it. In another method based on statistical attributes, the source waveform is extracted by using the so-called fourth-order cumulants (Lazear, 1993; Velis and Ulrych, 1996), based on the assumption that the reflectivity series is a non-Gaussian, stationary and statistically independent random process. In further extensions of these methods (Dai et al., 2016), elements of deterministic methods such as local similarity (Fomel, 2007) are included; however, the reference traces used for this similarity are inferred from the envelopes of seismic records themselves, i.e. by another statistical hypothesis. With respect to the noise, both deterministic and statistical methods usually assume white stationary noise within the seismic frequency band.

For real seismic records, none of the above statistical assumptions are guaranteed and as a result, determination of the source phase is subject to assumptions about the properties of the source. Generally, the convolutional model shows that with any reasonable phase of the source

waveform, there should exist an earth response explaining the observed seismic data. In the approach of this paper, I recognize this inherent uncertainty of phase and focus on simplicity, stability, and practicality of the method. The method should (approximately) recover the amplitude spectrum and phase for earth's impulse response in which a certain percentage of the strongest pulses in any given time window are relatively sparse (section 3.2). This statistical property of the earth's response is further called the stronger-peak sparseness (SPS). Although this property is not mathematically formalized, it can be described as time separation between pulses progressively increasing for stronger pulses. Such sparseness of reflectors seems to be often present in observed well logs and realistic synthetics (sections 3.3, 3.4 and 3.7). Another aspect of the expected SPS property is that weaker impulse responses (multiples, effects of tuning, etc.) adjacent to the strongest ones are mutually incoherent and can therefore be suppressed by stacking.

The time-domain algorithm employing the above SPS property does not require any control from well logs and can also utilize additional information from interpreted reflections of interest. Further in section 3.2, a modification of the convolutional model is considered, in which the source signature is affected by coherent noise consisting in a (de)amplification of the low-frequency part of the signal. I observed this type of noise in the stacked sections from the Weyburn CO_2 sequestration study (shown in Chapter 4), which are used in data examples in this study, and such noise may also be present in other stacked land datasets. To correct for such noise, grid search is performed to obtain the optimum estimation result (section 3.2). In sections 3.3 and 3.4, the source-waveform estimation and coherent-noise reduction methods are tested with two variants of the waveform-estimation procedure. In section 3.5, the approach is applied to real seismic data from the Weyburn CO_2 sequestration dataset (Chapter 2). In this section, I

also illustrate a Q-compensation correction, showing that the method allows inversion for non-stationary source waveforms. In section 3.6, I explore an interesting new approach to Q estimation in reflection seismic records by using the source-waveform estimation approach. Finally, in section 3.7, a quantitative measure of the SPS property is briefly investigated for well-log and stacked reflection data.

3.2 Model and Method

According to the seismic convolutional model, the observed seismic trace $s(t)$ can be represented by a convolution of a seismic wavelet $w(t)$ with the earth's impulse response $r(t)$ (Ricker, 1953):

$$s = w * r + n, \tag{3.1a}$$

where '$*$' denotes the convolution operator, n is an additive (incoherent) noise, and t is the "local" time in the vicinity of the reflection time at this portion of the record (Morozov et al., 2018b). Note that the time series $r(t)$ contains the primary reflectivity as well as all multiples, mode conversions, attenuation, noise coherent with the signal, and also effects of filtering applied during seismic processing. In matrix form, equation (3.1a) can be written as

$$\mathbf{s} = \mathbf{W}\mathbf{r} + \mathbf{n}\,, \tag{3.1b}$$

where **s**, **r**, and **n** are columns and **W** is the (generally) nonstationary wavelet matrix. In matrix **W,** j^{th} column represents the wavelet at two-way refection time t_j. Denoting the number of samples in the wavelet by N_w, matrix **W** only contains N_w nonzero values near its diagonal. The objective of this study is to determine the waveform $w(t)$ or matrix **W** from signal $s(t)$ alone.

Once the $w(t)$ is estimated, inverse filtering would allow determining the reflectivity time series $r(t)$.

As with all statistical methods (section 3.1), factorization of the time series $s(t)$ into two series $w(t)$ and $r(t)$ requires certain assumptions about their properties. In this study, I only impose three simple and intuitive constraints on the $w(t)$ series by assuming that: 1) $w(t)$ is limited to a time interval $t \in \left[-T/2, T/2\right]$, where T is selected by the data interpreter, 2) $w(t)$ has a peak amplitude equal one at $t = 0$, and 3) the values of $w\left(t\right) = 0$ and its derivatives $w'\left(t\right) = 0$ at $t = \pm T/2$. The second of these constraints merely represents the selection of the time $t = 0$ within the waveform and its scaling. This scaling means that, for example, in order for the factor $r(t)$ (equation (3.1a)) to represent the seismic reflectivity, true-amplitude processing should be applied to the signal $s(t)$. In addition, an underlying assumption about the reflectivity $r(t)$ is that the largest-amplitude peaks in it are sparse. To utilize this sparseness, I consider only the strongest contributions from $r(t)$ separated by no less than a selected time interval denoted T_s. In practical measurements (next sections), this interval can be selected equal the dominant period of the records. In addition, similar to all other methods, I assume that the noise $n(t)$ (equation (3.1a)) is incoherent and its effects are suppressed by the statistical averaging included in the procedure.

With the above constraints, the inverse of equation (3.1a) for $w(t)$ is approximated by iteratively identifying a sparse set of strongest reflections in the seismic trace $s(t)$ and stacking their waveforms. This procedure is implemented by the following operations:

1) By using a group of identical overlapping time windows of a selected length T_1, tapered segments of $s(t)$ are extracted. Each of these windows is composed of a flat portion and two cosine-shaped ramps of equal durations. In each tapered record, the largest-amplitude (positive or negative) peak is identified. The subsequent peaks are selected so that they are not closer than T_s to any of the preceding picks, and the number of picks does not exceed a selected value N.

2) For each selected peak number i, its time is denoted by t_i and the amplitude A_i is normalized by the root-mean-square (RMS) amplitude (A_{rms}) of the tapered record segment:

$$\tilde{A}_i = \frac{A_i}{A_{\text{rms}}}. \tag{3.2}$$

Due to such normalization, the reflections selected within different time intervals of the seismic trace contribute to the resulting waveform $w(t)$ approximately equally.

3) For each peak i, I extract a record segment $s_i(t)$ of length T centered on the peak. These segments are aligned in time and stacked to produce the estimated source waveform:

$$w(t) = c_0 h(t) \sum_i \tilde{A}_i \operatorname{sgn}(A_i) \hat{F} s_i(t_i + t), \tag{3.3}$$

where sgn() is the signum function, and the summation is carried out over all peaks. An optional filtering operator $\hat{F}$ can be applied to the signal window $s_i(t)$ in equation (3.3). This filter can be used to apply weights to certain time and/or frequency intervals, or to correct for possible nonstationary source waveforms in equations (3.1). In the following,

two types of this filter are illustrated. Finally, a Hanning taper $h(t)$ of length T enforces the constraints $w(\pm T/2)=0$ and $w'(\pm T/2)=0$, and scaling factor c_0 is applied to achieve the peak amplitude equal $w(0)=1$.

Thus, only four easily interpretable parameters T, T_1, T_s, and N are required in the above procedure. The resulting estimate for $w(t)$ represents an application of a nonlinear inverse filter that I denote R^{-1}: $w = R^{-1} * s$. Note that although from equations (3.1), R^{-1} has the meaning of inverse reflectivity, it is not an inverse of the reflectivity series $r(t)$ within any time range but a combination of the largest-amplitude reflectivities as described by the procedure 1)–3). This estimation procedure is further illustrated in Figure 3.1.

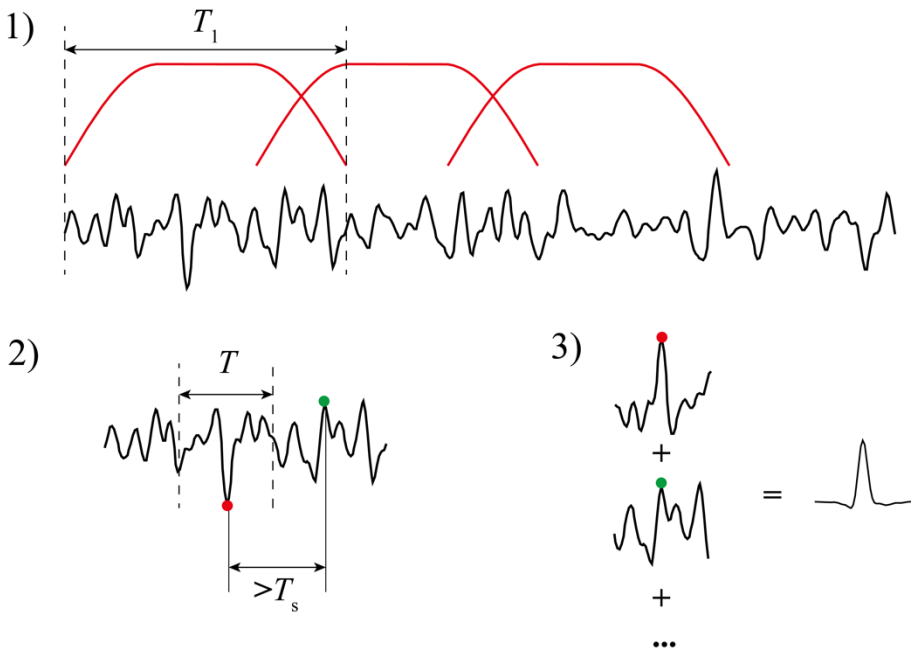

Figure 3.1. Source-waveform estimation procedure: Red curves in 1) are the overlapping time windows and black curve is the seismic trace $s(t)$. Red and green dots in 2) are the automatically selected largest-amplitude peaks. Extracted record segments are aligned and stacked in 3) to obtain the estimated $w(t)$ (lower right).

The time-variant filtering operator $\hat{F}$ in equation (3.3) depends on the data and expected types of waveform non-stationarity. Seismic attenuation and dispersion represent a typical cause of such non-stationarity likely present in many datasets. In such cases, $\hat{F}$ would include an inverse-Q filtering operator $\hat{F} = \hat{A}^{-1}$, where $\hat{A}$ is the attenuation operator parameterized by the Q-factor or t^* along the wave path. In matrix notation of equation (3.1b). the meaning of operator $\hat{A}$ consists in transforming the constant (true, stationary) far-field source waveform $\mathbf{w}_0$ into the attenuated waveform $\mathbf{w}$ as $\mathbf{w} = \hat{A}\mathbf{w}_0$ (Morozov et al., 2018b). For a frequency-independent Q, in the frequency domain, operator $\hat{A}$ consists in a multiplication of Fourier components of $\mathbf{w}_0$ by (Aki and Richards, 2002)

$$A(\omega, t^*) = \exp\left(-\frac{\omega}{2}t^*\right)\exp\left(-i\frac{\omega}{\pi}t^* \ln\frac{\omega}{\omega_r}\right), \tag{3.4}$$

where $t^* = \int_0^t Q^{-1}(\tau)\,d\tau$, t is the observation time, ω is angular frequency, and ω_r is the reference frequency, which is set equal the dominant frequency of the extracted record $w_0(t)$ (Morozov et al., 2018b). The first exponential factor in equation (3.4) describes the amplitude decay due to attenuation, and the second is the corresponding phase dispersion. The resulting Q-compensation filter applied to i^{th} trace window ($s_i(t)$; equation (3.3)) is therefore $F(\omega, t_i) = 1/A(\omega, t_i)$.

As usual when applying filters in the frequency domain, $F(\omega, t_i)$ is multiplied by the positive-frequency component ($S_i(f)$; equation (3.3)), which is below the Nyquist frequency. The negative-frequency part of the filtered signal (or above the Nyquist frequency) is obtained by the frequency-folding, or conjugate symmetry relations $\mathrm{Re}\,S_i(-f) = \mathrm{Re}\,S_i(f)$ and

$\mathrm{Im}\,S_i(-f) = -\mathrm{Im}\,S_i(f)$. This form of the filter guarantees that the output is a real-valued time series after the inverse Fourier transform. For larger values of ω and t_i, the Q-compensation filter $F(\omega, t_i)$ is regularized by restricting its maximum gain, as described by Wang (2008). As a result of included inverse Q filtering, the algorithm derives an estimate of the attenuation-independent source waveform $w_0(t)$.

Clearly, the use of the Q-compensation operator in equation (3.3) is consistent with conventional post-stack reflection data processing, in which Q-compensation is applied first, and waveform estimation is performed assuming an elastic medium. However, inclusion of Q-compensation (and other optional filtering) in the present source waveform analysis (equation (3.3)) is natural and offers additional benefits. In particular, this inclusion simplifies the data processing flow and in some cases yields independent estimates of the Q (section 3.6). As it is currently the common practice, for best results, Q-compensation should be performed at the end of imaging, as part of migration or full-waveform inversion.

In addition to attenuation, our experience with several land datasets suggests that stacked reflection data sometimes contain time-variant enhancement of the low-frequency signal below certain frequency, which we denote f_0 and estimate from seismic data processing (about 15 Hz in the dataset in section 3.5). Such relative low-frequency amplification can be treated as coherent (signal-related) noise. This noise can be caused by many reasons, such as inaccuracies of the velocity and residual-statics models and contributions from incompletely cancelled ground roll. If gradational zones or fine layering is present in a real reflection sequence, the low- and high-frequency reflections may occur at somewhat different times, which may be variable with depth and unknown *a priori*. Therefore, we can generally expect observing time-variant scaling and

time shifts between the low- and high-frequency parts of the records. Removing these effects would help improving the source wavelet and broadening its spectrum.

To correct for such potential undesirable effects, I consider a modification of the forward model (equation (3.1a)), in which the low-frequency component of the seismic trace is affected by an amplification factor a and an unknown time-shift filter ΔT acting below some frequency f_0:

$$s = \left(a\Delta T * F_{<f_0} + F_{>f_0} \right) * w * r + n, \tag{3.5}$$

where $F_{<f_0}$ is the zero-phase low-pass filter with a cosine-shaped transition from the response equal one at frequency $f < f_0$ to zero at $f > f_0$. Similarly, $F_{>f_0}$ denotes the zero-phase high-pass filter equal $F_{>f_0} = 1 - F_{<f_0}$ in the frequency domain.

Similar to the case of Q-compensation (equation (3.4)), filtering operator $\hat{F}$ (equation (3.3)) can be defined as an inverse of the operator in the parentheses in equation (3.5). However, as shown in sections 3.3 and 3.4 below, the resulting waveforms have a relatively weak sensitivity to parameter a and the time shift in filter ΔT, and consequently these parameters cannot be accurately inverted for in the presence of noise. Therefore, we perform the waveform optimization differently, without explicitly evaluating filters $\hat{F}$ and determining parameters a and ΔT. Depending on whether the unknown time shift (ΔT in equation (3.5)) is considered significant, two wavelet estimation procedures can be proposed. These procedures are denoted as *Estimation A* and *Estimation B* and consist in the following operations.

Estimation A

If the unknown time shift between the low- and high-frequency parts of the signal is significant, we cannot measure them but can only try achieving an optimal shape of the output wavelet while considering a range of possible frequencies f_0 and amplitude scalars a in equation (3.5).

To obtain such an optimal wavelet, I approximate the recorded signal as $s(t) = s_{\text{low}}(t) + s_{\text{high}}(t)$ in the convolutional model (3.5), where the low- and high-pass filtered records are $s_{\text{low}} = F_{<f_0} * s$ and $s_{\text{high}} = F_{>f_0} * s$, respectively. By using each of the frequency components $s_{\text{low}}(t)$ and $s_{\text{high}}(t)$ separately, as described above, I produce wavelet estimates $w_{\text{low}} = R^{-1}(s_{\text{low}}) * s_{\text{low}}$ and $w_{\text{high}} = R^{-1}(s_{\text{high}}) * s_{\text{high}}$. The resulting wavelet estimate is then got by using an additional weight factor c (Figure 3.2a):

$$w_{\text{est}} = c \cdot w_{\text{low}} + w_{\text{high}}, \tag{3.6a}$$

and scaled to satisfy the normalization requirement $w_{\text{est}}(0) = 1$. Finally, parameters f_0 and c are obtained by an optimization procedure (grid search) described below.

Estimation B

If there is no time shift between the low- and high-frequency signal components, then filter $\Delta T(t)$ in equation (3.5) would equal $\delta(t)$ (Dirac delta function). In this case, I design a filter $F_1 = c \cdot F_{<f_0} + F_{>f_0}$ correcting for the low-frequency enhancement in model (3.5). This filter F_1 is

applied on the recorded signal: $s_1 = F_1 * s$, where $s_1(t)$ would be the low-frequency corrected signal. The resulting wavelet $w(t)$ is estimated from this corrected $s_1(t)$ (Figure 3.2b):

$$w_{\text{est}} = R^{-1}(s_1) * s_1, \tag{3.6b}$$

and also time-shifted and scaled to satisfy the normalization requirement $w_{\text{est}}(0) = 1$. As in *Estimation A*, parameters f_0 and c are obtained by an optimization procedure.

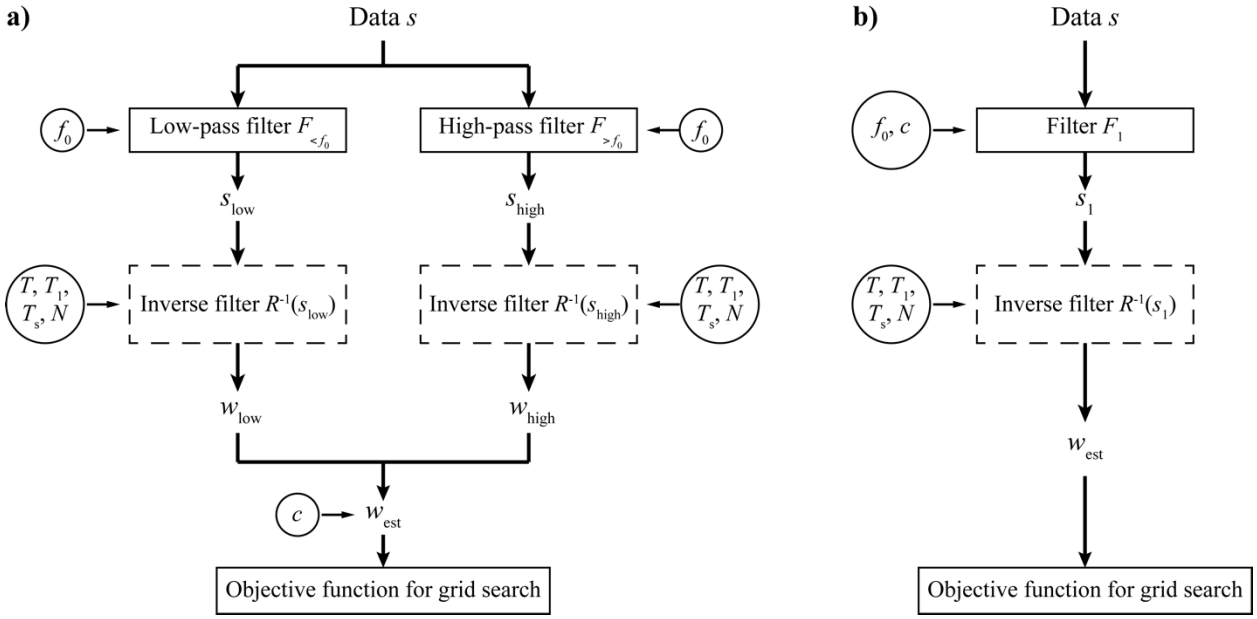

Figure 3.2. Flow charts for procedures of a) *Estimation A*, and b) *Estimation B*. Circles indicate parameters of the different steps of the procedure.

Evaluation of relations (3.6) requires selecting parameters f_0 and c. For both *Estimation A* and *Estimation B*, I determine parameters f_0 and c not as an inversion for the parameters of equation (3.5) but by an optimization procedure seeking to improve the shape of the final

waveform $w_{\text{est}}(t)$ or of its spectrum. As a criterion of waveform quality in this optimization, I minimize the following objective function:

$$\Phi(c, f_0) = \overline{\tau}(c, f_0) + b\overline{Y}(c, f_0), \tag{3.7}$$

where b is a weight factor, overbars for quantities $\tau(c, f_0)$ and $Y(c, f_0)$ denote some normalization procedures (described in the next paragraph), $\tau(c, f_0)$ denotes the time between zero crossings of the main lobe in the resulting waveform $w_{\text{est}}(t)$ (equations (3.6)), and $Y(c, f_0)$ is some measure of the distribution of its side lobes. In the following section, I use two types of such measures: (1) the RMS of all side-lobe amplitudes, or (2) the proximity of the waveform $w_{\text{est}}(t)$ to its minimum-phase counterpart. The second of these measures is derived in Appendix A. Thus, depending on the selected measure $Y(c, f_0)$, I consider two types of optimization:

1) The optimal wavelet would combine the narrowest main lobe with the smallest side lobes. This selection is referred to as the "width-amplitude" optimization in the next sections.

2) The search for the narrowest main lobe is combined with approximating the minimum-phase shape of $w_{\text{est}}(t)$. This approach is called the "width-phase" optimization below.

The first of the above measures seems advantageous in the general cases of unknown phase or zero-phase transformed data, and the second option could be useful when a causal source waveform (such as representing a dynamite source) is required. For the case of setting $b = 0$, the optimization procedure would only focus on minimizing the width of the main lobe.

To equalize the contributions from the two measures of waveform quality, each of them is demeaned and normalized in the objective function (3.7) as follows (for example, for quantity $Y(c, f_0)$):

$$\overline{Y_i} = \frac{Y_i - \mathrm{med}\{Y\}}{\mathrm{med}\left\{\left|Y_i - \mathrm{med}\{Y\}\right|\right\}}, \tag{3.8}$$

where i denotes one pair of trial values of f_0 and c, $\overline{Y_i}$ is the resulting objective-function measure, and $\mathrm{med}\{Y\}$ denotes the median value of quantity Y_i over all trials. After such scaling, all quantities $\overline{Y_i}$ become dimensionless, have zero median values, and are scaled so that their median absolute values equal one. Therefore, the factor b for such normalized values in equation (3.7) should also be of about one. With parameter b selected, the objective function (equation (3.7)) is evaluated and the optimization is performed by using grid search with respect to parameters f_0 and c.

In the following sections 3.3 and 3.4. several synthetic and real-data applications of this procedure are shown. Since the time shifts ΔT appear to be present in the stacked Weyburn dataset records, the *Estimation A* procedure appears to be more reliable (sections 3.3). This procedure produces good waveform estimates, and it was reported in the paper by Wang and Morozov (submitted I). The more stringent *Estimation B* procedure (section 3.4) seems less successful in several application examples, and it is shown here for the sakes of completeness and discussion.

3.3 Tests and Examples using *Estimation A*

In this section, I use the waveform-optimization procedure *Estimation A* in section 3.2 to estimate the wavelet from synthetic 1-D datasets. By using synthetic data, the resulting estimated wavelet $w_{\text{est}}(t)$ can be compared to the one used for data generation, which allows evaluating the performance of the method. In the following subsections, synthetic-data tests of the wavelet-estimation method are conducted with a maximum number of $N = 3$ peaks located within each signal window of length $T_1 = 300$ ms, and the extracted waveform window length $T = 100$ ms. The values of parameter T_s were determined from the dominant period of each of the input seismograms and range from 18 to 22 ms. In most examples, the objective function (3.7) is evaluated by taking $b = 1$, unless indicated specifically.

To form the synthetic data, I use real (subsection 3.3.1) or synthetic (subsection 3.3.2) well logs (time series) consisting of P-wave velocities and use the Gardner equation (Gardner et al, 1974) to estimate the density and normal-incidence reflectivity series $r(t)$. By using this reflectivity, the noise-free seismogram $s(t)$ is simulated by equations (3.1) or (3.5) by taking $n(t) = 0$ and using modifications of the 40-Hz Ricker wavelet as $w(t)$.

3.3.1 Real well-log model

Figure 3.3 shows the acoustic well log from well 102042300614 (Figure 2.6) in the Weyburn oilfield (Chapter 2), and synthetic reflection seismograms built from it by using the Ricker source wavelet and two of its modifications: a 90° phase-rotated Ricker wavelet and a minimum-phase (minimum-delay) equivalent. To simulate the low-frequency coherent-noise effect described in section 3.2, the synthetic seismograms are filtered by multiplying the

amplitudes below frequency $f_0 = 15$ Hz by factor $m = 1.5$. If the described wavelet-estimation method can remove such low-frequency amplification, the optimal cut-off frequency from grid search (f_0 in equation (3.7)) would equal this selected f_0, and the optimal parameter c in equation (3.7) would equal $1/m \approx 0.67$. For the following tests, grid search is performed for c ranging from 0 to 2 and trial f_0 values ranging from 5 Hz to 40 Hz (approximately the dominant frequency of the input wavelet).

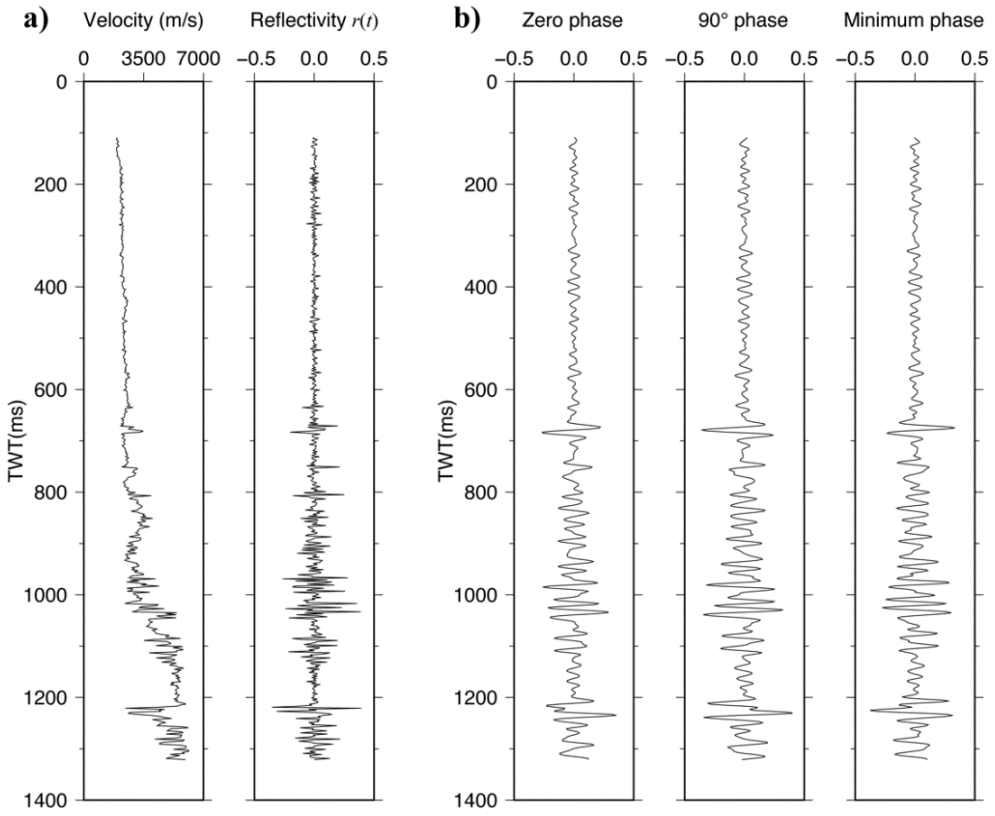

Figure 3.3. Synthetic models based on Weyburn-oilfield well logs: a) P-wave velocity and reflectivity series; b) Synthetic seismograms modeled by using the standard zero-phase, 90°-phase, and minimum-phase Ricker wavelets (labels).

For the cases of zero-phase and 90° input Ricker wavelets (Figure 3.3b), the procedure of wavelet estimation by the "width-amplitude" optimization is shown in Figure 3.4. In both cases, the parameters f_0 and c corresponding to the minimum of the objective function (equation (3.7))

are close to the expected values (dots in Figure 3.4), showing that this method corrects for the low-frequency inaccuracies of the input seismogram reasonably well. However, note the significant uncertainty of the optimal parameters (roughly the sizes of gray-color areas in Figure 3.4). This uncertainty means that the estimated waveform is only weakly sensitive to parameters f_0 and c, and this method can hardly serve as an accurate inversion procedure for the forward problem in equation (3.5). At the same time, this low sensitivity to model parameters shows that the resulting waveform $w(t)$ is stable, which is a highly desirable feature of the waveform-estimation approach. Figure 3.5 shows the waveforms and amplitude spectra of the optimal extracted $w_{\text{est}}(t)$ for the two types of input source wavelets. Note that the spectral signatures and upper-frequency cutoffs of the estimated wavelets are close to those of the input seismograms (Figure 3.5, right). The estimated wavelets are non-zero mean, and consequently they show broader bands toward low frequencies. From the viewpoint of seismic interpretation, the estimated wavelets may (arguably) be even more preferable and closer to seismic-source signatures than the modeled Ricker wavelets.

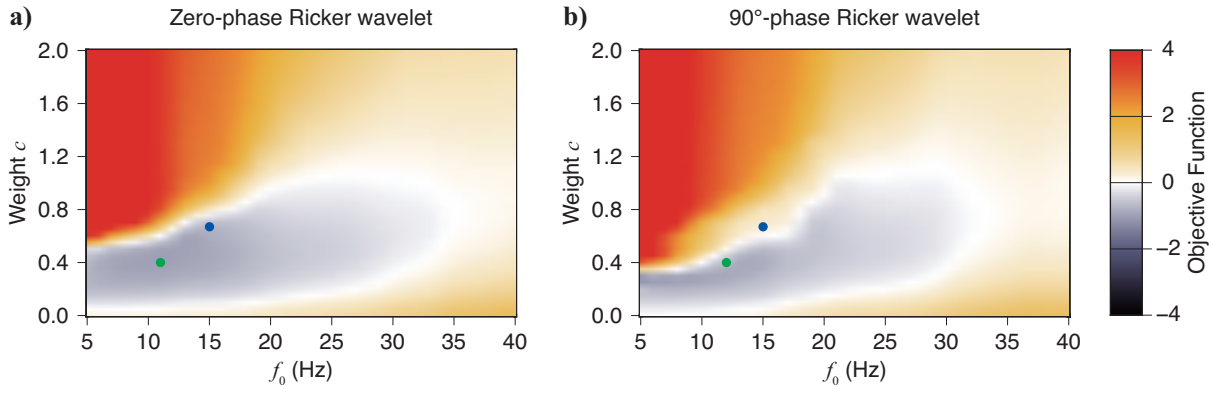

Figure 3.4. Values of the objective function during "width-amplitude" optimization (equation (3.7)) for: a) synthetic seismogram built using the zero-phase Ricker wavelet and b) using the 90°-phase Ricker wavelet (Figure 3.3b). Green dots indicate the optimum c and f_0 parameters, and blue dots are the expected values f_0 = 15 Hz and c = 0.67.

Another modification of this test example consists in changing the objective-function parameter b in equation (3.7) from $b = 1$ to $b = 0.43$ or 2.33. Figure 3.6 shows that such variations of b affect the resulting $w_{\text{est}}(t)$ only slightly. The source waveform optimized by using $b = 2.33$ has a slightly wider main lobe and lower side-lobe amplitudes compared to the results of selecting $b = 0.43$. This difference is expected, because the objective function with smaller b (equation (3.7)) favors the waveforms with narrower main lobes more strongly.

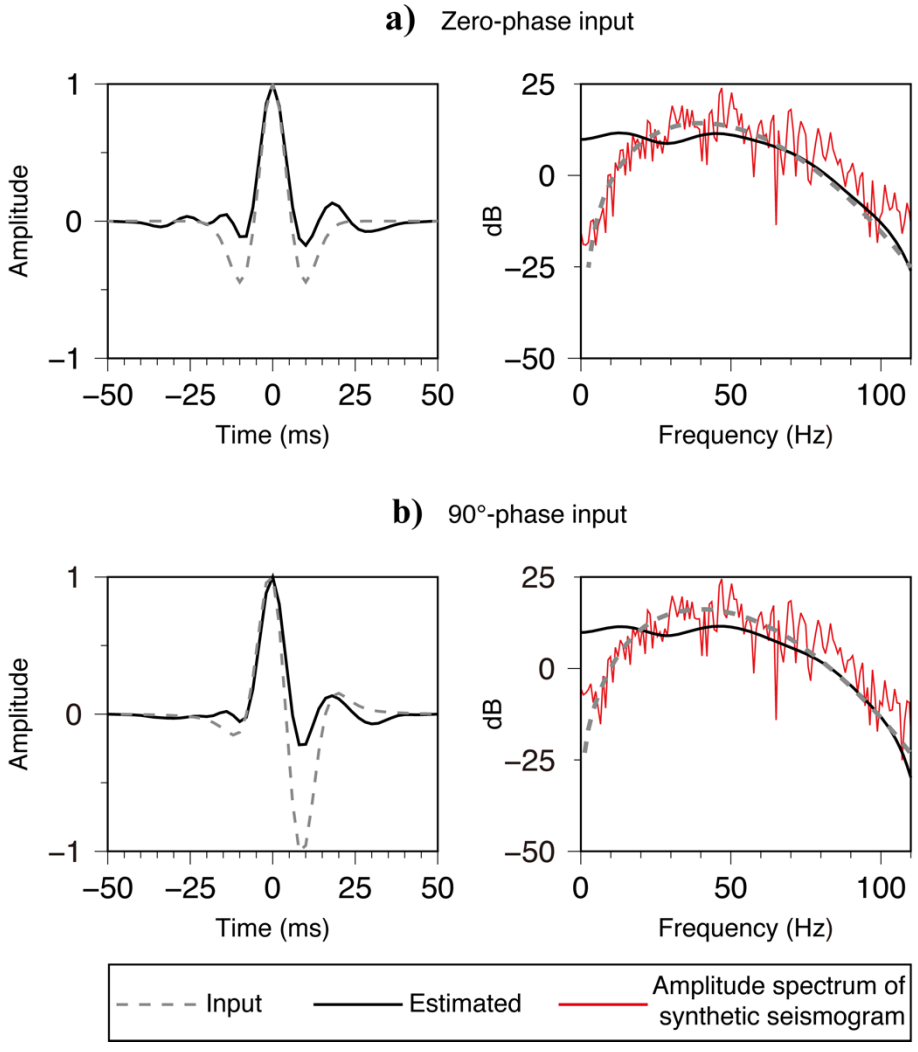

Figure 3.5. Waveforms (left) and amplitude spectra (right) for the input and estimated source waveforms (legend): a) for Ricker input wavelet and b) for 90° rotated input Ricker wavelet.

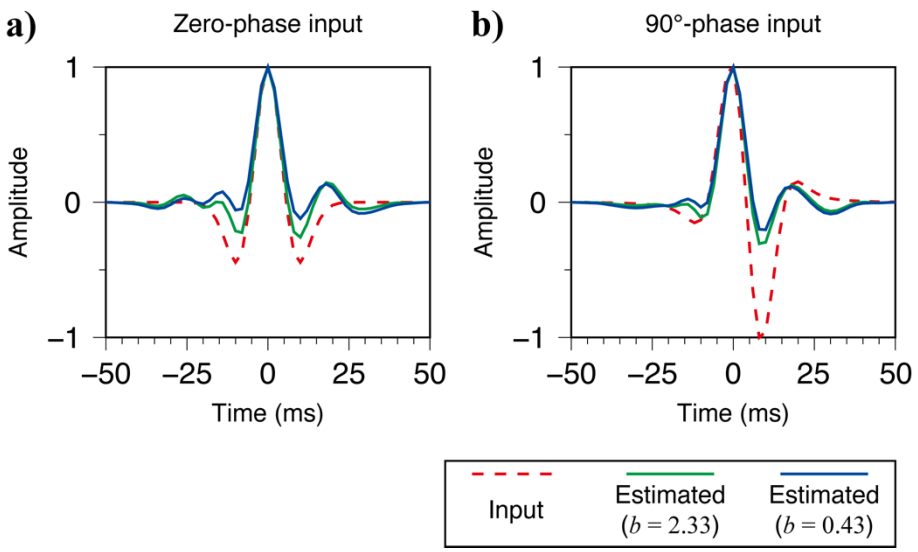

Figure 3.6. Input and inverted source waveforms obtained using different values of objective function coefficient b in equation (3.7) (legend): a) using Ricker wavelet as input source, and b) using 90°-rotated Ricker wavelet.

In the inversions of the synthetic data based on 90° Ricker wavelets (Figure 3.5b and Figure 3.6b), the shapes of the main lobes of the input wavelets are reproduced well but the phases are only slightly shifted in the correct directions. This difficulty of recovering the source-waveform phase from reflection seismic records is fundamental and impossible to resolve without knowledge or restrictive assumptions about the reflectivity $r(t)$ (e.g., Edgar and van der Baan, 2011; Kazemi and Sacchi, 2014). Nevertheless, such recovery should still be possible for certain forms of reflectivity series consisting of isolated sharp reflections, and I test whether this may be the case for the Weyburn well-log model (Figure 3.3a). For the synthetic seismogram created with the minimum-phase Ricker wavelet (Figure 3.3b), the waveform-estimation test is performed by using the "width-phase" optimization (section 3.2). With $b = 1$ in equation (3.7), the estimated source waveform is shown in Figure 3.7. As this figure shows, the near-minimum phase waveform is achieved.

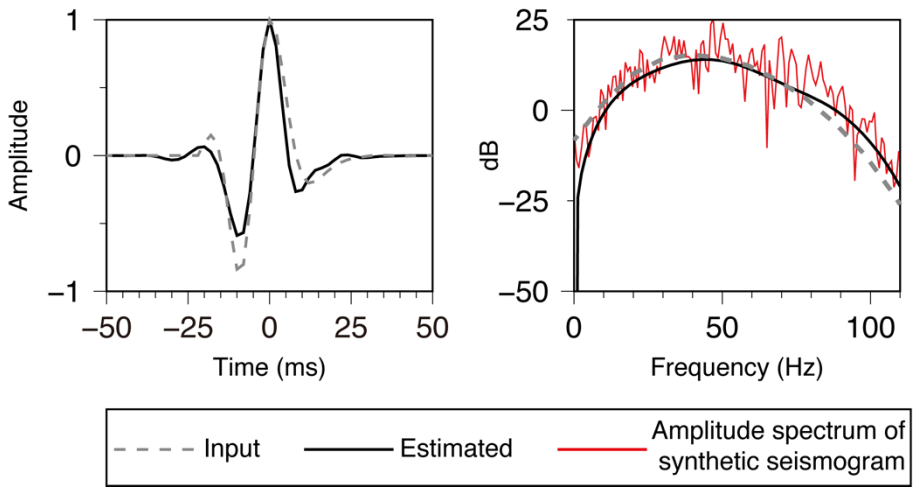

Figure 3.7. Waveforms and amplitude spectra for the input and estimated source waveforms (legend) by using "width-phase" optimization for the real-log model (Figure 3.3).

3.3.2 Synthetic stochastic-log model

To evaluate the dependence of estimated source waveforms on statistical properties of reflectivity time series $r(t)$ (equations (3.1) or (3.5)), I also perform several tests using synthetic seismograms built from stochastic 1-D velocity distributions. Holliger (1996) showed that synthetic well logs with realistic properties can be simulated by combining large-scale, deterministic velocity-time/depth functions with correlated velocity fluctuations characterized by the von Kármán autocovariance function. In frequency domain, the von Kármán autocovariance equals (Holliger, 1996)

$$P(f) = \frac{\sigma^2 \left(2\sqrt{\pi}\tau\right)^E \Gamma(\nu + E/2)}{\Gamma(\nu)\left(1 + f^2\tau^2\right)^{\nu + E/2}}, \tag{3.9}$$

where σ is the standard deviation of velocity fluctuations, τ is their correlation time lag, ν is the Hurst number describing the self-similarity property of the fluctuations, Γ denotes the gamma

function, and the Euclidean dimension E of the model equals one for a 1-D well log. By setting parameters σ, τ and ν, various velocity-fluctuation time series can be created by the following procedure (Holliger, 1996): 1) generate a uniformly-distributed random time series and transform it into the frequency domain, 2) scale it by the square root of equation (3.9), 3) take the inverse Fourier transform, and 4) add another uncorrelated sequence of random, white Gaussian noise.

Figure 3.8 shows three velocity and primary reflectivity ($r(t)$) pseudo-logs created by the above procedures with different parameters τ and ν and a constant background velocity of 4000 m/s. Note that larger correlation times τ generally lead to longer fluctuation periods in the velocity pseudo-logs, and larger Hurst numbers ν lead to weaker high-frequency fluctuations in the velocity and reflectivity ($r(t)$) pseudo-logs (Figure 3.8). As in the preceding subsection, zero-phase Ricker wavelet is used to create synthetic seismograms, in which the low-frequency component below 15 Hz is multiplied by a factor of 1.5.

For this stochastic-log model, several source-waveform estimations were performed using the "width-amplitude" optimization with $b = 1$ (equation (3.7)). For four combinations of $\tau = 5$ or 80 ms and $\nu = 0.1$ or 0.5, the estimated source waveforms are shown in Figure 3.9. These results show that although the reflectivity series are not visibly "sparse" in these models (Figure 3.8), the desired shape of the estimated wavelet (narrow main lobe and small side lobes) is still obtained consistently and similar to the real-log based tests in the preceding subsection. The estimated cut-off frequency f_0 and weight c (labels in Figure 3.9) are close to the expected values of 15 Hz and 1/1.5, showing that the method correctly responds to the considered coherent-noise effects in the records.

Next, I investigate the effect of parameter ν on the shape of the estimated wavelets in this test. By comparing the resulting waveforms in Figure 3.9, it can be seen that the main lobes of the estimated wavelets are somewhat wider than those of the input Ricker wavelets, with this widening increasing with ν. This widening occurs because correlated (von Kármán) velocity fluctuations reduce the bandwidth of the seismic signal, which eventually similarly affects the source-waveform estimation. It appears that similar bandwidth effects should also affect all other "statistical" waveform-estimation methods. However, statistical analysis of sonic-log data from boreholes suggest that small-scale fluctuations are typically characterized by low Hurst numbers $\nu \approx 0.1$–0.2 (Holliger, 1996), for which the widening is negligible (Figure 3.9a and 3.9b).

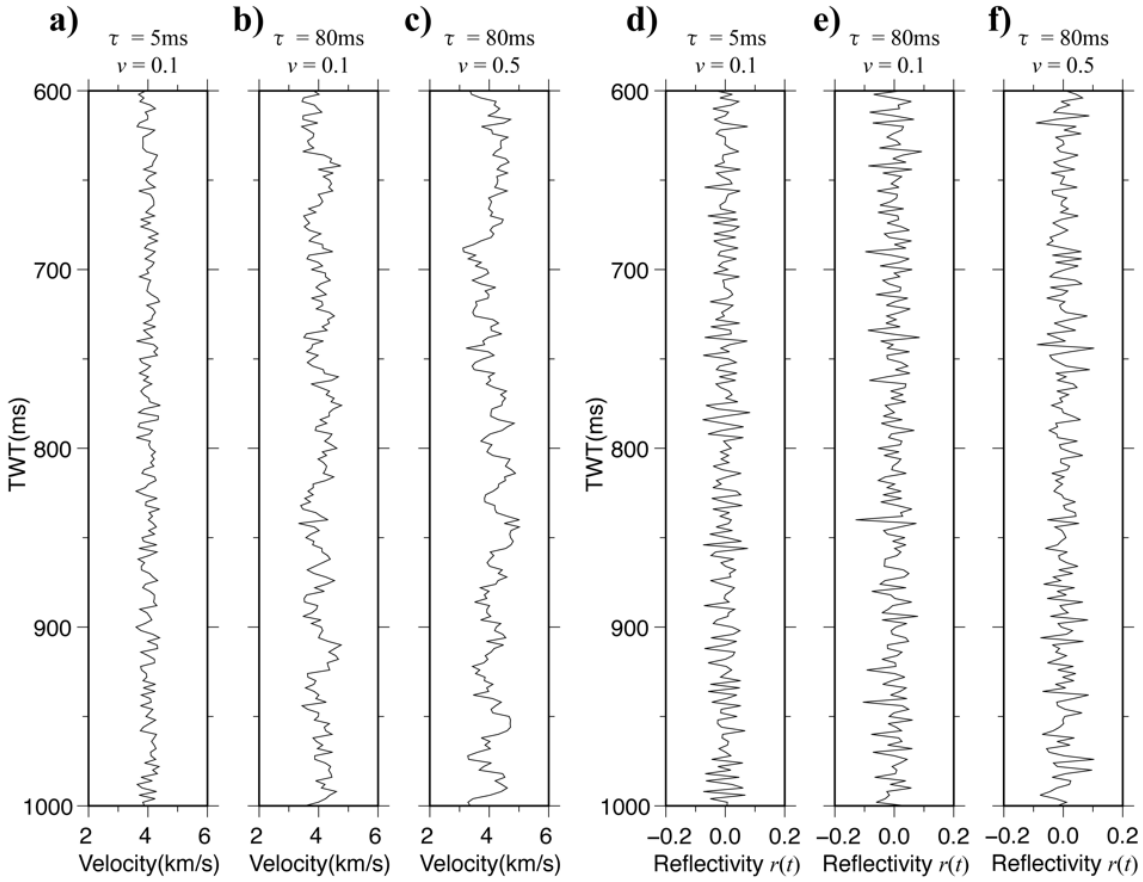

Figure 3.8. Synthetic velocity pseudo-logs (a)–c)) and the corresponding reflectivity series (d)–f)) modeled for different combinations of parameters τ and ν (labels).

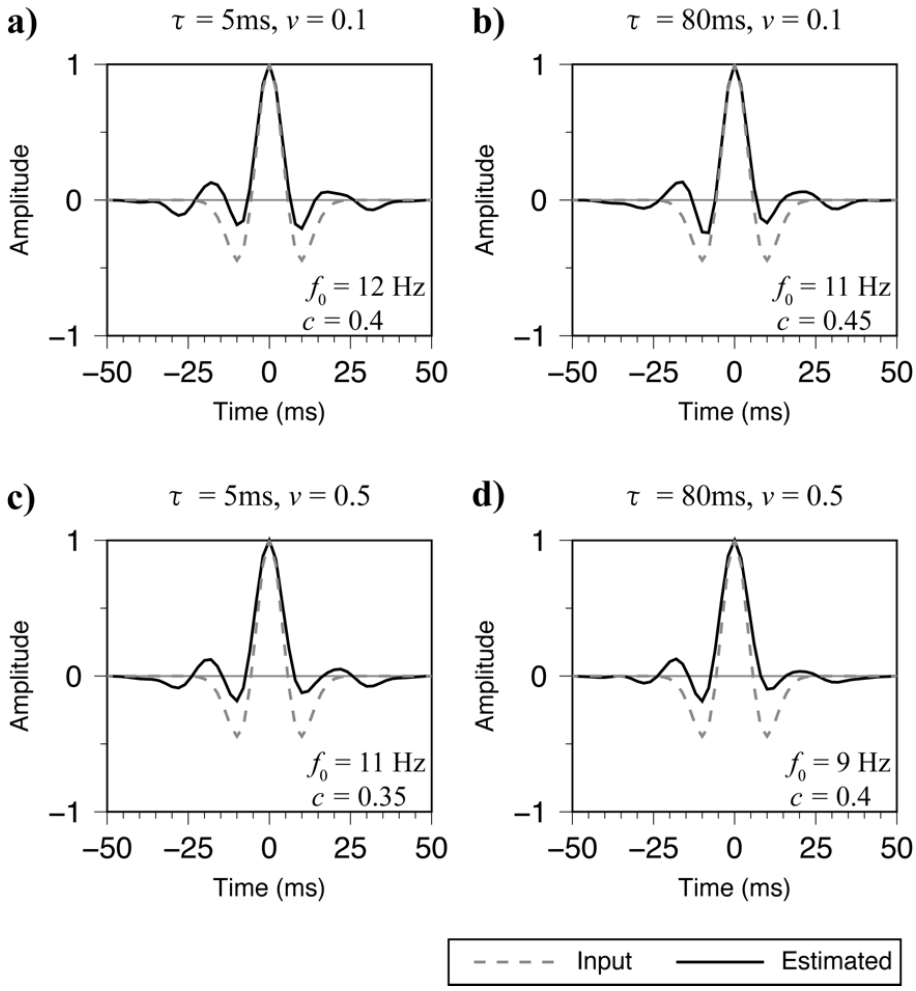

Figure 3.9. Extracted source waveforms from stochastic-log models with several pairs of von Kármán distributions τ and ν (labeled at the top of each plot). The labels below the graphs show the values of f_0 and c obtained during optimization.

To illustrate the effects of the added white Gaussian noise in velocity fluctuations or in equations (3.1) or (3.5), Figure 3.10 shows the source waveforms extracted from stochastic models with $\tau = 80$ ms and $\nu = 0.1$ and the signal-to-noise ratio (SNR) of 1 and 10. The SNR is defined in decibel as $\mathrm{SNR} = 10\log_{10}\left(P_{\mathrm{vel}} / P_{\mathrm{noise}}\right)$, where P_{vel} or P_{noise} is the average power of correlated velocity fluctuations or white Gaussian noise, respectively. The two estimated waveforms are close (Figure 3.10c), with a correlation coefficient of 0.99. These estimated

waveforms and the values of f_0 and c (labels in Figure 3.10) are also close to those in the preceding examples, showing that the estimation method is not significantly affected by such noise.

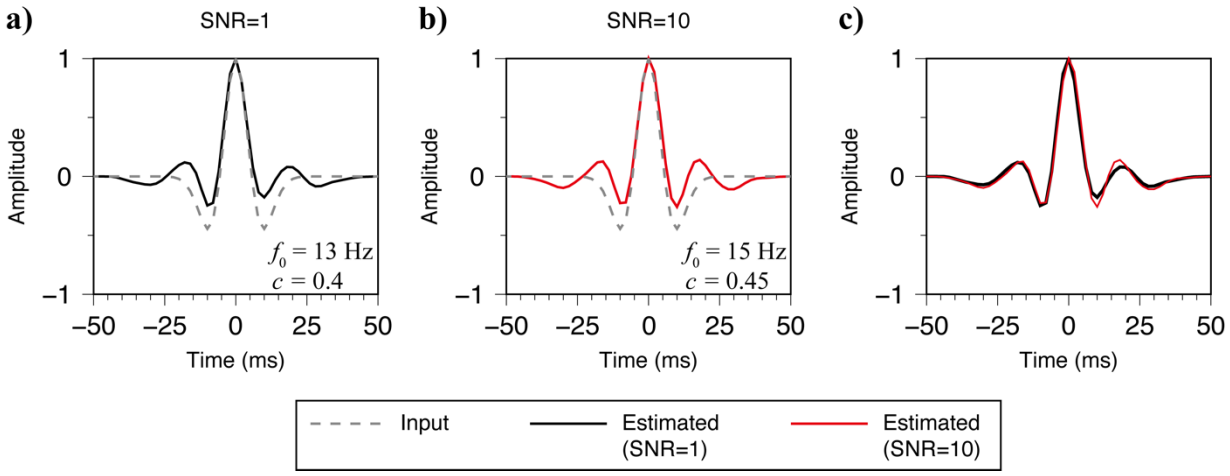

Figure 3.10. Source waveforms estimated from stochastic-log data with $\tau = 80$ ms, $\nu = 0.1$, and white Gaussian noise. The values of SNR, f_0 and c are given in the labels.

3.4 Tests and Examples using *Estimation B*

This section shows additional tests of the source-waveform estimation procedure for *Estimation B* in section 3.2, but this time with no time shifts between the low- and high-frequency signal components. These tests use the same parameters N, T_1, T, and T_s, and approaches for building synthetic seismograms from well logs, and the value of $b = 1$ in objective function (3.7) as in section 3.3. The resulting estimated wavelets $w_{\text{est}}(t)$ are also compared to the one used for data generation. Only real well-log example is examined in the following subsection.

3.4.1 Real well-log model

For the *Estimation B* procedure, synthetic seismograms in Figure 3.3 were modified as in section 3.3, by multiplying the amplitudes below frequency f_0 = 15 Hz by factor m = 1.5 in order to simulate a low-frequency coherent-noise effect described in section 3.2. Grid search parameters were also the same as in section 3.3, which was c ranging from 0 to 2 and trial f_0 values ranging from 5 Hz to 40 Hz.

For the cases of zero-phase and 90° input Ricker wavelets (Figure 3.3b), the procedure of wavelet estimation by the "width-amplitude" optimization is shown in Figure 3.11. In contrast to Figure 3.4 for forward model (3.5) with time shift (*Estimation A*), both cases in Figure 3.11 show that parameters f_0 and c corresponding to the minimum of the objective function (equation (3.7)) are far from the expected value of f_0, although reasonably close to the expected $c = 1/m \approx 0.67$ (dots in Figure 3.11). The wide areas in which the objective function is small (white and light gray in Figure 3.11) also indicate that the estimated waveform is not strongly sensitive to the trial parameters f_0 and c. In addition, the objective function attains undesirable minima at large frequencies f_0 and parameters c (Figure 3.11). These observations show that the global optimization procedure within a broad range of variables f_0 and c is unsuccessful in finding the correct values of f_0 and c. At the same time, because of the same low sensitivity of the objective function, even with inaccurately estimated parameters f_0 and c, the waveforms and amplitude spectra of the optimal extracted $w_{\text{est}}(t)$ for the two types of true source wavelets are reproduced well (Figure 3.12). Compared to the results of the *Estimation A* procedure (Figure 3.5), the estimated wavelets in Figure 3.12 are even closer to the input Ricker wavelets. In particular, for the case of a 90° input Ricker wavelet in Figure 3.12b, not only the shapes of the main lobes of

the input wavelets are reproduced well but the phases are partly recovered. In Figure 3.5b, the phase is only slightly shifted in the correct direction.

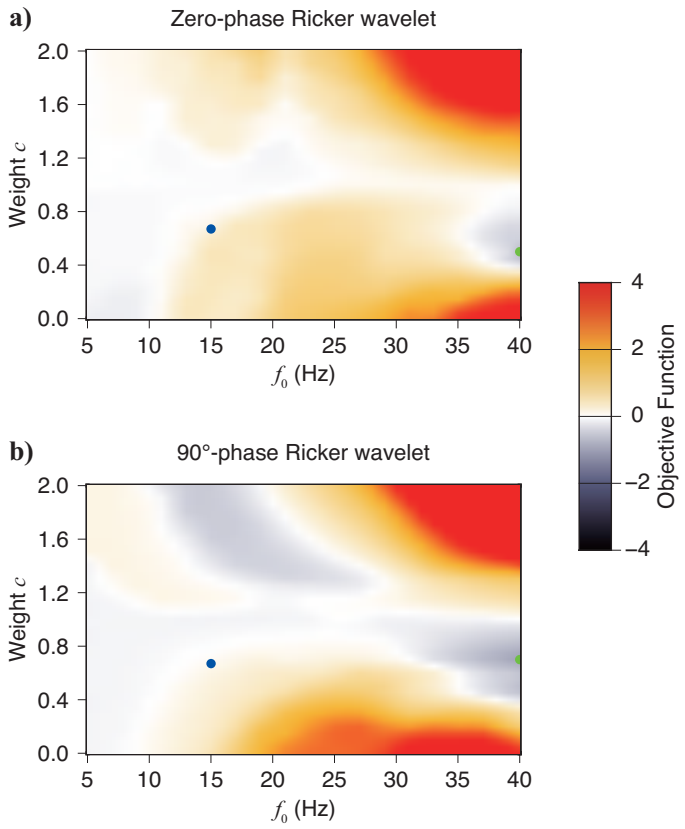

Figure 3.11. Values of the objective function during "width-amplitude" optimization (equation (3.7)) for: a) synthetic seismogram built using the zero-phase Ricker wavelet and b) using the 90°-phase Ricker wavelet (Figure 3.3b). Green dots indicate the optimum c and f_0 parameters, and blue dots are the expected values f_0 = 15 Hz and c = 0.67.

In another example, similar to Figure 3.7 in *Estimation A*, I perform waveform estimation by using the "width-phase" optimization (section 3.2) for the synthetic seismogram created with the minimum-phase Ricker wavelet (Figure 3.3b). With b = 1 in equation (3.7), the estimated source waveform is shown in Figure 3.13. As this figure shows, similar to the preceding example, the shape of the recovered wavelet tends to be near-minimum phase.

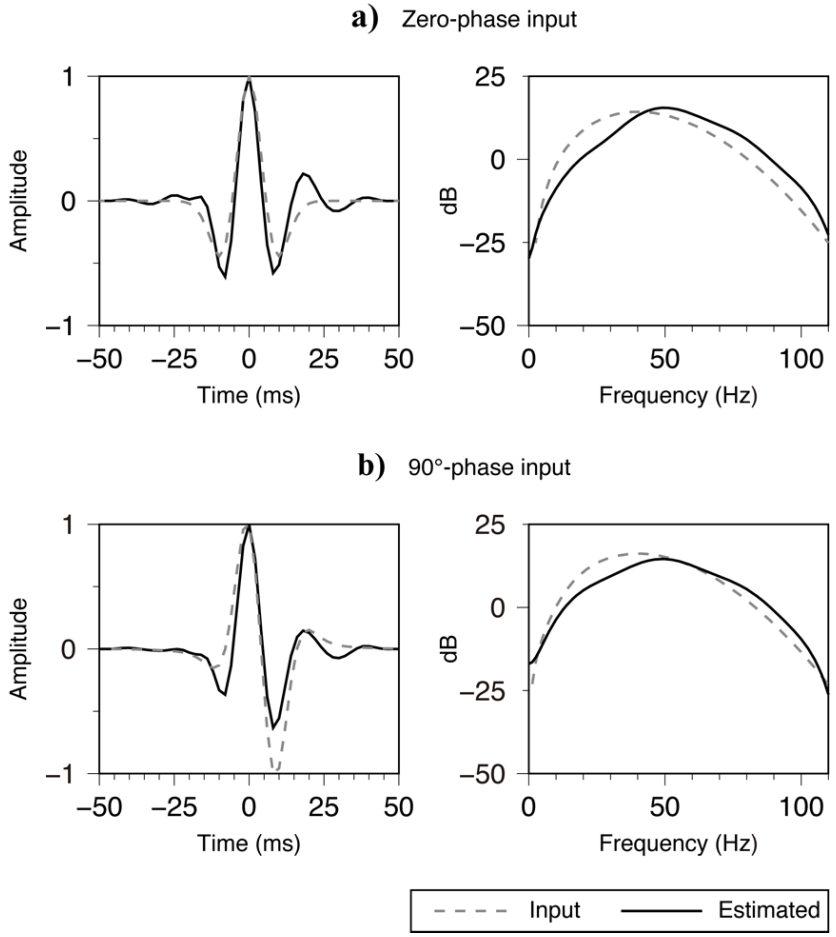

Figure 3.12. Waveforms and amplitude spectra for the input and estimated source waveforms (legend): a) for Ricker input wavelet and b) for 90° rotated input Ricker wavelet.

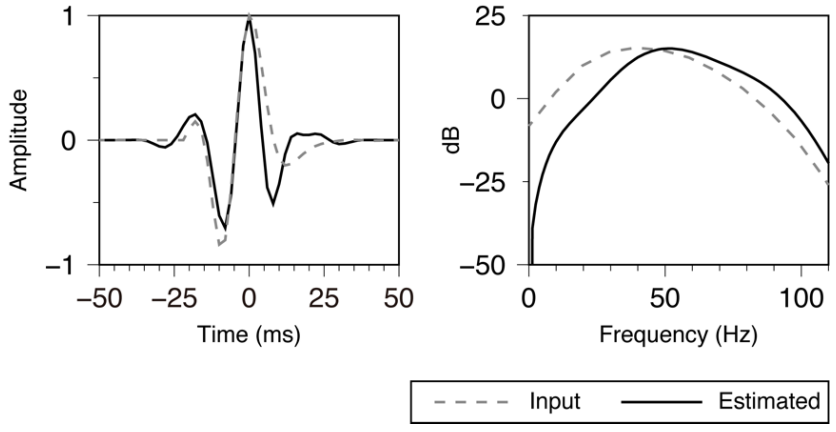

Figure 3.13. Waveforms and amplitude spectra for the input and estimated source waveforms (legend) by using "width-phase" optimization for the real-log model (Figure 3.3).

3.5 Application to Real Data

In this section, the source-waveform estimation method is applied to one trace from the stacked vertical-component seismic traces from the 3-D/3-C Weyburn reflection data (Figure 3.14a). As the previous test sections show that *Estimation A* is much better than *Estimation B* in correcting for the low-frequency inaccuracies of the input seismogram, in this section, I use the *Estimation A* procedure. Similar to the synthetic examples in sections 3.2 and 3.4, parameters of the algorithm are selected as T = 100 ms, T_1 = 300 ms, T_s = 23 ms (dominant period of the input seismic trace), and N = 3 (Figure 3.2). The objective function coefficient b is selected equal 1 (equation (3.7)). By using the "width-amplitude" optimization criteria, Figure 3.14b shows the source waveforms estimated from multiple common midpoint (CMP) locations. Note the consistent main lobes and low side-lobe amplitudes for each input trace. Variations of these estimated source waveforms are small, which suggests that this method is stable and practical in application to seismic data.

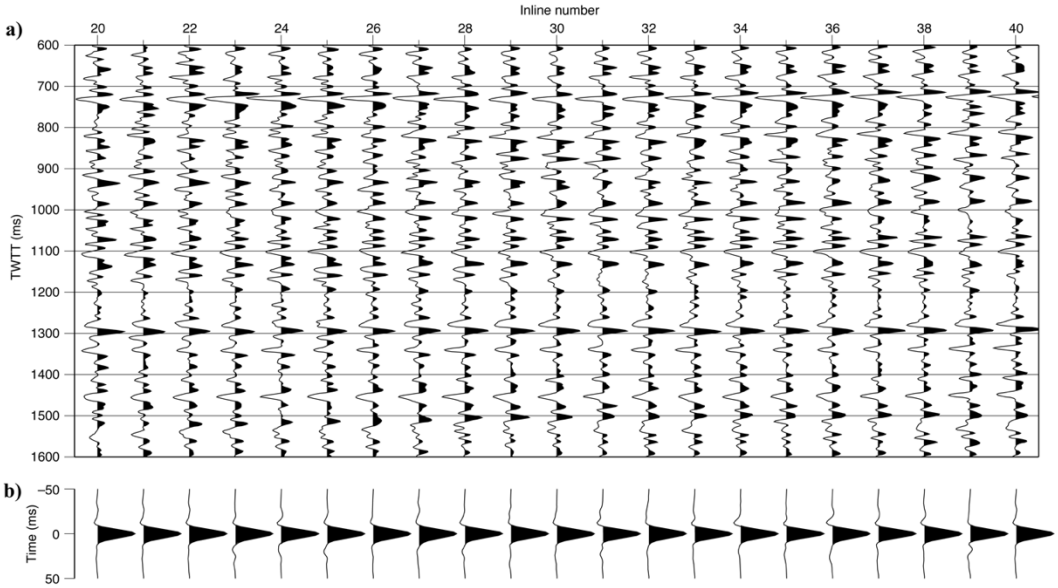

Figure 3.14. Source waveform estimations from a part of one stacked CMP line from the Weyburn 3-D dataset: a) input seismic traces, b) source waveforms estimated from each trace by using "width-amplitude" optimization.

For the correction for attenuation and dispersion by inverse-Q filtering, the values of the Q factor in equation (3.4) were taken equal from a simplified $Q_e(t)$ profile for the Weyburn CO_2 sequestration project area by Baharvand Ahmadi and Morozov (2013) and linearly interpolated between the following two-way reflection times: $Q(t \le 270 \text{ ms}) = 26$, $Q(t \le 610 \text{ ms}) = 66$, $Q(t \le 800 \text{ ms}) = 192$, and $Q(t \geqslant 1080 \text{ ms}) = 50$ (Table 1 in that paper). Figure 3.15 shows the source waveforms estimated with and without Q-compensation from one trace, as derived by using two types of optimization criteria. In both cases, the estimated waveforms show consistent shapes of the main lobe and small side-lobe amplitudes. With the "width-phase" optimization, the resulting waveforms are asymmetric and approximate a minimum-phase shape (Figure 3.15c). The values of parameters f_0 and c obtained by the optimization procedures (annotations in Figure 3.15b) are close to those expected from visual inspection of the power spectra of the records (not shown). For both types of optimization, Q-compensation has only a small effect on the results, which consists in the identification of higher-frequency side lobes (Figure 3.15). This shows that the waveform-estimation result should be dominated by smaller times, at which the signal is broader-band.

The wavelets shown in Figures 3.15a and 3.15b represent stationary source waveforms $\mathbf{w}_0$ corrected for the effects of Q. The corresponding nonstationary source waveforms at two-way reflection time t equal $\mathbf{w}(t) = \hat{A}(t)\,\mathbf{w}_0$, where $\hat{A}$ is the attenuation operator in equation (3.4). Taken at all reflection times t, the waveforms $\mathbf{w}(t)$ comprise the wavelet matrix $\mathbf{W}$ in equation (3.1b), which is shown for 14 values of t in Figure 3.16. In this representation of the matrix, the effects of waveform dispersion are shown by progressive delays of the main-lobe peaks relative to the diagonal of matrix $\mathbf{W}$ in Figure 3.16a and by the changing waveforms in Figure 3.16c. The near-exponential reduction of reflection amplitudes is clearly seen in Figure

3.16b and is related to wave attenuation. The reduction of the high-frequency content of the signal due to the effect of Q can also be noted by spectral analysis of the waveforms in Figure 3.16c. Thus, either in the form of the time-variant waveforms w (equation (3.1a)) or wavelet matrix **W** (equation (3.1b)), the resulting source model can be used to perform time-variant deconvolution, correction for attenuation effects, or for accurate evaluation of seismic to well-log ties.

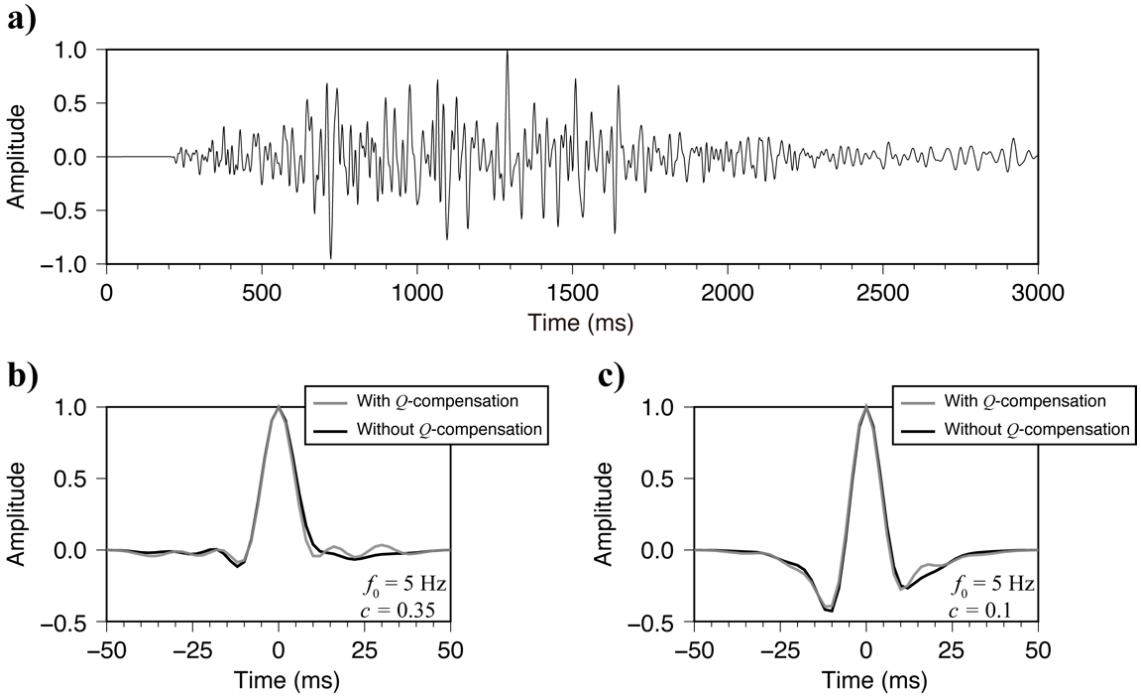

Figure 3.15. Source waveform estimation from one stacked trace from Weyburn seismic reflection dataset: a) input trace, b) source wavelets estimated by using "width-amplitude" optimization, and c) the same estimated by "width-phase" optimization. Labels in plots b) and c) show the values of f_0 and c obtained by the optimization procedures.

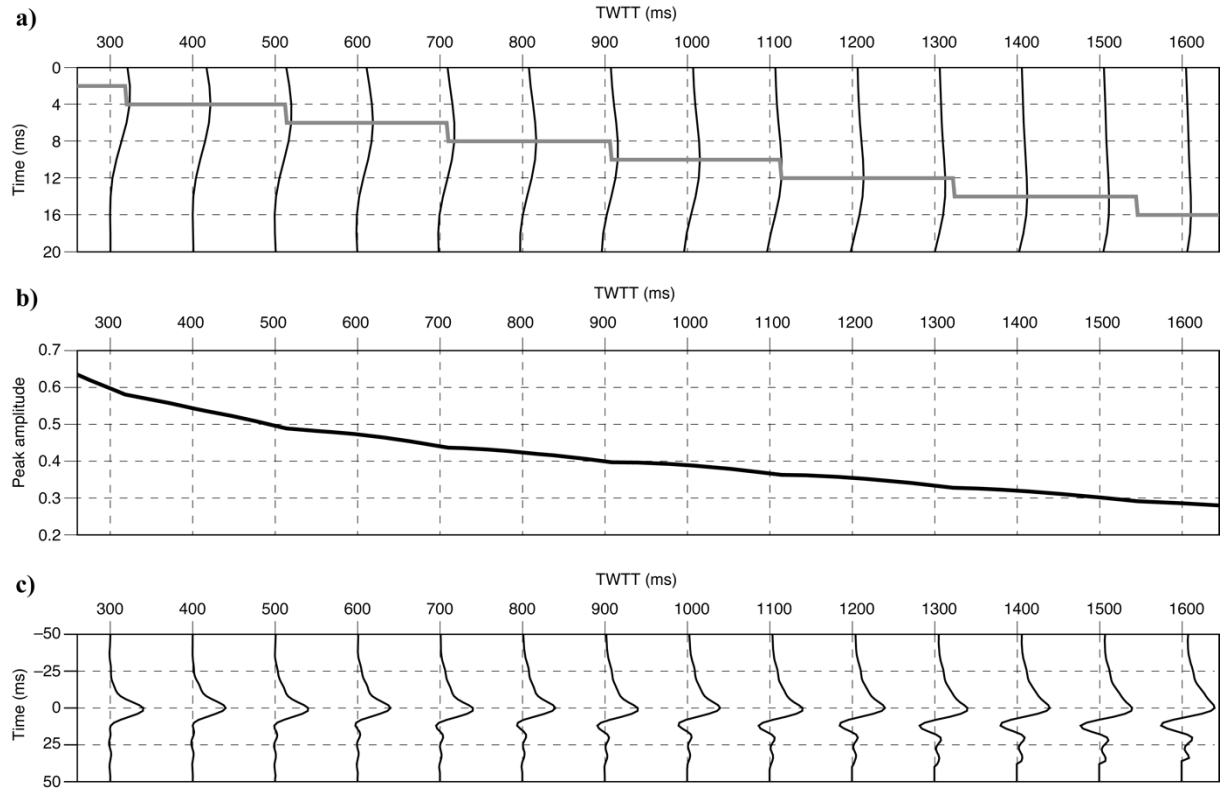

Figure 3.16. Columns of the nonstationary wavelet matrix **W** corresponding to the stationary source wavelet $\mathbf{w}_0$ derived by "width-amplitude" optimization (Figure 3.15b): a) travel times of the main-lobe peaks, relative to the diagonal of matrix **W** (thick gray line) and segments of the waveforms (thin lines); b) main-lobe peak amplitudes; and c) nonzero elements of matrix **W** aligned and normalized as defined in sections 3.3 and 3.4. In plot a), note that the discrete time jumps correspond to the rows of matrix **W** (horizontal grid lines) due to the 2-ms time sampling of the records.

3.6 *Q* Estimation from Reflection Records

By subdividing the entire seismic trace into a series of (possibly overlapping) time segments ($s_n(t)$) and performing estimations of source waveforms ($w_n(t)$) in each of them, the amplitude spectra ($A_n(f)$) of these wavelets can be calculated. By the well-known spectral-ratio

Q-estimation method, considering pairs of consecutive record segments number l and l+1, the quality factors Q between them can be estimated from

$$Q^{-1} = -\frac{1}{\pi\left(t_{l+1} - t_l\right)} \ln \frac{A_{l+1}\left(f\right)}{A_l\left(f\right)}, \tag{3.10}$$

where t_l denotes the time of the middle of the lth segment. This estimation is based on an assumption that in the absence of attenuation, the spectral shape of the wavelet inferred from different time levels within the reflection section should be the same. This assumption means that the reflectivity (and in particular, the strong and sparse reflectivity determining the result of this method) has the same spectral signatures at different t_l. This assumption appears to be reasonable even when the hypothesis of "white" reflectivity (Robinson, 1957) may be violated.

An initial test of this estimation using equation (3.10) is shown in Figure 3.17. In this Figure, A_1, A_2, A_3, A_4 are the amplitude spectra of the wavelets, measured within segments 0–500 ms, 500–700 ms, 700–1000 ms, and 1000–1300 ms of the seismic trace in Figure 3.15a respectively. The estimated Q values labeled in Figure 3.17 show depth variations of Q, which are close to those measured from VSP records in the same Weyburn area by Baharvand Ahmadi and Morozov (2013). However, as suggested in Chapter 7, more numerical tests and data examples still need to be considered to establish the reliability and utility of this application.

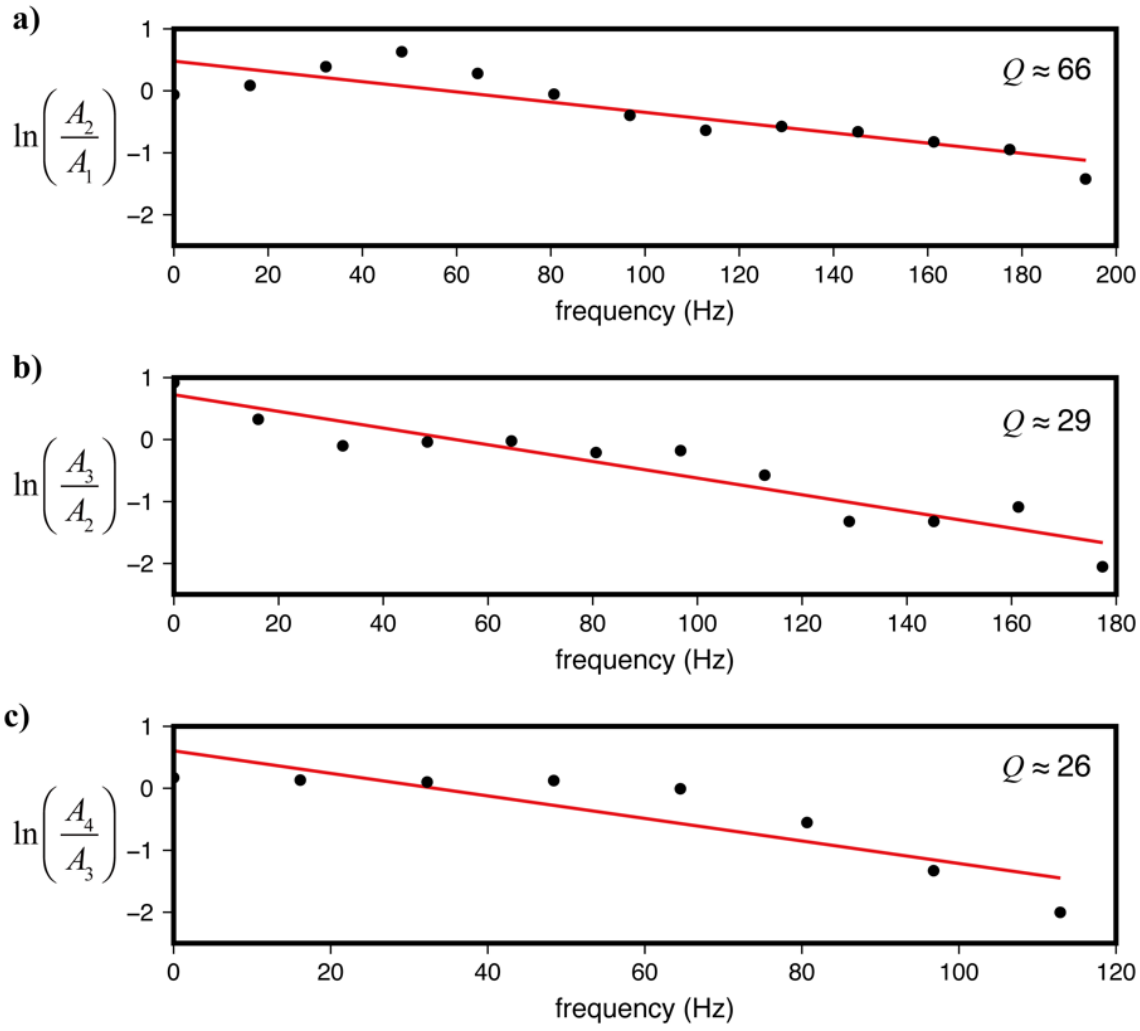

Figure 3.17. Q estimation by the spectral-ratio method using amplitude spectra of estimated source waveforms within: a) 250–600 ms, b) 600–850 ms, and c) 850–1150 ms. Black dots are the values of ($\ln\left[A_{l+1}(f)/A_l(f)\right]$), and red lines are their linear fits by constant Q labels).

3.7 Discussion

Applications to synthetic and real seismograms show that the proposed method allows estimating source waveforms by using either the proposed "width-amplitude" or "width-phase" waveform-shape optimization criteria. The method is simple, can work with low-SNR data, and

allows correcting for attenuation and band-limited, nonstationary coherent noise. With seismic data dominated by short-scale, correlated reflectivity fluctuations such as in the above stochastic reflectivity examples, the phase character of the source becomes lost but the main lobe of its waveform is recovered well. Arguably, in the presence of unknown short-scale correlated reflectivity, the phase of the source cannot be recovered in principle, and the proposed approach offers a good practical alternative of a simple source waveform with a narrow main lobe and low side lobes. At the same time, with data dominated by relatively sparse and strong reflections, similar to the observation in real reflection sections, the method may be able to partly recover the phase character of the source signature.

In order to validate the method and evaluate its limitations and the range of possible applications, it is necessary to understand its underlying physical hypotheses. Real subsurface is generally composed of complex multiscale layering, which can be both correlated and uncorrelated with the source signal. Reflection responses from such layering are further complicated by multiples, tuning caused by thin (below quarter wavelength) layers, variations of reflection amplitudes with incidence angles, mode conversions, and various types of coherent and incoherent noise. In individual seismic records, these effects may also be indistinguishable from those of attenuation. Consequently, the conventional assumption of constant ("white") amplitude spectra of elastic (or *Q*-compensated) reflectivity (e.g., Oldenburg et al., 1981) is not very accurate, but this assumption can hardly be improved in the general case. In this chapter, I employ a different, stronger-peak sparseness (SPS) hypothesis focusing on the statistical properties of the signal recorded in the vicinities of locally strongest reflections. Considering only strongest reflections within a time window should reduce the effects of multiples, mode conversions, and noise. Weaker reflections and short-period multiples occurring near strong

reflections can also be expected to have statistically uncorrelated time lags and amplitudes. If such stronger peaks in the recorded seismograms occur sufficiently sparsely (with separation exceeding the characteristic source period T_s), the stacking procedure described in section "Method" should reduce the various undesirable effects on the extracted source waveform.

Interestingly, realistic synthetics and real well-log and seismic data suggest that the above SPS hypothesis may be preferable to the simple *a priori* assumption of "white" reflectivity. In an attempt to quantify the sparseness of reflectivity, Figure 3.18 shows the dependencies of average times between reflections on their amplitudes. To obtain this plot, the time series of reflectivities from real and synthetic well logs (Figure 3.3a and Figure 3.8d), stacked seismic trace (Figure 3.14a) and uncorrelated random values (Gaussian distribution) were first tapered in segments of the same length (300 ms) and scaled to the same RMS amplitude (equal one) as in the waveform estimation procedure (section 3.2). Within these normalized time series, for any amplitude level A, we selected all signal peaks with absolute values exceeding A and measured their mean separation in time, denoted $\delta t(A)$. In the $(A,\delta t)$ plane, the SPS property of interest is indicated by a trend of δt values bending upward with increasing A (Figure 3.18).

Figure 3.18 suggests that all three types of signals considered in this paper possess the expected SPS property. The time separations between the peaks increase with amplitude. For von Kármán synthetic logs (section 3.3) and uncorrelated Gaussian random reflectivity series, the separation-time spectra are close and form a tight distribution (yellow and black dots in Figure 3.18), which is also close to the observations in the real reflectivity log (red in Figure 3.18). For amplitudes below about 1.5 of the window RMS values, the time separations of real reflectivity log are wider than in the synthetic logs and random reflectivity series, but above ~1.5 RMS

amplitudes, the synthetic and random reflectivity series become sparser. Peaks in reflection seismic records (green) are even sparser, principally because of the band-limited character of these records. By starting from the largest peaks (right sides of the distributions in Figure 3.18), the proposed waveform-extraction method utilizes the most favorable and well-separated portions of seismic records.

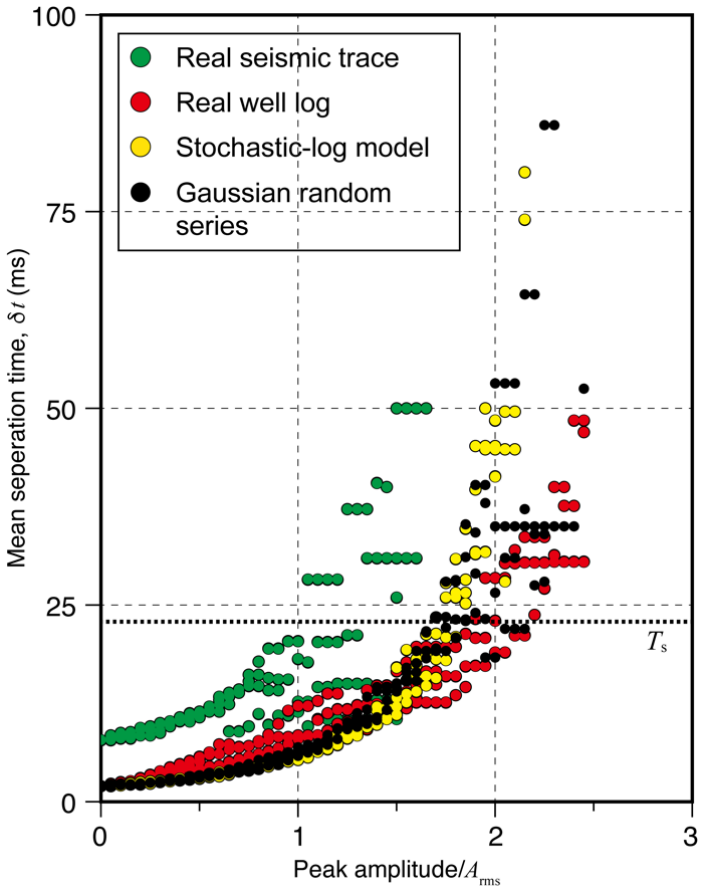

Figure 3.18. Dependencies of the average times between reflections on their minimum amplitudes for reflectivity series calculated in a real well log, synthetic stochastic log, real seismic trace, and in an uncorrelated Gaussian random time series (legend). Dotted line labeled T_s indicates the required minimum level of time separation.

The noted difficulty of inferring the phase of the source wavelet (sections 3.1 and 3.3) is well-known, fundamental, and also common to all waveform estimation methods. Generally, within the time scale of the seismic wavelet (T_s), almost any variation of the phase of the wavelet matrix **W** (equation (3.1b)) can be traded off with an appropriate variation of **r**. Similar to all statistical methods, the method of this paper resolves this trade-off empirically, assuming that the unknown short-scale variations near the strongest peaks in the impulse response **r** are mutually incoherent for different picks and suppressed by the weighted stacking (equation (3.3)). The incoherent noise (**n** in equation (3.1b)) is expected to be suppressed by statistical averaging, which should be achieved by a sufficient number of reflection peaks in equation 3. Further similarly to statistical methods, by summing multiple waveforms from different portions of the records (equation (3.3)), any anomalous shape of one reflection (caused, for example, by a surface wave in that time window) has only a limited effect on the result, and the resulting waveforms are stable (Figure 3.14b).

Along with its simplicity, the proposed method for source waveform estimation contains a significant potential for improvement by selecting filters $\hat{F}$ (equation (3.3)) appropriate for various types of data and observational environments. In this chapter, I only considered Q-compensation and correction for frequency-dependent amplification of the signal (filters $\hat{F}$ given by an inverse of equation (3.4) and a "pseudo-inverse" of equation (3.5)). For other nonstationary phenomena in the data, different filters can be designed. For example, if surface waves are incompletely attenuated by seismic processing, pre-stack data may contain low frequency, high amplitude arrivals masking body waves at ground-roll travel times. Air waves in land data similarly produce high-frequency and high-amplitude arrivals. Based on their expected travel times and frequencies, such arrivals can be suppressed or completely excluded by omitting

their time windows or selecting low amplitudes of filters $\hat{F}$ at the respective frequencies and travel times. In similar ways, selected time intervals or horizons can be emphasized or de-emphasized when applying the method to stacked data. Various instantaneous and multichannel attributes can also be used to construct filters $\hat{F}$ when working with prestack and stacked seismic data.

3.8 Conclusions

A simple and effective source-waveform estimation method is proposed based on iterative identification of the strongest and sparse reflections in seismic records. The approach is stable with respect to noise and parameter variations, and it allows accurately estimating the source waveforms without well-log control and sophisticated statistical hypotheses. The optimization approach allows correcting for coherent noise consisting in a possible spurious (de)amplification and phase shifts of the low-frequency components of the records. Such coherent-noise effects are reduced by optimizing the resulting source waveform in terms of its practically-important properties. Two types of criteria of such optimization are considered: one minimizing the main-lobe width and side-lobe amplitudes of the wavelet, and the second attempting to achieve a minimum-phase waveform. Similarly, other types of optimization criteria can be used. In addition, if the Q-factor is known for seismic waves in the study area, corrections for the effects of attenuation and velocity dispersion (non-stationarity of the source waveform) can be included in the approach, and the resulting source waveform is estimated at zero time, i.e. it is stationary. By using this source waveform, time-dependent waveforms can be predicted at any reflection time and used in many applications.

CHAPTER 4

WAVEFORM CALIBRATION AND TIME-LAPSE REFLECTIVITY DIFFERENCE

In this Chapter, I describe a waveform-calibration approach of time-lapse (TL) seismic datasets and an evaluation of TL reflectivity difference by using the attributes measured during this waveform calibration. They are illustrated on TL seismic data from the CO_2 sequestration project in Weyburn oilfield (Chapter 2). The presentation in this Chapter is based on the following paper:

> ***Wang, Y.**, and I. B. Morozov, 2018, Waveform calibration of time-lapse seismic data: GeoConvention 2018, CSPG/CSEG/CWLS, Abstract, https://www.geoconvention.com/archives/2018/204_GC2018_Waveform_Calibration_of_Time-Lapse_Seismic_Data.pdf.*

4.1 Introduction

Several types of engineering and geophysical methods are used to monitor and manage the processes of enhanced oil recovery in hydrocarbon reservoirs and geologic CO_2 sequestration. Well-logging measurements have the advantage of providing detailed and direct in situ information in depth, but wells sample only small areas laterally and are spatially sparse. In order

to provide a spatially-continuous assessment of physical properties within the reservoir or CO_2 storage site, TL seismic methods are often used (Lumley 2001; Arts et al., 2004).

For Weyburn Field, the reservoir zone is thin, and the injection of CO_2 into firm carbonates (vuggy limestone and marly dolostone; Chapter 2) creates only a few percent of expected P-wave velocity variations, which is near the seismic-noise level for detection (Lumley, 2010). Additionally, although the TL acquisition patterns were close to each other (Table 2.1) and pre-stack equalizations of the statics and waveforms were performed (Morozov and Gao, 2009), accurate consistency of stacked images still could not be achieved. Therefore, further calibration of stacked monitor records was required before calculating the reflectivity and acoustic impedance (AI) differences.

Several methods have been proposed to perform waveform calibration for TL seismic data. The principal challenge of this task is to achieve accurate consistency of the amplitudes and phases of the records from different vintages while retaining the TL variations within the target zones. Cross-equalization (Ross et al., 1996) has been widely applied by constructing matched filters to remove the acquisition-related differences between TL images. Generally, these matched filters include combinations of four operations: time shifting, amplitude scaling, spectral (bandwidth) equalization, and phase corrections. These operations are performed globally or locally within the images (e.g., Rickett and Lumley, 2001). Fomel and Jin (2009) presented a method to register TL images (i.e., to identify local associations of matching reflections in them) based on the local-similarity attribute. In addition to time corrections, Hale (2009) evaluated three-component displacement vectors for correction by local cross-correlation method and discussed its instability when the time shifts (vertical component) vary rapidly.

Druzhinin and MacBeth (2001) reported a sophisticated TL calibration workflow including 3-D resampling, global scaling and local spectral corrections combined with additional filters based on complex-trace attributes. Wang and Morozov (2018) gave an instantaneous-attribute based calibration method with very high matched-filter capability. However, local matched filters may become unstable in the presence of noise, and cross-equalization may overmatch seismic data so that significant TL signatures are unwittingly removed. To avoid overmatching TL datasets, Druzhinin and MacBeth (2001) applied the complex-trace based filters only outside of the target zone, and Wang and Morozov (2018) suggested a two-step procedure in which time-variant matched-filter parameters were measured outside of the target zone and continuously interpolated across the target zone. A similar approach is also taken in this paper. In addition, calibration approach in this chapter corrects for another undesirable effect that is not considered in the conventional cross-equalization. This effect consists in spurious reflection amplitude scaling caused by the time stretching itself (section 4.2 Method). In section 4.3, I show illustrations of this waveform-calibration method and its results for Weyburn reservoir. In section 4.4, I draw some general conclusions of this Chapter.

4.2 Method

4.2.1 Waveform calibration of time-lapse seismic data

Similarly to the well-known cross-equalization method (Ross et al., 1996; Rickett and Lumley, 2001), I perform TL waveform calibration of each stacked monitor record by three operations: time shifting, amplitude corrections and spectral shaping. These operations are similar to the elements of cross-equalization (Ross et al., 1996) but applied locally, by time-variant linear filtering using a group of overlapping Hanning windows in time. Each time

window contains a flat portion and two cosine-shaped ramps of equal durations, so that the sum of all windows equals one at any reflection time. For the baseline (u_{bas}) and monitor (u_{mon}) records tapered within one window, the calibrated monitor record (u_{cmon}) is obtained from u_{mon} by applying linear filters f_{tim}, f_{amp} and f_{spec} corresponding to time shifting, amplitude correction and spectral shaping, respectively:

$$u_{cmon} = u_{mon} * f_{tim} * f_{amp} * f_{spec}, \tag{4.4}$$

where "*" denotes the convolution operation. All of the three filters f_{tim}, f_{amp} and f_{spec} in equation (4.4) are applied in frequency domain. For filter f_{tim}, the transformation is represented by phase shift $-2\pi if\Delta t$, where f is the frequency and Δt is the desired time shift. Within each time window, the optimal value of parameter Δt (baseline minus monitor) is obtained by maximizing the cross-correlation of the monitor signal with the corresponding windowed record of the baseline survey.

After time shifting, the spectral-shaping filter f_{spec} is applied by

$$A_{cmon}(f) = A_{mon}(f)e^{-\pi(f-f_0)t^*}, \tag{4.5}$$

where $A_{mon}(f)$ and $A_{cmon}(f)$ are the amplitude spectra of $u_{mon}(f)$ and $u_{cmon}(f)$, respectively (equation (4.4)), and f_0 is the dominant frequency. With such scaling, the value of $A(f_0)$ is not changed by this filter. The spectral slope ("attenuation") parameter t^* is estimated by linear regression of the logarithm of the monitor and baseline signals with respect to frequency f and discarding the constant shift a:

$$\ln \frac{A_{\text{bas}}(f)}{A_{\text{mon}}(f)} = a - \pi t^* f, \tag{4.6}$$

where $A_{\text{bas}}(f)$ is the amplitude spectra of baseline seismic signal.

Finally, the amplitude-correction filter f_{amp} is performed by frequency-independent scaling:

$$u_{\text{cmon}}(t) = s u_{\text{mon}}(t). \tag{4.7}$$

The scaling factor s is obtained from dot products of the baseline and partially corrected monitor records within the window:

$$s = \frac{\int u_{\text{bas}}^2(t)\,dt}{\int u_{\text{bas}}(t)\left(f_{\text{spec}} * f_{\text{tim}} * u_{\text{mon}}\right)(t)\,dt}, \tag{4.8}$$

where $u_{\text{bas}}(t)$ is the baseline record.

For each of these filters, time-variant parameters are measured at the center of the corresponding window and linearly interpolated between adjacent windows. Additionally, these calibration parameters are evaluated just outside of the target reservoir interval and interpolated across it. This interpolation allows (presumably) preserving the TL variations within the target interval while correcting for the effects of different acquisition and seismic processing conditions that should be relatively slowly variable within the records. Due to the identical midpoint grids, flexibility of local cross-equalization, and relatively flat structure of the Weyburn reservoir, no spatial resampling of the monitor datasets is needed.

As noted in Chapter 3, the low- and high-frequency components of the stacked seismic records in Weyburn datasets may be somewhat differently affected by variations in source and receiver spectra, noise, and inaccuracies of normal moveout (NMO) corrections and stacking. Therefore, I separated the records into frequency components filtered below and above 20 Hz and performed calibration separately within these bands, by using 300-ms and 100-ms overlapping time windows respectively. The time-shifting and amplitude-correction filters f_{tim} and f_{amp} were applied to both low-and high-frequency components of the records, whereas f_{spec} was only applied to the high-frequency part of the data, which has a sufficient bandwidth for this correction. After calibration by using equation (4.4), the low- and high-frequency components were summed together to produce the resultant calibrated monitor traces.

4.2.2 Time-lapse reflectivity difference

By using the results of waveform calibration, the reflectivity difference between the calibrated monitor and baseline datasets is evaluated as follows. The idea of this calculation is to utilize the TL amplitude variations within the reservoir (caused by variations in fluid content and pressure) while disregarding local phase shifts, which should be negligible within a thin reservoir and should therefore be caused by noise. Due to the preceding calibration, ideally, there should be no phase or time shifts between the baseline and calibrated monitor reflectivities, which I denote r_{bas} or r_{cmon}, respectively. Therefore, these records can be related by a time-variant amplitude-scaling factor $\gamma_{\text{r}}(t)$:

$$r_{\text{cmon}} \approx \gamma_{\text{r}} r_{\text{bas}}, \tag{4.9}$$

which can be measured as $\gamma_r = \left|r^*_{cmon}\right| / \left|r^*_{bas}\right|$, where $\left|r^*\right|$ denotes the instantaneous amplitude (absolute value of the analytical signal) of record $r(t)$.

The measured TL reflectivity variation (factor γ_r) in equation (4.9) is obtained after waveform calibration, but the reflectivity is also affected by time stretching of the record occurring during waveform calibration. This change of reflectivity would take place even in the absence of true TL changes within the target zone, and therefore it must be corrected for. To correct for this time stretching, let us denote by t_0 the two-way reflection time in the baseline and t the time to the same reflector in the monitor record before calibration. These times are related as

$$t(t_0) \equiv t_0 - \Delta t = \int_0^{t_0} \frac{V_0}{V} dt_0 , \tag{4.10}$$

where Δt is the calibration time shift of the monitor record described in the preceding subsection, V_0 is the interval velocity at time t_0 in the baseline record, and V is the interval velocity at the corresponding time t in the monitor record. These velocities should be slightly different because of the TL variations of physical properties within the target reservoir. By differentiating equation (4.10) with respect to t_0, the time-stretch factor γ_v (due to velocity variation) is obtained as

$$\frac{1}{\gamma_v} = \frac{V_0}{V} = \frac{dt}{dt_0} = 1 - \frac{d(\Delta t)}{dt_0} . \tag{4.11}$$

After correcting for time stretching, the calibrated monitor reflectivity (equation (4.9)) would equal $r_{\text{cmon}}\, dt/dt_0 = r_{\text{cmon}}/\gamma_{\text{v}}$. Therefore, the TL reflectivity difference can be expressed in two ways: 1) directly as

$$r_{\text{diff}} = \frac{r_{\text{cmon}}}{\gamma_{\text{v}}} - r_{\text{bas}}\,, \tag{4.12a}$$

and 2) by using equation (4.9), as

$$r_{\text{diff}} \approx \left(\frac{\gamma_{\text{r}}}{\gamma_{\text{v}}} - 1 \right) r_{\text{bas}}\,. \tag{4.12b}$$

Both of these expressions for reflectivity difference will be used for evaluating the AI variations in Chapter 5.

4.3 Results

In this section, the above methods are applied to the vertical component of the 3-D 3-C TL seismic datasets from Weyburn Field (Chapter 2) by using tool "wfcalib" combined with several other components of IGeoS package (Morozov, 2008a). First, Figure 4.1 shows a detailed example of waveform calibration applied to one of the traces of monitor 2001 dataset. In this Figure, note that both the baseline and calibrated monitor records are shown by the same black color, and these records are close to each other. This comparison shows that the waveform calibration method is effective for matching the monitor traces to the baseline ones outside of the reservoir interval.

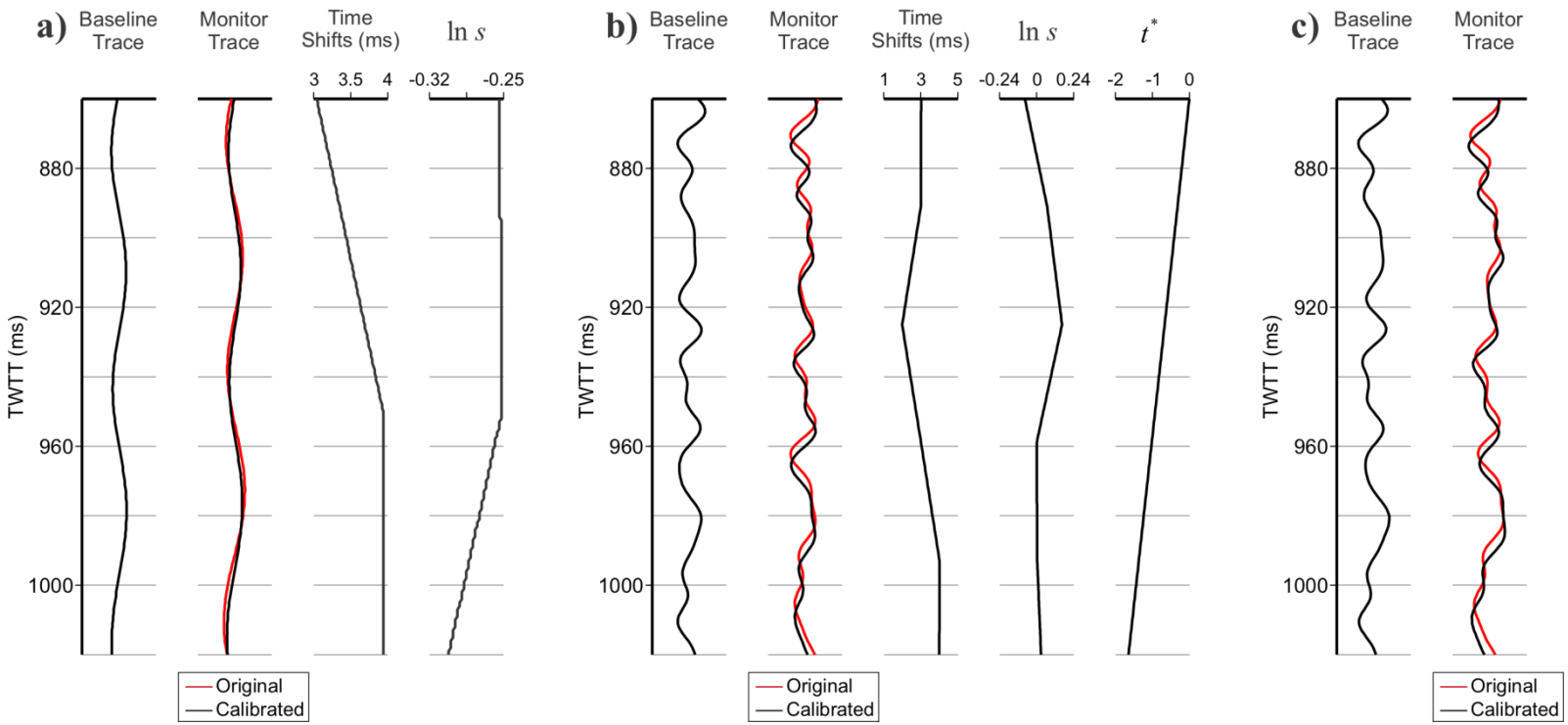

Figure 4.1 Application of time-variant waveform calibration to one stacked monitor record from 2001: a) low-frequency component of the record, b) high-frequency component of the record, c) resulting records. The original and calibrated monitor records are indicated in the legends. Note that the black lines (baseline and calibrated monitor) in each plot become close after calibration. In panels a) and b), the additional graphs show the calibration time shifts (Δt), natural logarithm of the amplitude scaling factor ($\ln s$ in equation (4.8)), and parameter t^* (equation (4.6)).

Figure 4.2 illustrates the TL reflectivity differences (r_{diff}) between the monitor and baseline datasets. In Figure 4.2b, r_{diff} is evaluated by direct subtraction of monitor 2001 and baseline after amplitude cross-equalization only (filter f_{amp} in equation (4.4)) and Figures 4.2c and 4.2d show the r_{diff} by equation (4.12b). Similar to the examples by Ross et al. (1996), a comparison of Figures 4.2b and 4.2c shows the importance of time shifting and spectral shaping. After the waveform calibration, the reflectivity differences are notable within the target zone and effectively reduced outside of it (Figures 4.2c and 4.2d).

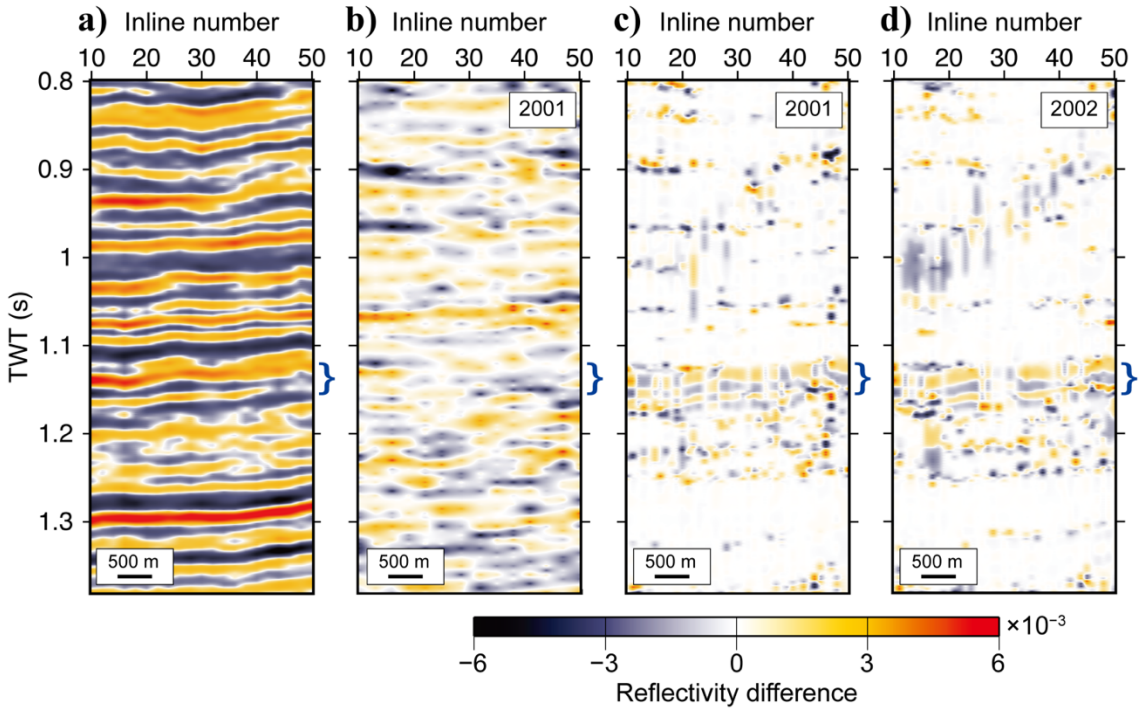

Figure 4.2. A segment of crossline 40 (Figure 1) illustrating TL calibration: a) Stacked reflection records from baseline 1999; b), c) and d) reflectivity differences for the monitors (labeled). The values of reflectivity differences in b), c) and d) are shown by color bar at the bottom. The reservoir zone is indicated by blue brackets.

The time shifts between reflections directly measured during the waveform calibration procedure represent one of the most significant indicators of TL changes within the reservoir.

Figure 4.3 shows the time shifts (baseline minus monitor) on Bakken horizon, which is a strong reflection located at about 150 ms below the bottom of reservoir (Figure 2.4). The observed negative time shifts of about 0.5 – 1.5 ms spatially correlate with the CO_2 injection patterns and should be due to the decrease in seismic velocities caused by increased CO_2 saturation and pore pressures. This correlation is particularly noticeable in the SE part of the study area. The negative TL time shifts for monitor 2002 are stronger than for monitor 2001, which also appears consistent with the progress of injection. Taking 25 m for the thickness of the subsurface interval affected by CO_2 and 4500 m/s for the interval velocity before CO_2 injection, I estimate that the injection of CO_2 causes a P-wave velocity reduction from about 4% to 12%.

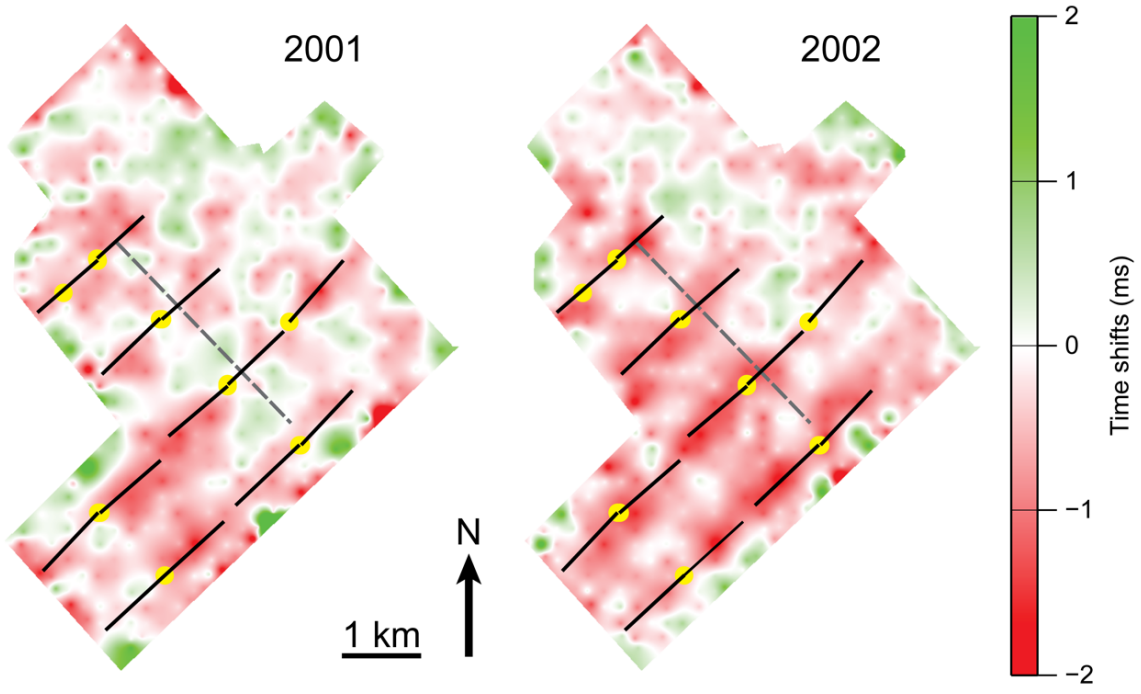

Figure 4.3. Time shifts between monitors (labeled) and baseline on Bakken horizon. Gray dashed lines show the crossline 40 for which the following cross-sections are shown. Black lines indicate the horizontal injection patterns and yellow dots are the locations of CO_2 injection.

By using the time-shift values in Figure 4.3 and reservoir-zone thickness calculated from the caprock and bottom horizons (Figure 2.4), equation (4.11) gives the factor γ_v, and equations (4.12) then allow calculating the 3-D volume of TL reflectivity difference. Figure 4.4 shows the reflectivity differences evaluated by equation (4.12b) for the reservoir zone and its surrounding area of crossline 40 (shown in Figure 2.3b and Figure 4.3). The reflectivity differences r_{diff} are generally small outside of the reservoir zone, where they are not expected to be associated with TL signatures of the CO_2 injection. By averaging r_{diff} within 4-ms windows centered on the interpreted Marly reflection picks (Figure 2.4), a horizon slice of the TL reflectivity differences is obtained (Figure 4.4). These variations clearly correlate with injection-well patterns and with the observed TL time shifts (Figure 4.3). Therefore, the r_{diff} related to CO_2 injection within the reservoir zone were effectively isolated from the global differences removed during waveform calibration. These reflectivity differences are also generally stronger in 2002 than in 2001, especially in the SE part of the study area. The stronger differences in 2002 could be related to additional volumes of CO_2 stored in the reservoir zone. On the other hand, the reflectivity differences are not as pronounced in the northern part of the area where vertical CO_2 injection wells (not shown) are used and most of the CO_2 injected in this part is located in the lower Vuggy zone (Figure 2.1; White, 2009, 2013). The lack of reflectivity differences in this northern part was also noted by White (2013), who also related them to relatively low reservoir porosities in this area. In the next Chapter 5 of this dissertation, the obtained TL reflectivity difference will be further used for the evaluation of TL AI.

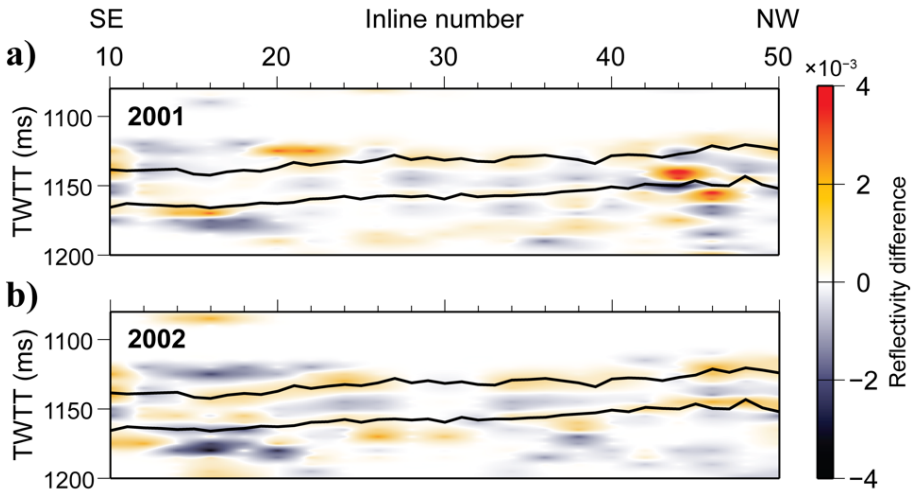

Figure 4.4. TL reflectivity differences between calibrated monitors and baseline along crossline 40: a) monitor 2001; b) monitor 2002. Black lines are the caprock and bottom horizons (peaks of positive reflections) of the reservoir zone.

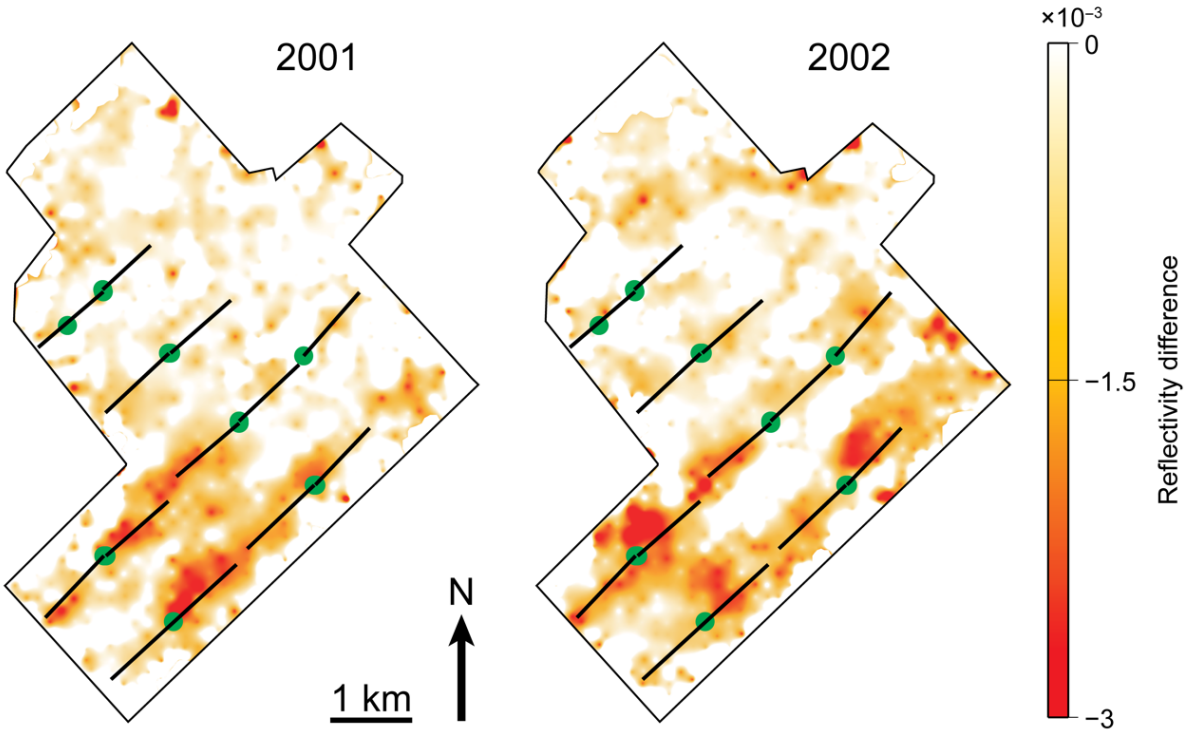

Figure 4.5. Negative-polarity reflectivity differences between calibrated monitors (labeled) and baseline on Marly. The lines and green dots are as in Figure 4.3.

4.4 Conclusions

Time-variant waveform calibration composed of time shifting, amplitude corrections and spectral shaping effectively eliminates the differences between the monitor and baseline traces outside of the reservoir interval of Weyburn oilfield. From the measured negative time shifts of about 0.5 – 1.5 ms, a P-wave velocity reduction up to 12% due to CO_2 injection in the Weyburn oilfield is estimated. Following the waveform calibration of monitor datasets, TL reflectivity difference is evaluated by using the measured time shifts and instantaneous amplitudes. The negative TL time shifts and reflectivity differences are spatially correlated with horizontal-well injection patterns. Both time shifts and TL reflectivity differences for monitor 2002 are stronger than for monitor 2001, which is consistent with the progress of CO_2 injection.

CHAPTER 5

TIME-LAPSE ACOUSTIC IMPEDANCE

The principal results of Chapter 4 consisted in measurements of time-lapse (TL) time shifts across the reservoir interval and the TL reflectivity difference for the Weyburn project. By using these measurements, the present Chapter 5 describes the procedure for obtaining the TL acoustic impedance (AI) variations. In contrast to the conventional approaches in which the TL AI is simply obtained by subtraction of the (calibrated) monitor and baseline AIs, I evaluate the TL AI directly from the TL reflectivity difference. The presentation in this Chapter is based on the following papers:

Wang, Y., *and I. B. Morozov, 2016, Constraining acoustic impedance inversion by seismic-processing velocities: 78th Conference and Exhibition, EAGE, Extended Abstracts, P612, doi: 10.3997/2214-4609.201601439.*

Wang, Y.*, and I. B. Morozov, submitted II, Time-lapse acoustic impedance variations during CO_2 injection in Weyburn oilfield, Canada, submitted to Geophysics, accepted.*

 The texts and figures of these papers were modified and reformatted for inclusion in this dissertation, and also expanded by additional material.

Similar to other chapters, section 5.1 starts with an introduction to the subject of TL AI inversion, at the end of which the pathways to other sections are further described.

5.1 Introduction

The P-wave AI (Lindseth, 1979) is one of the most commonly used geomechanical attributes derived from seismic reflection records. However, three principal difficulties of this attribute need to be addressed in order to make it sufficiently stable and accurate for detecting small in-situ AI differences occurring between TL datasets. The first difficulty is related to the need of accurate calibration of TL records, i.e. correcting them for time shifts, effects of velocity and statics models, and amplitude and spectral differences between TL seismic datasets. Ways for addressing these issues in the present study were described in Chapter 4. The second difficulty of obtaining an accurate TL AI is related to the inherent lack of low-frequency data in reflection seismic records and consequently in the inverted AI models (Lindseth, 1979). This uncertainty is amplified by the fundamentally arbitrary scaling factor inherent in the relation of AI to reflectivity. Therefore, the procedure for evaluating TL AI difference needs to be insensitive to such scaling and low-frequency uncertainties. Third, for accurate quantitative interpretation of the resulting AI, its amplitudes and spectral content need to be further calibrated in order to match the available well logs (Morozov and Ma, 2009). The last two of these problems are addressed in the present Chapter.

The AI is a mechanical material property used to characterize reflection and transmission of seismic waves across boundaries or gradational transitions between different media (Aki and Richards, 2002). For P-waves at normal incidence, the AI (denoted Z below) equals the product of rock density (ρ) and wave velocity (V):

$$Z = \rho V \ . \tag{5.1}$$

For a stack of constant-impedance layers, denoting R_i the normal-incidence P-wave reflectivity of the boundary between layers i and i+1, the AI within k^{th} layer can be obtained from the seismic reflection series $\{R_i\}$ occurring at times $\{t_i\}$ (Lindseth, 1979; Russell, 1988):

$$Z_k = Z_{0k} \prod_{i=0}^{k-1} \frac{1+R_i}{1-R_i} \approx Z_{0k} \exp\left(2 \sum_{i=0}^{k-1} R_i \right), \tag{5.2}$$

where the approximate equation is valid when $\sum_{i=0}^{k-1} R_i << 1$. In this relation, Z_{0k} denotes a slowly-varying function of layer number k containing an arbitrary scaling factor and additional low-frequency "drift" caused by the discretization, noise, and various types of errors in $\{R_i\}$ accumulated by the product or summation of multiple factors. The times $\{t_i\}$ are usually taken equal the seismic-record sampling times, and the AI inverted by equation (5.2) is a discontinuous function $Z(t)$ which is constant within each interval $[t_{i-1}, t_i]$. However, this discontinuous $Z(t)$ is difficult to use for calculating the TL AI because the series $\{t_i\}$, $\{R_i\}$, and $\{Z_k\}$ are affected by time stretching of the records, which is an important part of the monitor-to baseline waveform calibration procedure described in subsection 4.2.2 of Chapter 4. When inverting the AI from seismic records, the reflectivity needs to be treated as a continuous function $r(t)$, and the resulting AI is also a continuous function of two-way reflection time, given by

$$Z(t) = Z_0(t) \exp\left[2 \int_0^t r(\tau)\, d\tau \right], \tag{5.3}$$

where $Z_0(t)$ is a continuous scaling and low-frequency drift function, and $\left| \int_0^t r\, d\tau \right| << 1$ is assumed at any t. The discrete-layer impedances (equation (5.2)) are obtained from equation

(5.3) for a special form of (discrete, spiky) reflectivity variation $r(t)=\sum_{i=0}^{k-1} R_i \delta(t-t_i)$, where $\delta(t)$ denotes the Dirac delta function.

The uncertainties in AI scaling described by factor $Z_0(t)$ (equation (5.3)) can only be removed by using additional data such as well logs, estimated subsurface velocities, or geological models. These corrections are performed by scaling the low- or high-frequency recursive-AI solutions (Lindseth, 1979), by using joint-inversion and statistical methods (Cooke and Schneider, 1983; Russell and Hampson, 1991; Latimer et al, 2000), or by well-log based calibration of AI spectra, such as in colored AI inversion (Lancaster and Whitcombe, 2000; Morozov and Ma, 2009). In this study, I remove the uncertainties of AI (equation (5.3)) by time-variant well-log calibration (Morozov and Ma, 2009), which also incorporate the interval velocities derived from seismic data processing. This approach is simple and entirely driven by the data with physically interpretable step-by-step results. Compared to joint AI-inversion methods (e.g., Russell and Hampson, 1991), the inversion does not use sophisticated inverse or statistical algorithms, and requires no subjective selections of their parameters.

In the following section 5.2, I describe several steps of the procedure for deriving the TL AI. Final TL AI-difference images are shown in section 5.3. The resulting images improve the TL interpretation (Stammeijer and Hatchell, 2014) and help characterizing the detail of seismic-impedance changes occurring within the CO_2 injection zones of Weyburn Field. Based on these results in section 5.3, further analysis for the CO_2 distribution of this Weyburn Field is discussed, and in section 5.4, I give conclusions of this Chapter.

5.2 Methods

This section describes several elements of the method for evaluating the TL AI. Subsections 5.2.1 and 5.2.2 describe the derivation of the background velocity model and velocity/density relations required for evaluating the low- (sub-seismic) frequency and well-log AI. Such velocity volume gives a representation of the spatial variations of AI below the seismic frequency band, and the seismic-frequency part of AI is constrained by well-log data (subsection 5.2.3). The procedure for deriving the TL AI difference in Weyburn datasets is described in subsection 5.2.4, in which the AI difference is calculated from the reflectivity difference (Chapter 4; equations (4.12)) and spatially-variable baseline AI. Compared to subtraction of independently calculated baseline and monitor AI volumes, this AI-difference calculation is much more stable with respect to TL noise in the data.

5.2.1 Velocity model

In the subsequent AI inversion (subsection 5.2.3) by using the method by Morozov and Ma (2009), AI "pseudo-logs" will be needed at multiple locations within the study area. These pseudo-logs will be located at each location of the stacking-velocity picks performed during seismic data processing (Gao, 2011) and interpolated into the volume of the survey. To derive the low-frequency AI columns, vertically-continuous interval-velocity models are required. I derive such interval-velocity model from the stacking-velocity picks (Gao, 2011). These moderately spatially variable velocity columns reflect the heterogeneity of the study area (Figure 5.1). The derivation of the interval velocity for a CMP located near the well (Figure 2.3a) is illustrated as follows.

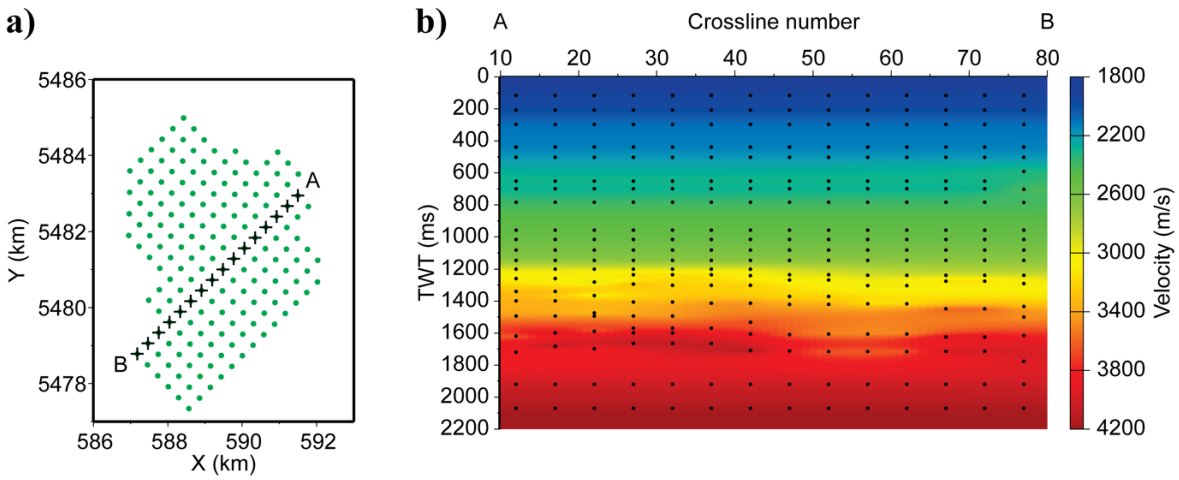

Figure 5.1. Stacking-velocity model obtained during reflection data processing: a) CMPs (green dots) used for picking stacking velocities; b) cross-section along line AB. Black crosses in a) indicate the inline position of the cross-section in b). Black dots in b) indicate the times of stacking-velocity picks.

For a horizontally-layered velocity structure, the stacking velocity equals the root-mean-square (RMS) velocity V_{rms}, which is related to the interval velocities V_{int} by

$$V_{\text{rms}}^2(t) = \frac{1}{t}\int_0^t V_{\text{int}}^2(\tau)\,\mathrm{d}\tau\,. \tag{5.4}$$

To ensure that the $V_{\text{int}}(t)$ is a continuous function, I use the Rayleigh-Ritz method (Korn and Korn, 2000) and parameterize $V_{\text{int}}^2(t)$ as a combination of N_{m} continuous basis functions $\varphi_i(t)$:

$$V_{\text{int}}^2(t) = \sum_{i=1}^{N_{\text{m}}} \varphi_i(t)\, m_i\,, \tag{5.5}$$

where m_i are some unknown parameters, with $i = 1 \ldots N_{\text{m}}$. The piecewise-linear basis functions $\varphi_i(t)$ (red in Figure 5.2) are defined by

$$\varphi_i(t)=\begin{cases} 0 & \text{for } t \le t_{i\text{-}1}, \\ \dfrac{t-t_{i\text{-}1}}{t_i-t_{i\text{-}1}} & \text{for } t_{i\text{-}1} < t \le t_i, \\ \dfrac{t-t_{i+1}}{t_i-t_{i+1}} & \text{for } t_i < t < t_{i+1}, \\ 0 & \text{for } t_{i+1} \le t, \end{cases} \tag{5.6}$$

where t_i are some control time points, which I select equal the times at which the stacking velocities $V_{\text{stack}}(t_j)$ are picked during reflection data processing. From equations (5.4) and (5.5), the squared RMS velocity is also a linear combination of parameters m_i:

$$V_{\text{rms}}^2(t)=\sum_{i=1}^{N_{\text{m}}}\psi_i(t)m_i\,, \tag{5.7}$$

where functions $\psi_i(t)=\frac{1}{t}\int_0^t\varphi_i(t)\,d\tau$ (blue in Figure 5.2).

At times t_j, equation (5.7) must satisfy $V_{\text{stack}}(t_j)=V_{\text{rms}}(t_j)$, which can be written in matrix form as:

$$\mathbf{d}=\mathbf{L}\mathbf{m}, \tag{5.8}$$

where vector **d** consists of squared stacking velocities: $d_j=V_{\text{stack}}^2(t_j)$, and the elements of matrix **L** equal $L_{ij}=\psi_i(t_j)$. By inverting equation (5.7) for **m** by using the least-squares method, the squared interval and RMS velocities at any time t are predicted by equations (5.5) and (5.7), respectively.

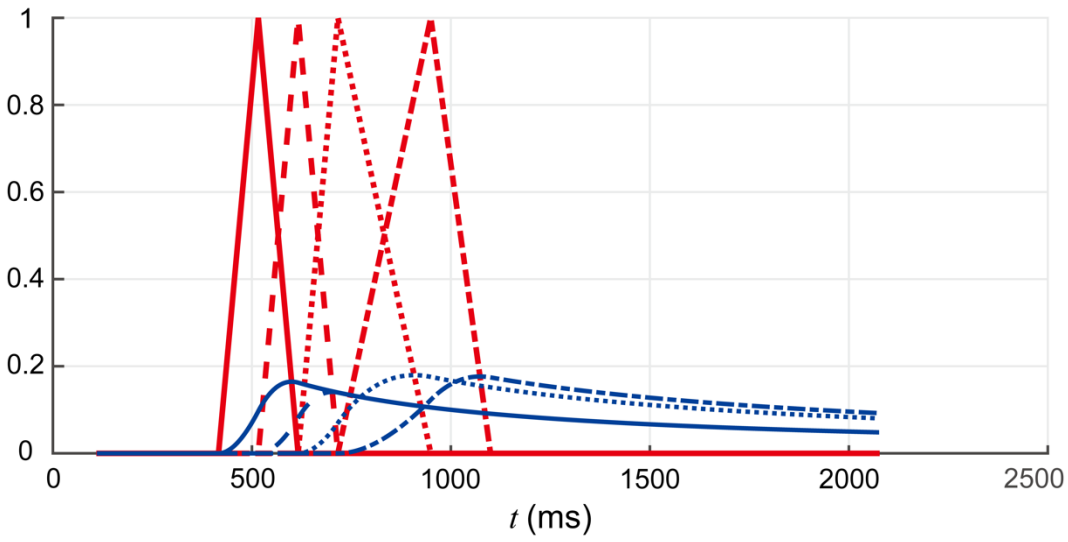

Figure 5.2. Basis functions $\varphi_i(t)$ (red) and $\psi_i(t)$ (blue) in equations (5.5) and (5.7) for four consecutive values of i.

The above inversion procedure consists in constructing piecewise-linear interval-velocity depth functions accurately satisfying the observed stacking-velocity values. Because such interval-velocity columns are non-unique, I explore their variability by performing 100 perturbations of the control points (times at which the columns are constrained; t_i in equation (5.6)) by uniformly distributed random shifts from –50 to 50 ms. These perturbations produce interval- and RMS-velocity columns (Figure 5.3). To reduce the variations of interval velocities within time intervals poorly covered with stacking-velocity picks (black lines in Figure 5.3), the final estimated $V_{\text{int}}(t)$ curve at each time t was obtained by taking the median values of all 100 interval-velocity values (yellow curve in Figure 5.3). The obtained solution for the interval is consistent with the average trend of the P-wave acoustic-log velocity measured in the well (blue line in Figure 5.3).

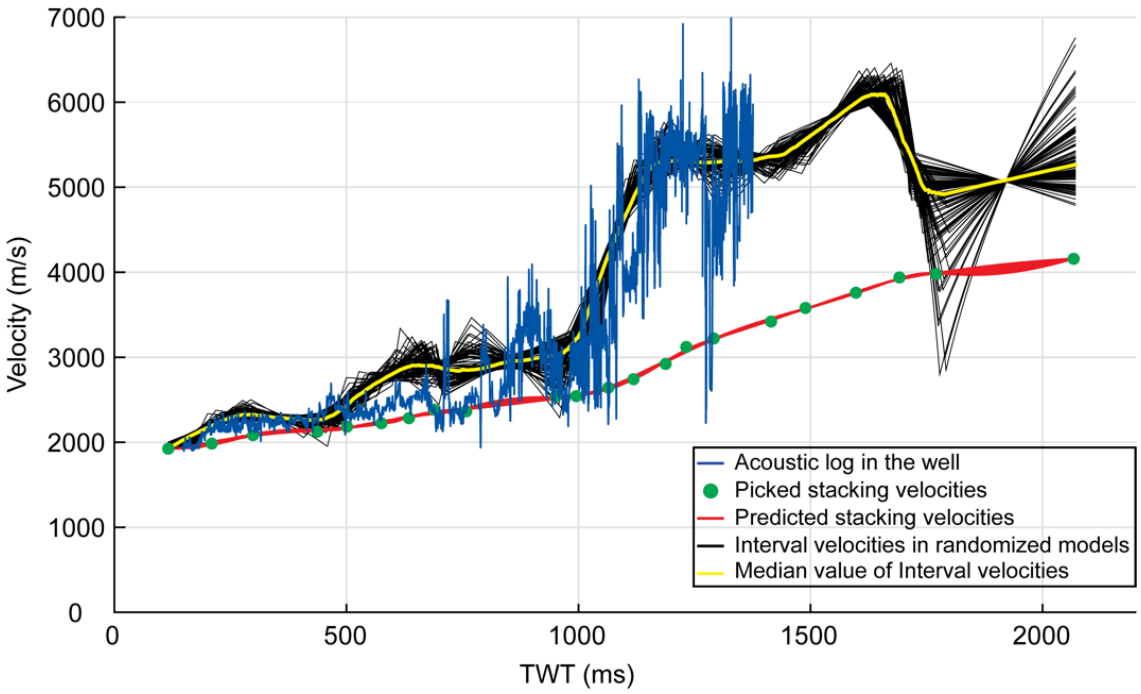

Figure 5.3. Stacking, interval, and well-log velocities for a CMP near well 102042300614 (legend).

5.2.2 Density/velocity relations

In addition to the interval-velocity columns at each pseudo-log location, density models are also required for evaluating the low-frequency AIs contributing to the pseudo-logs. At each pseudo-log location, this density model is derived from velocity by using the Gardner equation (Gardner et al., 1974):

$$\rho = \alpha V^{\beta}, \tag{5.9}$$

where V is the P-wave interval velocity and ρ is the density. This fairly general empirical equation is an effective approximation for density-velocity relations for a number of rock types like shales, sandstones and carbonates and is generally appropriate for clastic reservoirs. It is

accordingly expected to be suitable for the reservoir zone of this study area which is composed of limestone and dolostone. With this estimate for density, the low-frequency AI is obtained from V as

$$Z_{\text{vel}} = \alpha V^{1+\beta}. \tag{5.10}$$

Study-area specific parameters α and β in equations (5.9) and (5.10) can be estimated by interpretative linear fitting of $\ln\rho$ as a function of $\ln V$. Cross-plotting of the P-wave velocity and density readings from the well logs suggests several layers with somewhat different parameters α and β within and outside the reservoir (Figure 5.4). Above the reservoir, two layers with $\rho(V)$ trends of $\alpha_1 \approx 0.15$ and $\beta_1 \approx 0.34$, and $\alpha_2 \approx 0.0315$ and $\beta_2 \approx 0.522$ can be identified (grey and black lines in Figure 5.4a). The R^2 statistic (coefficient of determination, the proportion of variance of ρ predicted by the $\rho(V)$ trend) for these $\rho(V)$ relations are shown in the labels in Figure 5.4a. All of the data in Figure 5.4a can also be approximated by a single $\rho(V)$ trend (yellow line) of $\alpha \approx 0.052$ and $\beta \approx 0.465$, with $R^2 \approx 0.79$. The selection of one or two $\rho(V)$ dependencies above the reservoir has only a very small effect on the subsequent AI inversions (sections 5.2.3 and 5.2.4) as the relative RMS difference between the AIs obtained by using one or two $\rho(V)$ functions over the time interval of density log (Figure 2.6) is around 0.01. Such effect will also be similarly week on the calculation of differential AI.

In Figure 5.4b, I identify four velocity-density relations: Marly dolostone (purple), Vuggy limestone (red), Frobisher dolostone (blue) and another rock of Frobisher below the reservoir zone (black). The differences between the first three of these $\rho(V)$ dependencies are small and also lie within a residual variance of a single common trend within the reservoir (grey line in

Figure 5.4b). The data below the reservoir (black in Figure 5.4b) suggest a sharply contrasting, opposite $\rho(V)$ trend. However, these points come from only a narrow depth interval near the end of the density well log, and they may simply represent a limited sampling of the variance of density values.

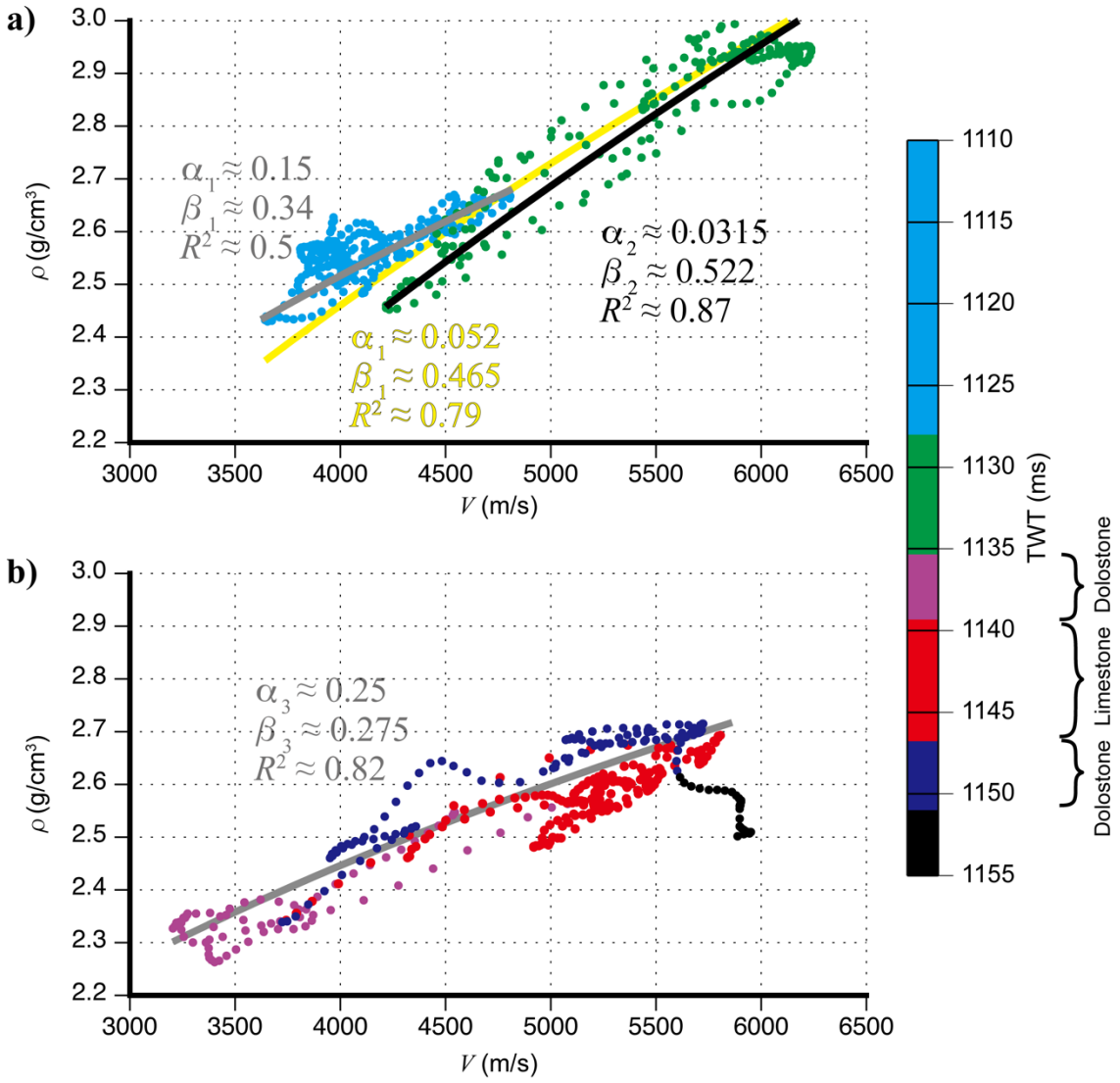

Figure 5.4. Cross-plots of P-wave velocities and densities from well 102042300614 (symbols) and the interpreted relations of equation (5.9) (lines): a) above the reservoir, b) inside and below the reservoir. Symbol colors correspond to the two-way travel time ranges shown by the color bar. The reservoir zone of Marly dolostone and Vuggy limestone are indicated.

Thus, for the AI inversion in the following subsections, I use the three-layer $\rho(V)$ model shown by lines in Figure 5.4. Although the separation of layers and estimation of parameters α and β in equation (5.9) are non-unique, the combined $\rho(V)$ model represents a reasonable and consistent velocity-density trend within and above the reservoir (Figure 5.4). The residual scatters in density values may be substantial (about ±0.05 to 0.1 g/cm^3; Figure 5.4), but they commonly occur due to rock variability and are unavoidable. At the same time, this variability should not affect TL observations with the same rock. In the absence of reliable data, below the reservoir, I use velocity/density trend inferred for the single-layer model above the reservoir by choosing one fitting curve for all data points (yellow line in Figure 5.4a).

5.2.3 AI inversion

I calculate the baseline AI and TL AI difference using the well-log based calibration method by Morozov and Ma (2009). Although effectively performing what is usually called "AI inversion" from reflection seismic records, this method contains no inverse algorithms and tuning parameters and is implemented by multiple filtering of AI columns derived from seismic and well-log records. Analogous to the source-wavelet estimation in Chapter 3, determination of the AI from reflection seismic data is a fundamentally ill-posed inverse problem, and multiple AI models can perfectly fit the data. Also similar to the approach in Chapter 3, the resulting AI is sought as predicting the observed reflectivity plus satisfying several additional requirements, which are important for physical and geological interpretation of this quantity. In the method by Morozov and Ma (2009), the key requirements of the resulting physically-interpretable AI section are:

A) The amplitude spectrum must match that of the well-log AI located near the imaging location,

B) Below the seismic frequency band, the AI at the available well-log locations must also match the one derived from these logs, and

C) Within the entire study area, the spatial pattern of predicted reflectivity must match that of the seismic volume.

In addition to these requirements, I further require that:

D) The resulting 3-D AI cube matches the spatially-variable low-frequency AI model from the preceding subsection. In this way, the resulting AI model would attain the depth and large-scale lateral variability, which is impossible to obtain from either the seismic data or the one available well log.

To add constraint D) to the algorithm by Morozov and Ma (2009) (tool "synlog" in IGeoS package; Morozov (2008)), I produce an AI "pseudo-log" at each point where the stacking and interval velocities are determined, and use these pseudo-logs as well logs. The pseudo-logs are obtained by merging the AI columns calculated from the interval-velocity profiles (preceding subsection) with the AI from the available well logs. By using a 100-ms sliding Hanning time window, the interval-velocity AI (Z_{vel}) and well-log AI (Z_{log}) are separated into lower- and higher-frequency components: $Z_{\text{vel}} = Z_{\text{LF-vel}} + Z_{\text{HF-vel}}$ and $Z_{\text{log}} = Z_{\text{LF-log}} + Z_{\text{HF-log}}$. The resulting pseudo-log at each location is then obtained by replacing the high-frequency part of Z_{vel} with that of Z_{log}:

$$Z_{\text{pseudo-log}} = Z_{\text{LF-vel}} + Z_{\text{HF-log}}\,. \tag{5.11}$$

Figure 5.5 shows the detailed calculation of $Z_{\text{pseudo-log}}$ (equation (5.11)) at one location near well 102042300614. Below about 1370 ms, no well logs are available, and the Z_{log} is extended with a constant value (Figure 5.5b). Morozov and Ma (2009) also experimented with extending the depths of AI variations below the deepest borehole coverage by using random AI layering. However, I do not consider such extensions in this study.

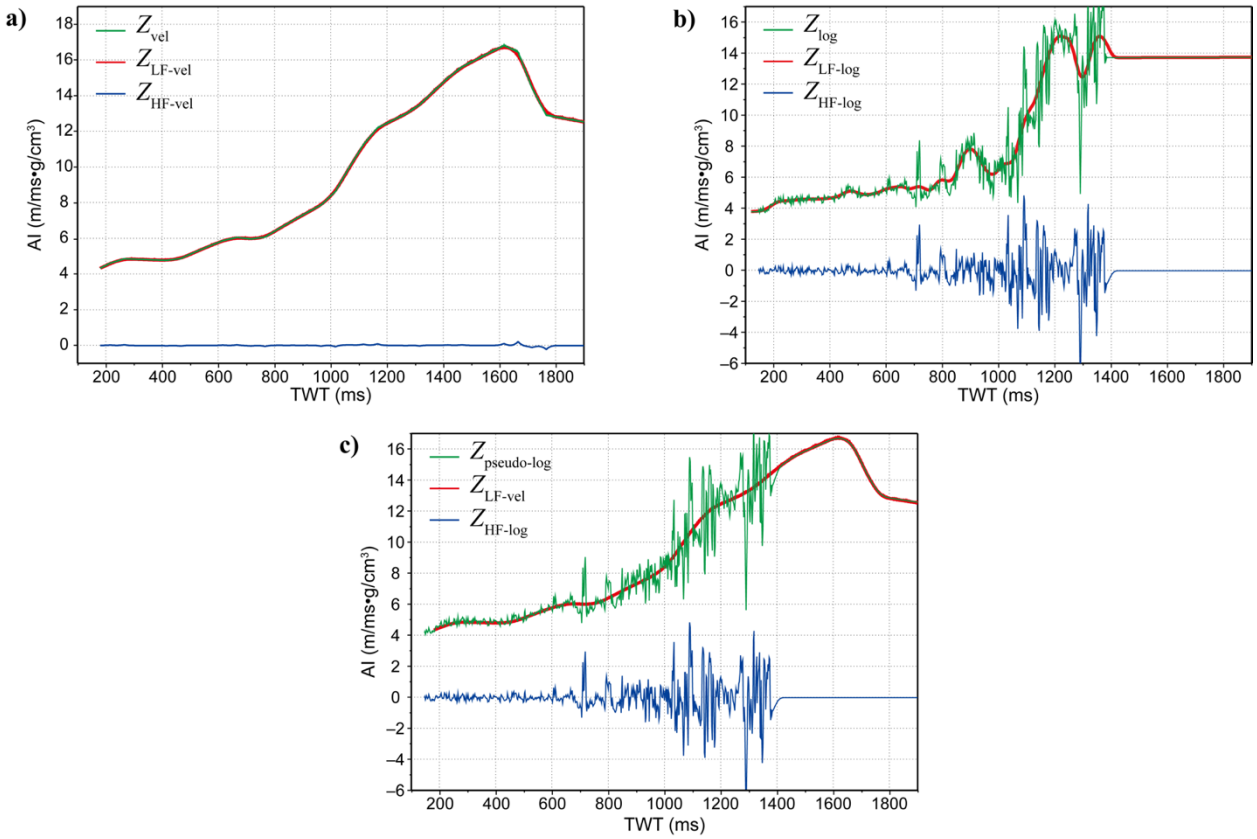

Figure 5.5. Calculation of AI pseudo-logs: a) AI calculated from interval velocity (Z_{vel}) and its low-frequency ($Z_{LF\text{-}vel}$) and high-frequency ($Z_{HF\text{-}vel}$) components after Hanning filter (labeled); b) AI calculated from well 102042300614 (Z_{log}) and its low-frequency ($Z_{LF\text{-}log}$) and high-frequency ($Z_{HF\text{-}log}$) components (labeled); c) AI pseudo-log ($Z_{pseudo\text{-}log}$; green line), which is the sum of $Z_{HF\text{-}log}$ (blue line in b))and $Z_{LF\text{-}vel}$ (red line in a)).

In the AI inversion procedure by Morozov and Ma (2009), the pseudo-logs are first interpolated by using the Delaunay triangulation into the position of each stacked seismic trace. The interpolation is performed along a series of picked horizons, for which I used the caprock and base of the reservoir and Bakken reflection (Figure 2.4). In this way, the major layering shown by the well log is preserved and the spatial variability of the seismic-processing model is incorporated in the model. Finally, the AI derived from the seismic trace is merged and calibrated by the interpolated pseudo-log, producing an AI volume satisfying the requirements A)–D) above (Morozov and Ma, 2009).

As mentioned in section 5.1, a key difficulty in any AI inversion is the lack of low-frequency information in reflection seismic data, which causes uncertainties in AI scaling and large-scale variations. It is therefore important to evaluate whether and how the present inversion procedure (Morozov and Ma, 2009) is able to resolve this problem. To evaluate this problem quantitatively, Figure 5.6 shows the amplitude spectra of the calculated $Z_{\text{LF-vel}}$ and $Z_{\text{pseudo-log}}$ (equation (5.11)) and a seismic trace near well 102042300614. For convenience of their comparison, all three spectra are scaled to equal peak amplitudes. By taking levels of 30 dB below the peak amplitudes, grey shading in Figure 5.6 indicates the estimated frequency bands in which the low-frequency model AI ($Z_{\text{LF-vel}}$; $\sim 0 - 3$ Hz) and the seismic AI ($\sim 7 - 90$ Hz) are dominant. Thus, seismic data do not contribute to the AI image below about 7 Hz, and the key question is whether the model contains an unconstrained frequency gap (Yuan et al., 2019), such as the white zone between 3 to 7 Hz in Figure 5.6. However, the result of the method by Morozov and Ma (2009) consists in producing an AI section with amplitude spectrum matching the pseudo-log $Z_{\text{pseudo-log}}$ (properties A) and B) above; red line in Figure 5.6). This spectrum is continuous across the gap and above the noise level at all frequencies. Therefore, this AI

inversion method produces a unique and broadband impedance time series without uncertainties and unconstrained gaps in the frequency range.

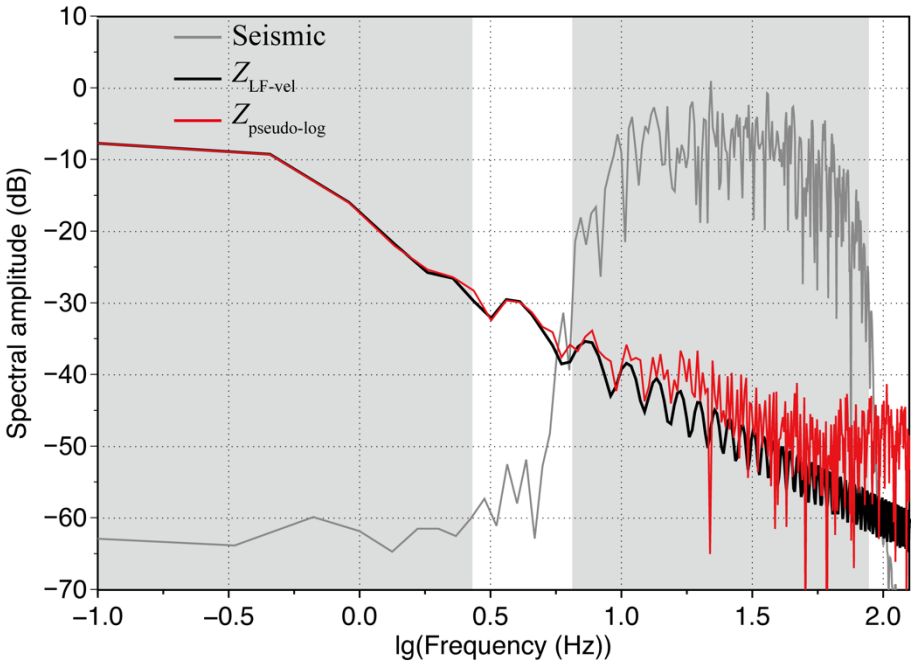

Figure 5.6. Amplitude spectra of seismic data (gray line), $Z_{\text{LF-vel}}$ (black line) and $Z_{\text{pseudo-log}}$ (red line). Gray areas indicate the low-frequency range (left) and seismic bandwidth (right).

5.2.4 Time-lapse AI difference

The TL AI difference can be evaluated by subtraction of independently evaluated monitor and baseline AIs. However, subtraction of close time series is prone to noise and computational instabilities (the low-frequency drift corrected by well-log calibration), and it could therefore contain undesirable noise. To avoid such subtraction noise, I therefore use equation (4.12b) and evaluate the AI difference directly from the reflectivity difference. By using equations (5.3) and (4.12a), the ratio of the calibrated monitor AI (denoted Z_{cmon} below) and baseline AI (Z_{bas}) equals

$$\frac{Z_{\text{cmon}}\left(t_0\right)}{Z_{\text{bas}}\left(t_0\right)} = \exp\left[2\left(\int_0^{t_0}\frac{r_{\text{cmon}}}{\gamma_{\text{v}}}d\tau - \int_0^{t_0} r_{\text{bas}}\, d\tau\right)\right] \approx 1 + 2\int_0^{t_0} r_{\text{dif}}\, d\tau\,. \tag{5.12}$$

In this integration, the scaling uncertainty and low-frequency instability (equation (5.3)) should not be a problem, as this integral is effectively taken over a narrow time range of the reservoir zone, and $r_{\text{dif}} \approx 0$ outside of this zone. Finally, from equation (5.12), the TL AI difference equals

$$Z_{\text{dif}}\left(t_0\right) = Z_{\text{cmon}}\left(t_0\right) - Z_{\text{bas}}\left(t_0\right) \approx 2Z_{\text{bas}}\left(t_0\right)\int_0^{t_0} r_{\text{dif}}\, d\tau. \tag{5.13}$$

Thus, the AI difference can be evaluated by multiplying the baseline AI (Z_{bas}) and another AI-type quantity obtained from r_{dif} (equation (4.12b)) by any suitable method.

Interestingly, equation (5.13) presents the impedance difference as a product of two impedance-type time series. It therefore may appear that the result is nonlinear with respect to reflectivity. For example, if we imagine that all reflectivities are multiplied by factor c, the result of equation (5.13) should be multiplied by c^2. Nevertheless, equation (5.13) is still correct and no such nonlinearity takes place. As expected, the output of equation (5.13) is linear with respect to the time-lapse reflectivity difference r_{diff}, and the factor $Z_{\text{bas}}(t_0)$ is in fact scaled by the scaling relations for impedance and by the procedures correcting for the low-frequency instability (section 5.1).

5.3 Results

In this section, the methods described in section 5.2 are applied to the vertical component of the 3-D 3-C datasets from the Weyburn-Midale Monitoring and Storage project (Chapter 2) and baseline and TL AI volumes are obtained.

Figure 5.7 shows a vicinity of the reservoir in crossline 40 (gray dashed line in Figure 2.3b and Figure 4.3) from the stacked baseline reflection records and AI obtained by the method of the preceding section 5.2. The stacked seismic dataset (amplitude in arbitrary scaling; Figure 5.7a) is of good quality, and with the use of seismic-processing velocities and well log, baseline AI in Figure 5.7b shows the (moderate) spatial variations of the velocity-density layering (as opposed to seismic dataset in Figure 5.7a) within the study area.

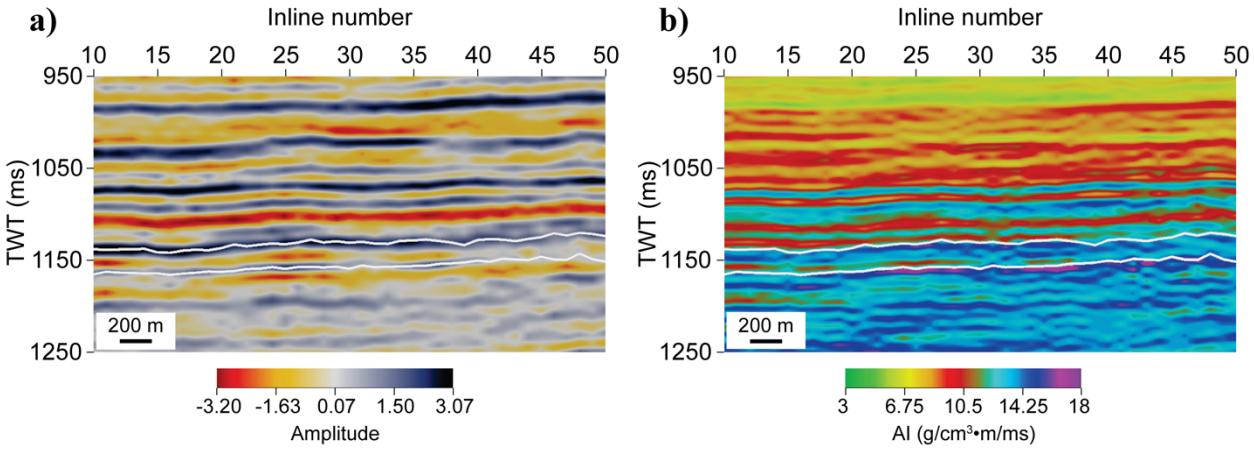

Figure 5.7. Cross-sections of the baseline data along crossline 40: a) stacked seismic records; b) AI. White lines are the caprock and bottom horizons. Marly reflection (negative polarity) is indicated in plot a).

By using the baseline AI and reflectivity difference evaluated by equation (4.12b), Figure 5.8 shows the relative variations of AI (Z_{dif} / Z_{bas}) within the Marly and Vuggy zones of the reservoir. These relative AI variations are averaged within the TL AI volumes by using time windows (4-ms for Marly and 8-ms for Vuggy) below the corresponding reflection time picks. For the interval velocity of about 4500 m/s, these windows correspond to approximately the entire respective intervals. Within both reservoir zones, negative AI variations consistent with CO_2-injection patterns are seen, particularly in the SE part of the study area (Figure 5.8). The

decrease of AI is stronger in 2002 than in 2001, similar to the TL reflectivity difference on Marly (Figure 4.5).

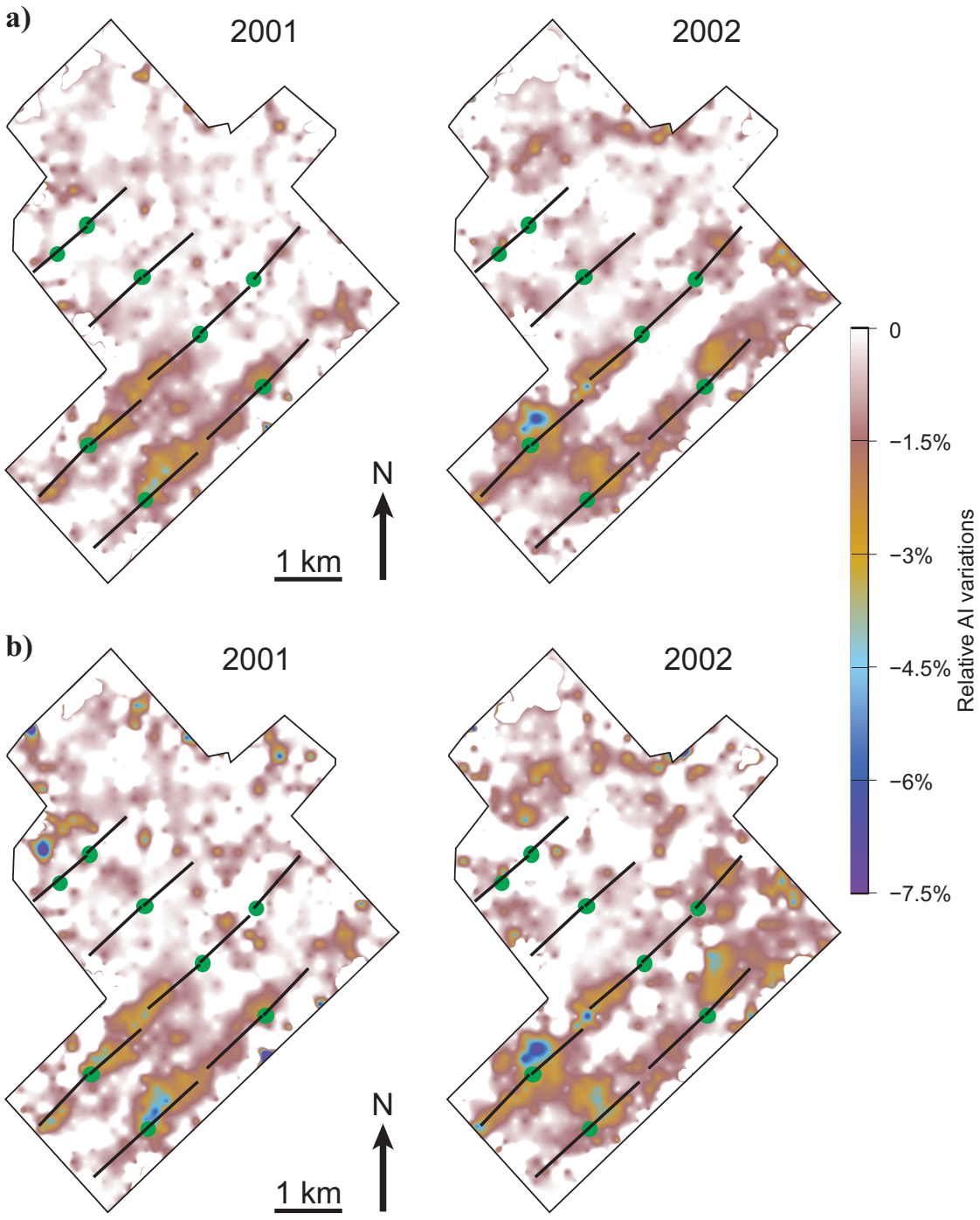

Figure 5.8. Relative AI variations (Z_{dif} / Z_{bas}) between calibrated monitors (labeled) and baseline on a) Marly and b) Vuggy

In the vicinities of the horizontal injection wells, AI decreases of about 3% are seen within both Marly (Figure 5.8a) and Vuggy (Figure 5.8b) zones. By detailed comparison of Figures 5.8a and 5.8b, we observe that the AI decreases are more diffuse around injection wells in Vuggy, especially in 2002. These AI decreases in Figure 5.8 and of broader extent in Vuggy are due to CO_2 injected in Marly and then penetrate and spread within the underlying Vuggy with higher permeability. By contrast, these AI decreases in Marly or Vuggy are much smaller than the TL AI variation of 5% to 15%, which is expected from equation (5.10) with the P-wave velocity decrease estimated from time shifts (Figure 4.3). These estimates are consistent with the maximum decrease in AI of about 12% estimated by White et al. (2011) from another TL reflection seismic dataset in this area. The stronger TL effect on the time shifts (4–12% velocity decrease from Figure 4.3) compared to that on the AI (~3% decrease in Figure 5.8) could be explained by CO_2 penetrating beneath the Vuggy zone. This question is further considered in section 5.4 .

Herawati and Davis (2002) also estimated AI decreases from other TL datasets of Weyburn Field by direct subtraction of AIs estimated from sparse-spike inversion of different vintages. They showed that the maximum AI decrease in Marly is more than 6%, which is larger than my estimation (Figure 5.8b). However, in Vuggy, their estimation of AI decrease is less than 5%, which is consistent with my result (Figure 5.8c).

Finally, I compare the TL AI difference derived from equation (5.13) for monitor 2002 dataset with the AI difference obtained by subtracting the independently-obtained AIs of the baseline and calibrated monitor 2002 datasets (Figure 5.9). Prior to AI calculation, the reflectivity in the monitor dataset was corrected for time stretching as in equation (4.12a). As expected, the differential-AI approach (equation (5.13); Figure 5.9b) provides a considerably

clearer result, with lower spurious noise, stronger TL responses, and better correlations with injection-well patterns and time shifts in Figure 4.3b.

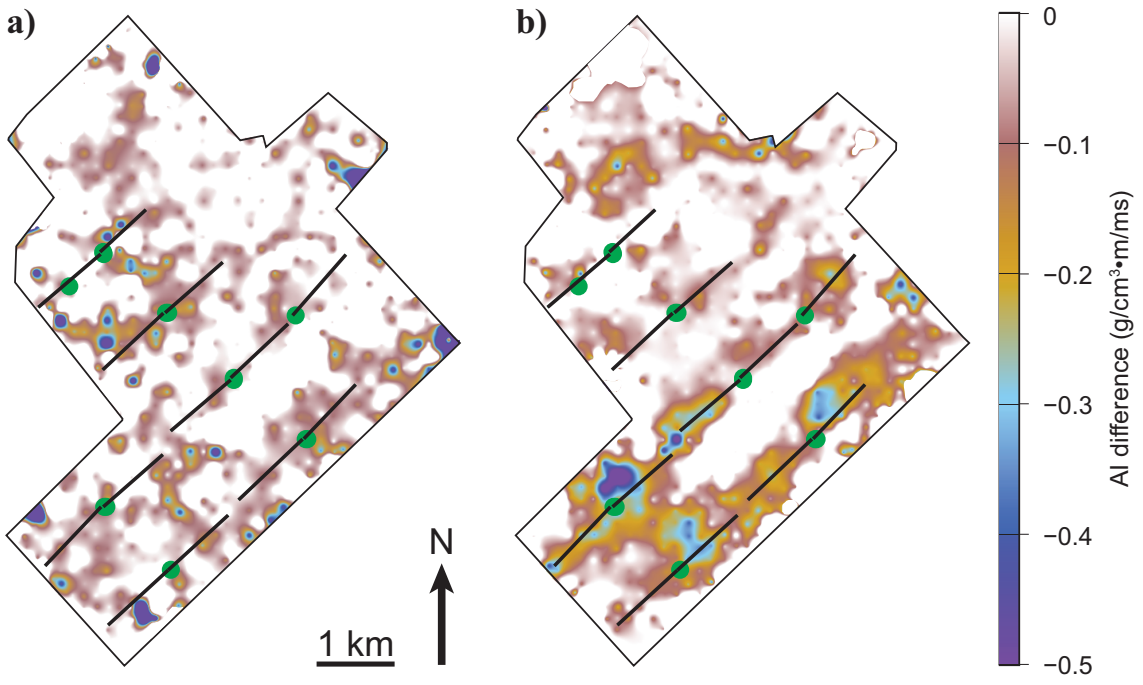

Figure 5.9. AI differences between calibrated monitor 2002 and baseline, measured within a 4-ms window below the Marly reflector: a) AI difference obtained by direct subtraction and b) AI difference evaluated from baseline AI and reflectivity difference (equation (5.13)).

5.4 Discussion

Due to combining all available data (seismic records, interval velocities from seismic processing, average trends and spectra from well logs, and velocity-density relations), the inverted AI difference (Figure 5.9) likely represents the best available estimate of TL AI variations within the subsurface in this area. However, three important questions are still incompletely answered in this study, which are: 1) characterization of the uncertainties of the resulting images, 2) potential effects of attenuation, and 3) relation of AI and attenuation to rock

physics, and in particular, separation of the effects of pore pressure and CO_2 saturation within the reservoir. In this section, I comment on these general questions, which are also relevant to many other TL and AI studies.

The general problem of AI inversion from reflection seismic data is under-constrained, which means that there exist multiple AI models that can accurately predict the observed reflectivity (e.g., Lindseth, 1979). This uncertainty is greatly increased when layering at sub-wavelength scale and/or seismic attenuation are included in the model. For example, in post-stack imaging, practically any attenuating medium can be modeled by purely elastic fine layering, and in oil and gas reservoirs, both intrinsic and scattering attenuations are usually present. Both of these attenuations are strong in the Weyburn reservoir area (Baharvand Ahmadi and Morozov, 2013) and contribute to the under-constrained character of AI models. In addition, various types of acquisition and processing noises further increase the inherent uncertainties of the AI and TL AI volumes.

Because of its under-constrained character, the AI model shown in Figure 5.8 and Figure 5.9 can be viewed as one of many models predicting the reflectivity data (practically) exactly but selected among other acceptable models based on some additional (sometimes called "regularization") criteria. In the popular joint, statistical, and full-waveform inversion methods (e.g., Tarantola, 2005; Buland and Ouair, 2006; Yuan et al., 2019), regularization criteria require the proximity of the solution to some prior model. The AI solution is largely determined by the selection of the prior model and the data misfit norm, and also by the assumed statistical properties of possible models, such as their uncorrelated Gaussian distributions. These assumptions allow performing the inversion directly in terms of rock and/or pore-fluid properties (e.g., Grana and Mukerji, 2015). Nevertheless, all these assumptions are still hypothetical,

because 1) the layered structure of a real thin reservoir is not statistical, 2) there actually exists no prior model, and 3) we only deal with a single realization of reflectivity, which can be accurately matched by the basic seismic constraints such as equations (5.2). By being forced toward some subjective prior model, joint and statistical-inverse AI solutions no longer accurately satisfy the seismic constraints and intermix the uncertainties of the seismic, rock-physics, and mathematical aspects of the problem. Thus, joint and statistical AI inverses are inherently biased by their regularization, although the meaning of this bias is difficult to specify in each particular case (Morozov and Ma, 2009). In another type of regularization, sparse-spike AI inversion (Herawati and Davis, 2002) achieves unique AI solutions by assuming constant impedances within wavelength-scale layering.

In contrast to the above subtleties of joint inversion, in the approach of this paper, we perform the AI inversion accurately, with regularization consisting in purely seismic constraints from well-log and seismic-processing observations (section 5.2). These criteria do not bias the solutions from satisfying the seismic constraints (equations (5.2)), and the inversion requires no prior models or assumptions about model statistics (Morozov and Ma, 2009). The only (yet significant) source of errors and uncertainties is the effect of data noise and TL acquisition and processing inaccuracies. To evaluate this effect, let us return to Figures 4.2c or 4.2d and view the distribution of reflectivity differences r_{diff} outside of the reservoir zone (in which r_{diff} is ideally expected to be zero) as data errors. By drawing uncorrelated random values $\varepsilon_{r\text{diff}}$ from this distribution, we can form synthetic reflectivity profiles $r'_{\text{diff}}(t)$ for the reservoir:

$$r'_{\text{diff}}(t) = r_{\text{diff}}(t) + \varepsilon_{r\text{diff}}, \tag{5.14}$$

where $r_{\text{diff}}(t)$ is the inverted TL reflectivity series at one selected midpoint within the reservoir (Figure 4.2c). By using equation (5.14) and performing 500 random trials, probability densities of impedances Z'_{diff} at each time t are estimated (Figure 5.10a). Because the solution $Z_{\text{diff}}(t)$ (black line in Figure 5.10a) satisfies the seismic inverse problem (equations (5.2)), the mean values of Z'_{diff} at each t (red dashed line in Figure 5.10a) are close to $Z_{\text{diff}}(t)$. The variance of Z'_{diff} varies from about 0.04 g/cm^3·m/ms at the top to about 0.1 g/cm^3·m/ms at the bottom, which is much smaller than, for example, the typical errors from statistical inversion (Grana and Mukerji, 2015). Therefore, the inverted variations of $Z_{\text{diff}}(t)$ (black line) are well constrained.

Figure 5.10 also shows two additional properties of AI in the presence of random variations of reflectivity, which may be useful for statistical AI inversion. First, note that the variance of Z'_{diff} at each time increases from the top to the bottom of the model (Figure 5.10a). This loss of statistical confidence with increasing depth should be due to the low-frequency instability described in the section 5.1, which leads to "drifting" $Z_{\text{diff}}(t)$ profiles. Second, Figure 5.10b shows that as expected, the statistical distributions of Z'_{diff} at two consecutive time levels (two sides of a reflector) are strongly correlated. Similar to the AI, rock physics parameters should likely also be statistically correlated between layers. Thus, it appears that it might be useful to use spatially-correlated and depth-dependent model distributions of physical properties in joint and statistical inversions.

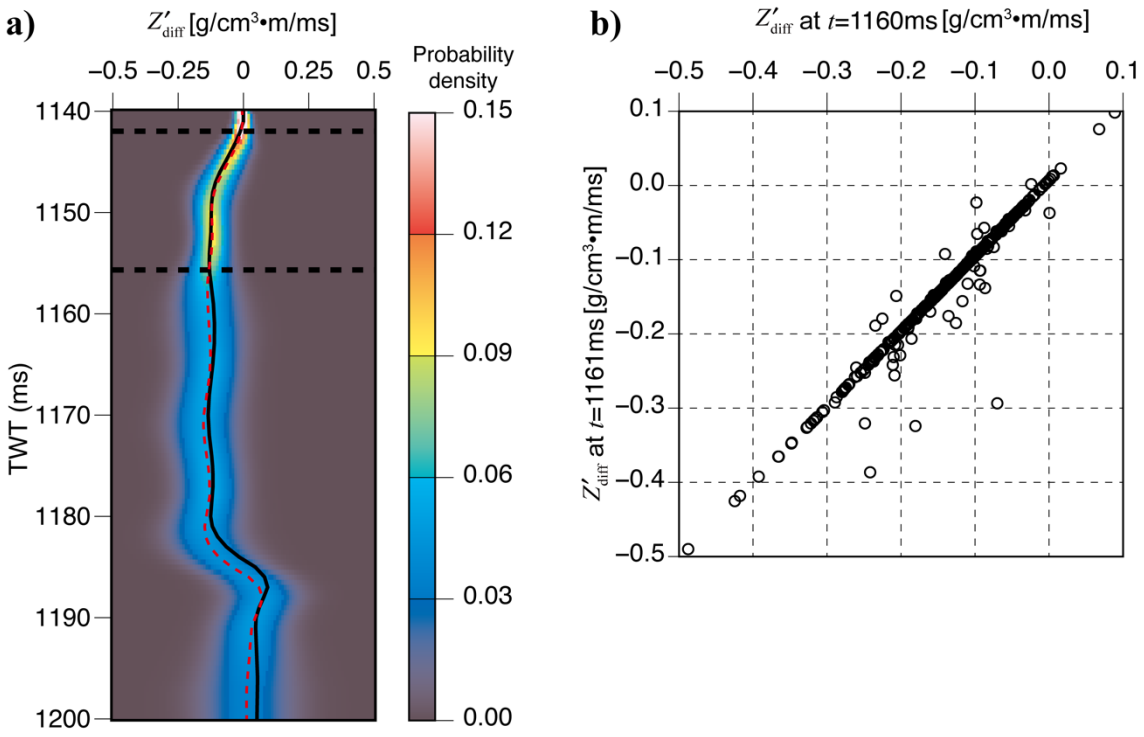

Figure 5.10. Simulated TL AI uncertainties at crossline 40, inline 35 in monitor 2002 results: a) Probability density for Z'_{diff} values (color bar); b) Cross-plot of Z'_{diff} distributions at two consecutive time levels of 1160 and 1161 ms. Black solid and red dashed lines in a) are the inverted $Z_{diff}(t)$ and mean values of Z'_{diff}, repectivly. Black dashed lines indicate the reservoir interval.

Another potential uncertainty in our AI model is related to the limited spatial sampling of its "pseudo-logs" columns (section 5.2). This type of uncertainty can be tested by the blind-well method, i.e. by removing one of the pseudo-logs and comparing the inverted result with it. However, due to the relatively smooth stacking-velocity model (Figure 5.1), its Delaunay interpolation (Morozov and Ma, 2009) should produce a good approximation for any of the pseudo-logs. Consequently, blind well testing was deemed unnecessary in this case.

After solving the TL AI inversion problem (Figure 5.8 and Figure 5.9), there still remains a significant uncertainty of its rock-physics interpretation. Detailed modeling and inversion are still required in order to understand the effects caused by the sub-wavelength thickness of the reservoir and its layering, seismic attenuation, trade-off between the effects of reservoir pressure and CO_2 saturation, and also significant variations of porosity and permeability within the Vuggy and Marly zones. Landrø (2001), Buland and El Ouair (2006), Dadashpour el al. (2008), Grana and Mukerji (2015), and other authors proposed models for inverting pressure and saturation changes from TL reflectivity and AI variations. The pressure and saturation effects can generally be constrained by considering angle- or ray-parameter dependent elastic impedances (e.g., Santos and Tygel, 2004). However, prestack effects are complicated by high compressibility of CO_2, which leads to weak sensitivity of AVO effects to CO_2 saturation above about 3% (Ma and Morozov, 2010; Baharvand Ahmadi et al., 2011). These complex phenomena require further research.

An important observation and also uncertainty of the model is the possibility of CO_2 being present outside of the reservoir zone, as suggested by White (2013a) and also by Figures 4.2c and 4.2d in this study. As estimated in section 4.3 , the TL P-wave velocity reduction ranges from about 4% to 12% (maximum decrease of 15% by White, 2013a), but the maximum P-wave velocity reduction predicted for Weyburn samples by Gassmann-equation fluid substitution is only about 6% (Brown, 2002). This discrepancy could be due to the potential existence of CO_2 outside of the reservoir zone. The Frobisher carbonates beneath the reservoir are likely be affected by the injected CO_2 because they have similar porosity to the overlying Midale reservoir, and the possible seal of Frobisher evaporite is absent in the monitoring area (Chapter 2; Figure 2.2). Finally, other factors could also amplify the TL signature, such as the

pore-pressure induced P-wave velocity reduction, which can be as high as 6 to 11% (Brown, 2002), or limitations of Gassmann's equation for partial saturation of CO_2 (Baharvand Ahmadi et al., 2011).

5.5 Conclusions

In this Chapter, a method for calculating the time-lapse (TL) acoustic impedance (AI) is developed. This method consists of constraining a spatially-variable, low- frequency AI by using interval-velocity model derived from stacking-velocity picks, measuring velocity-density relations in well logs, well log data from available wells, and reflection horizons identified within the 3-D volume. By combining this information, accurate and stable estimates of the baseline AI and TL AI difference are performed.

In the CO_2 sequestration study within the Weyburn oilfield, TL variations of the AI are delineated for two monitor datasets (Chapter 2). Reductions of the AI by about 2 to 4.5% in Marly and about 3% in Vuggy over three years of injection are spatially correlated with injection patterns and interpreted as caused by increases in CO_2 content and/or reservoir pore pressure. Compared to the P-wave velocity decrease of about 4% to 12% determined from TL time shifts (Chapter 4), it is suggested that the Frobisher carbonates beneath the reservoir should also likely be affected by the injected CO_2.

CHAPTER 6

SEISMIC RESPONSES OF LAYERED LINEAR ANELASTIC SOLIDS

In contrast to the rest of this dissertation, this Chapter presents a pure modeling study, and on a topic practically not studied in the literature. This Chapter presents the first attempt of modeling seismic wavefield in layered media by rigorous wave mechanics, in contrast to the conventional viscoelastic (VE) methods used in most current approaches. This study was inspired by the recent paper by Morozov and Deng (2018b), in which it was shown that wave propagation in finely layered media may not be simply VE. In particular, Morozov and Deng (2018b) showed that non-VE wave modes and boundary conditions need to be considered within layered structures.

In keeping with the studies of the Weyburn reservoir, the wavefield modeling in this Chapter is performed for a detailed 1-D structure based on the same acoustic and density logs from well 102042300614 (Chapter 2) as used in other chapters of this dissertation. The presentation in this Chapter is based on the following papers:

Wang, Y., *and I. B. Morozov, 2019, Modeling Seismic Waves in Layered Anelastic Media – beyond the Viscoelastic Approach: GeoConvention 2019, CSPG/CSEG/CWLS, Abstract, https://www.geoconvention.com/uploads/2019abstracts/GC2019_136_Modeling_Seismic_Waves_in_Layered_Anelastic_Media.pdf.*

***Wang, Y.**, and I. B. Morozov, submitted III, Seismic responses of layered linear anelastic solids – Wave-induced internal deformations beyond the viscoelastic model, submitted to Geophysics, in revision.*

 The texts and figures of the above papers were modified and reformatted for inclusion in this dissertation.

Similar to other chapters, section 6.1 starts with an introduction to this topic and gives a brief overview of the rest of this Chapter.

6.1 Introduction

Layered one-dimensional (1-D) models of the subsurface are often used for modeling transmission, reflection, and converted-mode seismic responses within the Earth (e.g., Fuchs and Muller, 1971; Kennett, 1983; Ursin and Stovas, 2002). The goals of such models are in accurate assessment of amplitudes, thin-layer and random-heterogeneity effects, and also effects of inelasticity, effects of fluids within rock pores (poroelasticity), liquid layers, and anisotropy. In this Chapter, I do not consider anisotropy and specific pore-fluid flows and only focus on modeling general inelastic effects. I understand the term "inelastic" as all types of physical phenomena resulting in the dissipation of mechanical wave energy into heat. Such phenomena include, for example, thermoelastic energy dissipation (Landau and Lifshitz, 1986) and Darcy friction of pore fluids within porous rock. However, within the conventional macroscopic viscoelastic (VE) models of waves in solids (for example, Fuchs and Muller (1971)), these detailed processes are not considered, and the discussions are limited to a class of

phenomenological models that usually called *anelastic* solids. For an anelastic solid, the stress is expected to be related to the strain by convolution in time, i.e. “material memory”. Therefore, anelastic media can also be defined as media with (causal) time-dependent material properties. Because of time-delayed material memory, anelastic rock exhibits phase shifts between strain and stress and consequently energy dissipation, and therefore it is inelastic.

This Chapter focuses on describing rock anelasticity, although from a perspective different from most previous studies. Numerous studies of this subject (including the above references) and most of the existing seismic-modeling software are based on the VE model, which represents the anelasticity of the medium by a frequency-dependent quality factor $Q(f)$ attributed to it (e.g., Knopoff, 1964). Q-factors are broadly used in seismic interpretation and related to reservoir properties such as porosity, saturation, presence of gas or fluids (e.g., Chen et al., 2018), and also short-scale heterogeneity.

However, despite its long history, almost unquestioned acceptance, and broad use, it is important to see that the VE model represents only one, and with that rather specific and refutable hypothesis about the rheology of anelastic rock. The VE hypothesis is based on the so-called correspondence principle, which replaces all mechanical interactions within the medium with a phenomenological “material memory” directly relating the time histories of the observed stress and strain. This principle was proposed by summarizing laboratory observations, for which it may arguably be sufficient (Lakes, 2009). However, some controversies of this model for seismic waves were also noted long ago (e.g., in section 7 of the seminal paper by Knopoff (1964)). As shown in this Chapter, the physical picture provided by the correspondence principle is incomplete and inaccurate in cases that are most important in exploration seismology: for

porous, fluid-saturated sedimentary rock, vicinities of material-property contrasts, small rock samples, waves, and particularly for waves in layered media.

Currently, there seems to be no general agreement about whether a reliable dynamically-equivalent VE model (DEVM), i.e. an approximation by effective VE media can be found for arbitrary heterogeneous rock (Solazzi et al., 2016). In numerous studies of wave-induced fluid flows (WIFF), fluid-substitution models, and in numerical modeling, an assumption of a DEVM is taken as a tacit starting point (e.g., Müller et al., 2010; Rubino, and Holliger, 2013). The DEVM assumption also represents the basis of most subresonant attenuation measurements in the laboratory (e.g., Tisato and Quintal, 2013; Pimienta et al., 2015a, 2015b). Nevertheless, some authors (White, 1986; Morozov, 2015) pointed out that the DEVM assumption is invalid for wet porous rock and recommended using the complete equations of Biot's (1956) poroelasticity. Morozov and Baharvand Ahmadi (2015) argued that also generally, VE moduli and Q-factors are apparent properties, which can be attributed to the medium only when the spatial heterogeneity is either absent (in uniform media) or disregarded (as in experiments with small rock samples). By using numerical simulations of heterogeneous poroelastic media, Milani et al. (2016a) showed that defining a DEVM requires selecting sufficiently large, macroscopically-uniform reference elementary volumes (REV) in which the REV-scale pore-fluid flows and secondary waves are insignificant. To ensure the absence of secondary waves, the REV should also be located far from any material-property contrasts. However, such boundless quasi-uniform media are rare in practice, where significant material-property contrasts and reflecting boundaries occur at the scales of secondary-wave skin depths (~10–50 cm). In laboratory attenuation experiments, when skin depths are comparable to the dimensions of the samples, strong "drained/undrained transitions" (DUT) may dominate the observations (Pimienta et al., 2015a, 2015b). In a layered

rock sequence, the DUT is caused by non-VE effects (interlayer flows) and may be pervasive (Milani et al., 2016b). Consequently, in a layered Earth or within a laboratory sample, secondary waves are often present, and the "material memory" and Q-factors do not exist locally but result from spatial deformations of the entire structure. For heterogeneous poroelastic rock, the uncertainty of the notion of "local" VE Q may include almost the entire effect of attenuation (Dunn, 1987; Morozov, 2015).

Thus, for accurate wave modeling in non-uniform anelastic media, first-principle mechanics including DUT-type effects and secondary wave modes should be used. In this Chapter, I show that such modeling is feasible and relatively straightforward, but it requires knowledge of rock properties other than its Q-factors. The approach is demonstrated by modeling reflected and transmitted seismic responses of the layered Weyburn oil reservoir (Chapter 2).

This Chapter is organized as follows. In section 6.2, I further illustrate the shortcomings of the VE model for layered rock and explain the rationale for studying non-VE phenomena. In this section, I also point out a fundamental analogy between pore-fluid flows in porous rock (WIFF) and internal friction within arbitrary media. By analogy with WIFF, I refer to such effects within arbitrary media as "wave-induced internal deformations" (WIID), so that WIFF becomes its special case for media containing fluids.

In section 6.3, I give the differential equations and wavemode solutions for an arbitrary layered medium with WIID, and in section 6.4, I discuss the parameterizations of material properties and boundary conditions. Because mechanical rheologies for Earth's media are poorly known (only several estimates made recently by Deng and Morozov (2016), Morozov et

al. (2018a), and Deng and Morozov (2018a, 2018b)), I model each layer by a versatile mechanical structure known as the standard linear solid (SLS; e.g., Carcione, 2007). The parameterization of layers by SLSs also highlights the similarity with many recent models and estimates of Q-factors from seismic data (e.g., Chen et al., 2018; Qadrouh et al., 2018). SLS structures are often used to approximate basic anelastic phenomena such as squirt flows or WIFF (e.g., Lakes, 2009; Tisato and Quintal, 2013; Pimienta et al., 2015a, 2015b), and I select their parameters so that they approximate DUT effects within the layers. In addition, I compare the results to direct modeling by non-VE, body-force internal friction.

Further, in section 6.5, reflected and transmitted seismic responses including both primary and secondary waves are modeled by using several types of anelastic boundary conditions. In VE models, anelastic-boundary effects are disregarded, and the VE theory contains no mechanism for boundary conditions on internal variables (e.g., Carcione, 2007), and it is also assumed that no secondary (non-VE) wavemodes exist within the medium. Nevertheless, from physical and experimental viewpoints, non-VE wavemodes should exist, and anelastic boundary effects such as DUT may dominate the observations.

In section 6.6, several types of empirical (apparent) Q values are measured in the modeled wavefields. With each layer being either elastic or an SLS, the stack of layers behaves as a generalized SLS (GSLS), i.e. produces a broad band of $Q^{-1}(f)$ and the corresponding wave-velocity dispersion spectrum. In this section, I also analyze the meaning of the popular partitioning of the empirical Q^{-1} into intrinsic, scattering, and other inverse-Q factors (e.g., Gurevich et al., 1997; Tisato and Quintal, 2013). Finally in section 6.7, I discuss several implications of the results for parameterizations of anelasticity in seismic models.

6.2 Wave-Induced Internal Deformations

Biot's (1956) poroelastic theory, its extensions, and numerous models of wave-induced fluid flows (WIFF) suggest guiding principles for describing mechanical effects within rock. Most importantly, these theories show that anelastic effects are always caused by excitations of certain internal degrees of freedom within the medium. I will refer to such media with internal deformation variables as "multi-component." For example, creep within granular solids results from groups of grains moving relative to each other, and relaxation of a fluid-saturated rock body occurs by means of expanding pores and/or fluids moving through them. Memory variables used in finite-difference seismic modeling algorithms (Day and Minster, 1984) also represent internal deformations, although presumed unobservable and governed by purely mathematical, postulated relations.

Another general observation from all WIFF theories shows that if considering mechanical phenomena at constant temperature, viscosity is ultimately the only physical mechanism causing internal friction (Landau and Lifshitz, 1986). This observation has a profound significance restricting the possible forms of WIID friction. In macroscopic mechanical media, linear viscous interactions can take on only two forms: body-force friction (leading to Darcy's law and caused by the material-property matrix denoted $\mathbf{d}$ in section 6.3) and Cauchy stress (Navier-Stokes law; material properties denoted $\boldsymbol{\eta}$ there). Combinations of parameters $\mathbf{d}$ and $\boldsymbol{\eta}$ yield all physically-implementable VE and poroelastic systems, including double- and multiple-porosity and permeability models (Morozov and Deng, 2016a, 2016b). In particular, all conventional VE models are obtained by taking $\mathbf{d} = \mathbf{0}$ and selecting certain forms of matrix $\boldsymbol{\eta}$, and Biot's model is the case $\boldsymbol{\eta} = \mathbf{0}$ and a specific form of matrix $\mathbf{d}$ (with one internal variable).

Following the analogy with WIFF, we also need to consider some classification of WIID effects. WIFF phenomena are usually categorized by the spatial and temporal scales of pore-fluid flows. For example, Ba et al. (2017) propose the following classification:

1) "type I" local WIFF (WILFF) denotes the phenomena related to flows within rock fabric and micropores, such as in squirt-flow models (e.g., Murphy et al., 1986).

2) As "type II" WILFF, Ba et al. (2017) classify mesoscopic-scale phenomena, such as caused by patchy saturation or heterogeneous material properties (e.g., White, 1975).

3) Ba et al. (2017) also define the "type III" WILFF representing a superposition of types I and II.

4) In addition, the "global" WIFF type is represented by the wavelength-scale attenuation/dispersion effects caused by inertial forces in Biot's (1956) model.

Note that the above classification is only based on fluid-flow patterns in certain theoretical models, such as squirt flows in identical, isolated, planar micropores in a quasi-uniform medium. Within real rock, all of the above types of WIFF should overlap and operate together. In particular, the key causal attenuation mechanism considered in this Chapter is DUT, which can be viewed as type II WIFF above, but likely with some contributions from types I and III and occurring through global flows across the whole layers. A similar mixed-type WIFF by interlayer flows in permeable, periodically-layered media was modeled by Milani et al. (2016b). Yao et al. (2015) proposed a model in which DUT-type effects occur at the microscopic-pore level, and thus they again overlap with both types I and II WIFF. Thus, instead of elaborate classifications by flow patterns, it would be easier and completely unambiguous to characterize

attenuation regimes by the values of the mentioned material-property matrices $\boldsymbol{\eta}$ and **d,** and also by the properties of layer boundaries (section 6.4).

Biot's poroelastic model also illustrates the reason for DEVM approximations (anelasticity parameterized by Q-factors) being limited for seismic waves. Although such approximations for Biot's model are well known (Geertsma and Smit, 1961), they are limited to simulating the shapes of the $Q(f)$ and velocity-dispersion spectra for a single pair of primary P or S waves in boundless uniform media. Nevertheless, secondary (pore-flow related, diffusive, or "slow") waves also exist and are important in many cases. For example, White (1975), Gurevich et al. (1997), and Carcione and Picotti (2006) modeled the effects of secondary waves on attenuation in layered media, Castagna et al. (2003) pointed out the low-frequency tuning and shadows beneath gas reservoirs, and Chabyshova and Goloshubin (2014) suggested that secondary waves may be responsible for such effects. As shown in this Chapter, secondary wave modes should also be significant in *arbitrary anelastic*, layered media.

The physical accuracy of DEVM approximations in seismic-wave modeling is also compromised by disregarding the body-force friction (matrix **d**) while keeping the inertial force (as it is critical for forming waves). However, since seismic frequencies are much lower than Biot's frequency f_{Biot}, the body-force friction usually greatly exceeds the inertial force within the rock. Therefore, material property **d** should generally not be neglected in seismic modeling. The same conclusion should likely apply to other WIID/WIFF mechanisms.

Poroelastic WIFF models (e.g., White, 1975) also show that despite their conventional association with "attenuation," the total dispersion (difference between high-frequency and low-frequency wave velocities) and the corresponding peak inverse Q-factor ($\max_f\left[Q^{-1}\left(f\right)\right]$) are

actually *purely elastic effects*. These effects result from the existence of multiple elastic moduli in the multicomponent structure (Mavko and Jizba, 1991), which I call the zero- (internal) deformation (ZD) and zero-pressure (ZP) moduli (section 6.3). The ZD modulus is analogous to Biot's undrained modulus or to the adiabatic elastic modulus in thermodynamics, and the ZP modulus is analogous to the drained or isothermal moduli, respectively.

Thus, the above comparison of the general rock anelasticity with its well-understood special case (poroelasticity) suggests three recommendations for a rigorous model:

1) Body-force friction forces should not be disregarded,

2) Even when approximating the subsurface with a DEVM, layer-boundary related effects such as DUT should be considered, and

3) *Q*-factors can be measured in the resulting wave fields but not assumed to be present within the layers.

These principles are implemented in the continuum-mechanics model described in the following sections.

6.3 Mechanical Approach to Waves in Layered Media

In this section, I summarize the equations of wave propagation in a unified formulation for poroelastic and/or VE media by Morozov and Deng (2016a, 2016b). This approach, called the General Linear Solid (GLS) by these authors, consists of standard, linear Lagrangian continuum mechanics for multicomponent media (Landau and Lifshitz, 1986). The procedure of finding the wavefield in a layered medium is also standard for wave mechanics, and consists of

determining of the spectra of downward- and upward-traveling P- and S-wave modes within each layer and solving for their amplitudes by using boundary conditions. The principal difference from conventional models is that $N \geqslant 1$ wave modes are used instead of only one mode for each polarization (e.g., Ursin and Stovas, 2002).

Consider a layered 1-D structure in which all material properties only depend on depth z and are constant between depth levels $z = z_l$, where l is the number of the boundary (Figure 6.1). Within each layer, the macroscopic displacement field is described by an N-dimensional model vector $\mathbf{u}$ comprising the observable and some kinds of "internal" displacements of the REV within the medium. In the following, I use a boldface notation and uppercase subscripts for vectors in the model space and explicit vector notation and lowercase subscripts for the coordinate space. For example, $\vec{\mathbf{u}} = \begin{pmatrix} \mathbf{u}_x & \mathbf{u}_z \end{pmatrix}^T$ denotes the full wavefield representing vectors in both model and coordinate spaces, $\mathbf{u}_i$ will be the i^{th} spatial component of the model field, and $\vec{u}_J$ denotes the vector of spatial displacement of the J^{th} model-space component of the field. With $J = 1$, variable $\vec{u}_J$ represents the usual observable displacement of the REV. All of these quantities are functions of the spatial coordinates $\vec{x}$ and time t.

For linear elastic and frictional interactions within the medium, the general governing equations for the field $\vec{\mathbf{u}}\left(\vec{x},t\right)$ are (Morozov and Deng, 2016a)

$$\begin{cases} \boldsymbol{\rho}\ddot{\mathbf{u}}_i = -\mathbf{d}\dot{\mathbf{u}}_i + \partial_j \boldsymbol{\sigma}_{ij}, \\ \boldsymbol{\sigma}_{ij} = \mathbf{K}\Delta\delta_{ij} + 2\boldsymbol{\mu}\tilde{\boldsymbol{\varepsilon}}_{ij} + \boldsymbol{\eta}_K \dot{\Delta}\delta_{ij} + 2\boldsymbol{\eta}_\lambda \dot{\tilde{\boldsymbol{\varepsilon}}}_{ij}, \end{cases} \tag{6.1}$$

where indices $i,j = 1, 2,$ or 3 denote the spatial dimensions, $\boldsymbol{\varepsilon}_{ij} \equiv \left(\partial_i \mathbf{u}_j + \partial_i \mathbf{u}_j\right)\big/2$ is the strain tensor, $\Delta \equiv \varepsilon_{kk} \equiv \mathrm{tr}\,\boldsymbol{\varepsilon}$ is the volumetric strain, $\tilde{\boldsymbol{\varepsilon}}_{ij} \equiv \boldsymbol{\varepsilon}_{ij} - \Delta\delta_{ij}\big/3$ is the deviatoric strain, and summations over pairs of repeated spatial indices are implied. Tensor $\boldsymbol{\sigma}_{ij}$ (matrix in model space) is the Cauchy stress, and its divergence $\partial_j \boldsymbol{\sigma}_{ij}$ is the only type of force considered in the VE model. In poroelasticity-type models, the principal source of internal friction is the Darcy drag force $-\mathbf{d}\dot{\mathbf{u}}_i$ (first equation (6.1)). This body force is also the principal mechanism of interaction between the rock matrix and partial melt in rock compaction models (McKenzie, 1984). Material properties are represented by the density matrix $\boldsymbol{\rho}$, the bulk ($\mathbf{K}$) and shear ($\boldsymbol{\mu}$) elastic-moduli matrices, the corresponding viscosity matrices $\boldsymbol{\eta}_K$ and $\boldsymbol{\eta}_\mu$, and the Darcy drag matrix $\mathbf{d}$. All of these matrices are square, symmetric, and positive definite.

The principal advantage of the GLS equations (6.1) compared to VE ones is in explicit separation of strain-, strain-rate-, and flow-velocity related forces without mixing them into phenomenological convolutional relations between the time histories of strain and stress. Equations (6.1) are local and simultaneous (relate only quantities taken at the same point in space and time) and require no additional variables or equations for describing wave attenuation. The GLS model is defined for an arbitrary heterogeneous medium and contains no temporal scales ("relaxation times," "characteristic frequencies," or "unrelaxed moduli"). As in mechanics, all relaxation processes in this model occur by means of spatial flows, such as waves or transient deformations.

To describe the spectrum of wave modes in a layered model, the complete set of modes within each uniform layer needs to be first identified. The following derivation will apply to

either 1) conical waves in a cylindrical coordinate system (z, ϕ, r) with an axisymmetric source, or 2) plane waves in Cartesian coordinate system (z, y, x). In both of these cases, I disregard the SH waves by taking the transverse displacements equal $\mathbf{u}_\phi = 0$ or $\mathbf{u}_y = 0$ (SH waves can be considered similarly as a scalar field; cf. Kennett, 1983). The remaining variables $\mathbf{u}_z$ and $\mathbf{u}_r$ describe coupled P and SV waves and depend on the spatial variables z, r (or x), and time t. The cylindrical and Cartesian-coordinate wave solutions can be mutually related by using the forward Hankel transform followed by inverse Fourier transform (e.g., Fuchs and Muller, 1971):

$$\mathbf{u}_i\left(z,x\right) = \int_0^\infty dk_x e^{-ik_x x} \int_0^\infty dr r J_n\left(rk_x\right) \mathbf{u}_i\left(z,r\right), \tag{6.2}$$

where, J_n is the Bessel function of order $n = 0$ when transforming the vertical spatial components $\mathbf{u}_i = \mathbf{u}_z$ and $n = 1$ for horizontal components $\mathbf{u}_i = \mathbf{u}_x$ or $\mathbf{u}_r$.

By virtue of equation (6.2), the problem reduces to considering harmonic attenuating plane waves within a 1-D layered structure. Let me denote such a wave within one layer by $\vec{\mathbf{u}}\left(\vec{r}\right) = \vec{\mathbf{u}} \exp\left(-i\omega t + i\vec{k}\vec{r}\right)$, where ω is the angular frequency, $\vec{k} \equiv \begin{pmatrix} k_z & k_x \end{pmatrix}^T$ is the complex-valued wavenumber vector, k_z is the vertical wavenumber, and $\vec{r} \equiv \begin{pmatrix} z & x \end{pmatrix}^T$ is the radius vector. Thus, the wavemodes are generally inhomogeneous waves, with vectors $\mathrm{Im}\,\vec{k}$ directed differently from $\mathrm{Re}\,\vec{k}$ (Figure 6.1; Declercq et al., 2005). I refer to such complex-valued vector $\vec{k}$ as a bivector. For such harmonic wavemodes, equations (6.1) become

$$-\omega^2 \boldsymbol{\rho} \mathbf{u}_i = \left[i\omega \mathbf{d} \delta_{ij} - \left(\mathbf{K}^* + \frac{1}{3}\boldsymbol{\mu}^* \right) k_i k_j - \boldsymbol{\mu}^* \vec{k}^2 \delta_{ij} \right] \mathbf{u}_j, \tag{6.3}$$

where the matrix moduli are defined by $\mathbf{K}^* \equiv \mathbf{K} - i\omega\boldsymbol{\eta}_K$ and $\boldsymbol{\mu}^* \equiv \boldsymbol{\mu} - i\omega\boldsymbol{\eta}_\mu$ (Morozov and Deng, 2016a). For attenuating waves propagating in the positive directions of axes *X* and *Z*, both components of $\vec{k}$ and the absolute value $\left|\vec{k}\right|$ are complex-valued with non-negative imaginary parts. The horizontal wavenumber k_x is common to all layers (the Snell-Descartes law; Declercq et al., 2005), and considering waves incident from an elastic medium above the anelastic zone, $\operatorname{Im}\vec{k}_x$ can also be taken as zero.

It is further convenient to consider the longitudinal (P) and transverse (S) waves satisfying equation (6.3) separately. Following the convention for positive P- and S-wave displacements by Aki and Richards (2002) (block arrows in Figure 6.1), the corresponding polarization bivectors are denoted by $\vec{n}_{\mathrm{P}} \equiv \vec{k}_{\mathrm{P}} \Big/ \left|\vec{k}_{\mathrm{P}}\right|$ and $\vec{n}_{\mathrm{S}} \equiv \pm\vec{e}_y \times \vec{k}_{\mathrm{S}} \Big/ \left|\vec{k}_{\mathrm{S}}\right|$, where $\vec{e}_y$ is a unit vector in the transverse direction (axis *Y*), and signs '+' and '–' correspond to the downgoing and upgoing waves, respectively. In terms of projections onto the spatial coordinate axes, these relations are $n_{\mathrm{P}i} = k_{\mathrm{P}i} \Big/ \left|\vec{k}_{\mathrm{P}}\right|$ and $n_{\mathrm{S}i} \equiv \pm\varepsilon_{i1j} k_{\mathrm{S}j} \Big/ \left|\vec{k}_{\mathrm{S}}\right|$, where ε_{ijk} is the antisymmetric Levi-Civita symbol. Denoting the wave amplitudes of P or S waves by $\vec{\mathbf{u}} = a\mathbf{u}_{\mathrm{P\,or\,S}}\vec{n}_{\mathrm{P\,or\,S}}$, the final parameterization of one wavefield mode is:

$$\vec{\mathbf{u}}_m\left(t,\vec{r}\right) = a_m \mathbf{u}_m \vec{n}_m e^{-i\omega t + i\vec{k}_m\vec{r}}, \tag{6.4}$$

where *m* is the mode number comprising the propagation direction and mode type, a_m is the mode amplitude, and vector $\mathbf{u}_m$ is normalized in some way. With this notation, equations (6.3) separate for P and S waves:

$$\begin{cases} \left(\omega^2\boldsymbol{\rho} + i\omega\mathbf{d}\right)\mathbf{u}_{\mathrm{P}} = \mathbf{M}^*\vec{k}_{\mathrm{P}}^{\,2}\mathbf{u}_{\mathrm{P}}, \\ \left(\omega^2\boldsymbol{\rho} + i\omega\mathbf{d}\right)\mathbf{u}_{\mathrm{S}} = \boldsymbol{\mu}^*\vec{k}_{\mathrm{S}}^{\,2}\mathbf{u}_{\mathrm{S}}, \end{cases} \tag{6.5}$$

where $\mathbf{M}^* \equiv \boldsymbol{\Lambda}^* + 2\boldsymbol{\mu}^*$ is the complex-valued P-wave modulus matrix. Equations (6.5) represent two generalized eigenvalue problems, from which N P-wave and N S-wave modes can be found, with absolute values of wavenumbers $\left|\vec{k}_{\mathrm{P}}\right|$ and $\left|\vec{k}_{\mathrm{S}}\right|$ given by the corresponding eigenvalues (Morozov and Deng, 2016a).

By selecting $\mathbf{u}_m$ as $4N$ eigenvectors of equations (6.5) for layer l, where $m = 1, 2, \ldots 4N$ is the wavemode number, the harmonic plane-wave field can be parameterized by a $4N$-component vector. Wave mode amplitudes a (equation (6.4)) are not constrained by equations (6.5); they are combined in the total wavefield vector (Figure 6.1):

$$\boldsymbol{\psi}^l \equiv \left(\begin{array}{cccccccccccccc} a_{\mathrm{P}l}^{\downarrow 1} & a_{\mathrm{P}l}^{\uparrow 1} & a_{\mathrm{P}l}^{\downarrow 2} & a_{\mathrm{P}l}^{\uparrow 2} & a_{\mathrm{P}l}^{\downarrow 3} & a_{\mathrm{P}l}^{\uparrow 3} & \ldots & a_{\mathrm{S}l}^{\downarrow 1} & a_{\mathrm{S}l}^{\uparrow 1} & a_{\mathrm{S}l}^{\downarrow 2} & a_{\mathrm{S}l}^{\uparrow 2} & a_{\mathrm{S}l}^{\downarrow 3} & a_{\mathrm{S}l}^{\uparrow 3} & \ldots \end{array} \right)^T, \tag{6.6}$$

where superscripts ‘1’ stand for the “primary” modes with nonzero wavenumbers and ‘2’, ‘3’, etc. for “internal-deformation” modes, such as slow waves in poroelastic media or zero-wavenumber modes in VE linear-solid models (next section), among which the superscripts ‘↑’ and ‘↓’ denote the upgoing and downgoing waves, respectively. Thus, at a given frequency ω, there exist $4N$ wave modes within each layer. Note that the VE model only considers the four primary modes and forces $a_{\mathrm{P,S}\,l}^{\downarrow\uparrow J} = 0$ for all $J > 1$ (Morozov and Deng, 2018b).

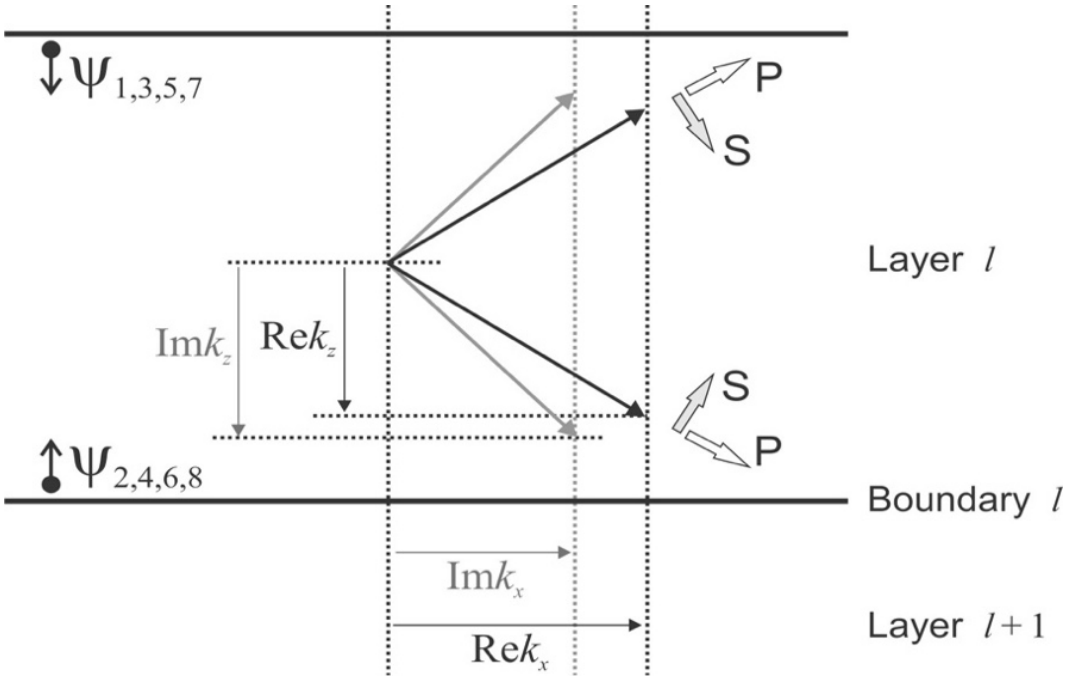

Figure 6.1. Model notation for one layer l and boundary l. Black dots labeled ψ indicate the points at which the downgoing and upgoing wave modes are parameterized, and their respective mode numbers (equation (6.6)). Black and gray arrows are the real and imaginary parts of the wavenumber bivectors for upgoing and downgoing waves of various types. Labeled block arrows indicate positive directions of particle displacements for P and S waves.

The wavefield vector $\boldsymbol{\psi}^l$ (equation (6.6)) is defined at reference points located at $x = 0$ near the upper boundary of the layer for downgoing waves and lower boundary for upgoing ones (Figure 6.1). The values of the observable and internal displacements, strains, and stresses at point $\vec{r}$ are given by

$$\begin{pmatrix} \mathbf{u}_z \\ \mathbf{u}_x \end{pmatrix}\left(\vec{r}\right) = \sum_{m=1}^{4N} \mathbf{U}^l_m\left(\vec{r}\right)\boldsymbol{\psi}^l_m \,, \tag{6.7a}$$

$$\begin{pmatrix} \boldsymbol{\varepsilon}_{zz} \\ \boldsymbol{\varepsilon}_{xx} \\ \boldsymbol{\varepsilon}_{zx} \end{pmatrix}(\vec{r}) = \sum_{m=1}^{4N} \mathbf{E}_m^l(\vec{r})\psi_m^l , \tag{6.7b}$$

$$\begin{pmatrix} \boldsymbol{\sigma}_{zz} \\ \boldsymbol{\sigma}_{xx} \\ \boldsymbol{\sigma}_{zx} \end{pmatrix}(\vec{r}) = \sum_{m=1}^{4N} \boldsymbol{\Sigma}_m^l(\vec{r})\psi_m^l , \tag{6.7c}$$

where the time-dependent factors $e^{-i\omega t}$ are implied, vector $\vec{k}$ (upward or downward, P- or S-wave) is determined by subscript m, and $\mathbf{U}_m^l$ are spatially-variant, $2N$-component vectors comprising all model-space and spatial components of displacements for mode m. I refer to such vectors as "model-spatial" vectors. Quantities $\mathbf{E}_m^l$ and $\boldsymbol{\Sigma}_m^l$ are similar $3N$ model-spatial vectors of strains and stresses for wavemode m.

The specific forms of eigenmodes $\vec{\mathbf{u}}$ and matrices $\mathbf{U}_m^l$, $\mathbf{E}_m^l$, and $\boldsymbol{\Sigma}_m^l$ are given in Appendix B. Note that in the general case $\mathbf{d} \neq \mathbf{0}$ (i.e., general WIID in equation (6.1)), the exponential wavemodes (equations (6.4)) are sufficient, but in the special case $\mathbf{d} = \mathbf{0}$ (pure VE), the secondary wavemodes need to be selected differently. With $\mathbf{d} = \mathbf{0}$ and $\boldsymbol{\rho}$ containing only one nonzero element in the SLS rheology (equation (6.10)), the secondary wavemodes for both pairs of secondary P and S waves (equations (6.5)) have zero wavenumbers $\left|\vec{k}\right| = 0$ and infinite phase velocities. To separate such degenerate wavemodes, I use equation (6.4) only for primary modes with $\left|\vec{k}\right| \neq 0$, and for secondary modes, use linear functions of z (Appendix B). Note that the case $\mathbf{d} = \mathbf{0}$ is only considered in this Chapter for generality, and for comparison with conventional models (e.g., Ursin and Stovas, 2002, and the following subsection). For real rock,

this case appears to be physically unrealistic, and nonzero **d** should normally be used. For example, for fluid-saturated sedimentary rock (such as considered in section 6.5), the ratio of the body-force (Darcy) frictional and inertial forces is large at seismic frequencies: $\left\|-\mathbf{d}\dot{\mathbf{u}}_i\right\| / \left\|\boldsymbol{\rho}\ddot{\mathbf{u}}_i\right\| \sim \eta/(\kappa\rho\omega) \sim 10^4 \div 10^6$. Consequently, forces $-\mathbf{d}\dot{\mathbf{u}}_i$ should dominate over $\boldsymbol{\rho}\ddot{\mathbf{u}}_i$, and material property **d** (although little known) should not be neglected.

6.4 Layered Standard Linear Solid

The subsequent modeling of reflection and transmission responses of a stack of SLS layers follows the well-known propagator approaches for 1-D layered media (e.g., Fuchs and Muller, 1971; Ursin and Stovas, 2002). The following subsections describe: 1) specification of the mechanical properties of the layers, 2) derivation of a complete set of wave modes within each layer (subsection 6.4.1), 3) forming the upward and downward propagator matrices (subsection 6.4.2); and 4) evaluating the variable boundary conditions in the propagator (subsection 6.4.3). Unlike, for example, Ursin and Stovas (2002), I derive no explicit expressions and small-contrast approximations but focus on simple matrix relations allowing numerical modeling of the complete transmitted and reflected wavefields.

6.4.1 Material properties

With appropriate selections for the model-space dimensionality N and constitutive matrices, equations (6.1) describe the wavefields in almost all rheologies of interest in seismology. These rheologies include Biot's (1956) and multiple-porosity, multiple-permeability poroelasticity, their extensions to solid viscosity (Sahay, 2008), macroscopic models of WIFF, all mechanically-realizable viscoelastic models including "linear solids," and also models closely

approximating the attenuation and dispersion spectra measured in laboratory experiments (Morozov and Deng, 2016b; Deng and Morozov, 2016). The SLS rheology is obtained by taking $\mathbf{d} = \mathbf{0}$ and selecting the rest of the material properties as follows. First, in 1-D wave layered models, it is convenient to parameterize the elastic properties by P-wave and shear-moduli matrices (Morozov and Deng, 2016a)

$$\mathbf{M}_l = \begin{bmatrix} M_{Ul} & -\delta M_l \\ -\delta M_l & \delta M_l \end{bmatrix} \quad \text{and} \quad \boldsymbol{\mu}_l = \begin{bmatrix} \mu_{Ul} & -\delta\mu_l \\ -\delta\mu_l & \delta\mu_l \end{bmatrix}. \tag{6.8}$$

These moduli are measurable in static mechanical experiments; in particular, the modulus $M_{Ul} \equiv (\mathbf{M}_l)_{11}$ can be measured as the ratio of the observable (uniaxial) pressure of the rock (p_1) to its dilatation (Δ_1): $M_{\mathrm{ZD}l} = -p_1/\Delta_1$, while keeping the internal variable fixed: $u_2 = 0$ and $\dot{u}_2 = 0$. Because of such form of deformation, let us call this modulus the "zero- (internal) deformation," or ZD modulus. In the VE literature, this modulus is often called "unrelaxed," because constraints $u_2 = 0$ can be implemented by a sudden increase of pressure p_1. However, this allusion to time is unimportant and may sometimes be misleading. More precisely, modulus $M_{\mathrm{ZD}l}$ can be compared to the adiabatic modulus in thermoelasticity (Landau and Lifshitz, 1986). A similar elastic matrix (first equation (6.8)) occurs in Biot's poroelasticity, in which the constraint $u_2 = 0$ means the undrained (zero pore flow) conditions and therefore $K_{\mathrm{ZD}l}$ is the undrained bulk modulus. Parameter $\delta M_l \equiv \left(\mathbf{M}_l\right)_{22} \equiv M_{\mathrm{ZD}l} - M_{\mathrm{ZP}l}$ (equation (6.8)) is the difference between the moduli of these two states (sometimes called the "modulus defect"), and $M_{\mathrm{ZP}l}$ is the "zero (internal) pressure" (ZP) P-wave modulus. This modulus is called the "relaxed" modulus in the VE terminology. However, note again that the difference between $M_{\mathrm{ZD}l}$

and M_{ZPl} is unrelated to relaxation or any other time dependence of material properties but is simply caused by the matrix character of modulus $\mathbf{M}_l$ (equation (6.8)). With $M_{ZPl}=0$, equation (6.8) describes a Maxwell's solid or fluid. For the shear modulus $\boldsymbol{\mu}_l$, the interpretation of its matrix elements is similar to the above.

For both Maxwell's and SLS rheologies, each of the bulk and shear viscosity matrices contains a single material property η_K and analogously η_μ:

$$\boldsymbol{\eta}_{Ml}=\begin{bmatrix} 0 & 0 \\ 0 & \eta_{Ml} \end{bmatrix} \quad \text{and} \quad \boldsymbol{\eta}_{\mu l}=\begin{bmatrix} 0 & 0 \\ 0 & \eta_{\mu l} \end{bmatrix}. \tag{6.9}$$

These matrices mean that the friction within such material is only caused by the strain rates of the internal variable u_2. By contrast, inertial effects are only associated with the observable variable (REV displacement; Morozov and Deng, 2016a):

$$\boldsymbol{\rho}_l=\begin{bmatrix} \rho_l & 0 \\ 0 & 0 \end{bmatrix}, \tag{6.10}$$

where ρ_l is the mass density of the rock within layer l.

In practical seismic studies, the elastic and anelastic properties are commonly reported as the phase-velocity $V(f)$ and attenuation $Q^{-1}(f)$ spectra for waves. Therefore, for each layer l, it is convenient to parameterize K_{ZDl}, δK_l, and η_K by parameters of such observable spectra. As such parameters, I can take the low- or high-frequency P-wave phase velocity V_{Pl}, the frequency of relaxation peak ω_{0l}, and the peak attenuation $Q_l^{-1}\equiv Q^{-1}\left(\omega_{0l}\right)$ for bulk deformation.

In this chapter, I consider a structure approximating permeable fluid-saturated layers with drained/undrained transitions (DUT). This approximation can be achieved by one of the following approaches, or their combination: 1) by directly utilizing the Darcy friction given by material property $\mathbf{d}$ and setting $\boldsymbol{\eta} = \mathbf{0}$, or 2) by taking $\mathbf{d} = \mathbf{0}$ and selecting an $\boldsymbol{\eta}$ predicting the same characteristic frequency $f_{\mathrm{D/U}}$ of the resulting SLS. For P-wave (axial) and shear deformations, this frequency is (Pimienta et al., 2015a, 2015b, 2016)

$$f_{\mathrm{D/U}}^{P} = \frac{4\gamma M}{H^2} \quad \text{and} \quad f_{\mathrm{D/U}}^{S} = \frac{4\gamma\mu}{H^2}, \tag{6.11}$$

where $\gamma = \kappa/\eta$ is the pore-fluid mobility, η is its viscosity, κ is the permeability of rock frame. M is the drained bulk modulus, μ is the shear modulus, and H is the thickness of the layer. This characteristic frequency means that when the observation frequency f is below, for example, $f_{\mathrm{D/U}}^{P}$, the skin depth for the diffusive P wave exceeds the thickness of the layer: $\delta_P = 2\sqrt{\gamma M / f} > H$. Under such conditions, the layer is conducive to secondary-mode deformation (such as fluid flow) across its whole thickness. Consequently, the WIID/WIFF effect should be principally controlled by the *permeabilities* of the layer *and its boundaries*, and not by its VE moduli. The condition $f \lesssim f_{\mathrm{D/U}}^{P}$ is achieved in many laboratory experiments and layering in the field (Pimienta et al., 2015a, 2015b; Morozov and Deng, 2018a; and section 6.5 in this Chapter).

Note that the empirical parameters Q_l^{-1} and ω_{0l} possess somewhat subtle and controversial physical meanings. Attributing these parameters to the material assumes that an attenuation peak of magnitude Q_l^{-1} would be observed for a "bulk wave" in a uniform

unbounded medium filled with the material of layer l (Morozov and Baharvand Ahmadi, 2015). However, measurement of these Q_l^{-1} and ω_{0l} would require a different and unrealizable experiment. Since I expect that the relaxation frequency ω_{0l} is likely caused by the DUT mechanism, this relaxation is due to a small layer thickness and *should not* be observed in an unbounded medium. In addition, isolation of bulk-deformation properties ω_{0l} and Q_l^{-1} requires nontrivial corrections of experimental data for effects of shear and shape of the laboratory sample (Morozov and Deng, 2018a). However, for simplicity, and also in keeping with conventional interpretations (e.g., Pimienta et al., 2015a, 2015b), I do not consider these intricate subjects and only explore the effects of SLS rheology in this dissertation.

As mentioned in section 6.2, despite its notation, parameter Q_l^{-1} represents not "attenuation" but the purely elastic structure of the layer. From SLS relations, (e.g., Chapter 2 in Carcione, 2007), for P-wave deformation, this quantity equals

$$Q_{Ml}^{-1} = \frac{\beta_l}{2\sqrt{1+\beta_l}}, \tag{6.12}$$

where $\beta_l \equiv \delta M_l / M_{\mathrm{ZP}l} = M_{\mathrm{ZD}l} / M_{\mathrm{ZP}l} - 1$, and similarly for shear. In contrast to Q_l^{-1}, the characteristic frequency ω_{0l} characterizes the actual internal mechanical friction and is sensitive to viscosity η within the SLS ("dashpot" element in the usual mechanical diagrams):

$$\omega_{0\,Ml} = 2Q_{Ml}^{-1}\frac{M_{\mathrm{ZD}l}}{\eta_{Ml}}, \quad \text{and} \quad \omega_{0\,\mu l} = 2Q_{\mu l}^{-1}\frac{\mu_{\mathrm{ZD}l}}{\eta_{\mu l}}. \tag{6.13}$$

By taking the layer densities ρ_l, wave velocities V_{Pl}, and V_{Sl}, and parameters ω_{0l} and Q_l^{-1} from rock-physics and seismic observations, the elastic moduli in the SLSs can be obtained as $M_{ZDl} = \rho_l V_{Pl}^2$ and $\mu_{ZDl} = \rho_l V_{Sl}^2$, and the remaining mechanical parameters obtained as $\beta_l = 2\left(Q_l^{-1}\sqrt{1+Q_l^{-2}} + Q_l^{-2}\right) \approx 2Q_l^{-1}$ (from relation (6.12)), $\delta M_l = M_{Ul}\beta_l / \left(1+\beta_l\right)$ and $\eta_{Ml} = 2Q_{Ml}^{-1} M_{Ul} / \omega_{0\,Ml}$ (relation (6.13)), and similarly for shear moduli.

6.4.2 Reflection and transmission responses

In order to evaluate the reflection and transmission responses of a layered medium, I use an approach analogous to the propagator, T-matrix, and reflection/transmission (R/T) methods (Aki and Richards, 2002; Ursin and Stovas, 2002). In contrast to VE-based models in which the dimensions of R/T matrices are 2×2 (related to the amplitudes of primary P and S waves only), these matrices are $2N \times 2N$ and account for all secondary waves. The matrices contain all reflection and transmission coefficients, mode conversions between P and S, primary and secondary waves, and all effects of attenuation. At normal incidence, this approach was given by Morozov and Deng (2016a) and applied to effective poroelastic media by Morozov and Deng (2016b).

For a group of layers numbered from l to n, the upward propagator matrix $\mathbf{T}_{l,n}$ and its inverse (downward) $\mathbf{T}_{l,n}^{-1}$ are defined as linear operators transforming the combined wavefields below the n^{th} layer into those within layer l and vice versa:

$$\boldsymbol{\psi}^l = \mathbf{T}_{l,n}\boldsymbol{\psi}^{n+1} \quad \text{and} \quad \boldsymbol{\psi}^{n+1} = \mathbf{T}_{l,n}^{-1}\boldsymbol{\psi}^l . \tag{6.14}$$

The dimensionalities of matrices $\mathbf{T}_{l,n}$ and $\mathbf{T}_{l,n}^{-1}$ are $4N\times4N$, which equals 8×8 in the present case of SLS layers. Note that in the VE case, additional constraints on the internal variables are imposed within the layers but not included in boundary conditions (next subsection), and consequently, these matrices may not represent simple matrix inverses of each other. For brevity, these matrices are denoted for one boundary by $\mathbf{T}_l \equiv \mathbf{T}_{l,l}$ and $\mathbf{T}_l^{-1} \equiv \mathbf{T}_{l,l}^{-1}$. In the following subsection, these matrices are derived from boundary conditions on the l^{th} boundary. The full propagator matrices are therefore obtained by recursive relations

$$\mathbf{T}_{l,n} = \mathbf{T}_{l,n-1}\mathbf{T}_n \quad \text{and} \quad \mathbf{T}_{l,n}^{-1} = \mathbf{T}_n^{-1}\mathbf{T}_{l,n-1}^{-1}. \tag{6.15}$$

To obtain the R/T responses for a stack of layers, let us consider the uppermost layer 1 as elastic, take n equal the number of layers, and assume an elastic half-space below the layered zone, which I count as layer n+1. Within this elastic half-space, there should be no upgoing waves, and all internal variables can be set equal zero. We can then consider an experiment with wavemode amplitudes combined in vectors $\boldsymbol{\psi}^1$ (for layer 1) and $\boldsymbol{\psi}^{n+1}$ (for layer $n+1$). If we extract from these vectors 2-component vectors $\boldsymbol{\psi}_{\downarrow}^1$, $\boldsymbol{\psi}_{\uparrow}^1$, $\boldsymbol{\psi}_{\downarrow}^{n+1}$, and $\boldsymbol{\psi}_{\uparrow}^{n+1}$ containing only the downgoing and upgoing primary P- and S-wave amplitudes, and also extract the corresponding rows and columns from matrix $\mathbf{T}_{1,n}$, equation (6.14) with $l = 1$ will take the form

$$\begin{pmatrix} \boldsymbol{\psi}_{\downarrow}^1 \\ \boldsymbol{\psi}_{\uparrow}^1 \end{pmatrix} = \begin{bmatrix} \mathbf{T}_{1,n}^{\downarrow\downarrow} & \mathbf{T}_{1,n}^{\downarrow\uparrow} \\ \mathbf{T}_{1,n}^{\uparrow\downarrow} & \mathbf{T}_{1,n}^{\uparrow\downarrow} \end{bmatrix} \begin{pmatrix} \boldsymbol{\psi}_{\downarrow}^{n+1} \\ \boldsymbol{\psi}_{\uparrow}^{n+1} \end{pmatrix}. \tag{6.16}$$

Considering incident P- and S-wave modes with unit amplitudes ($\boldsymbol{\psi}_{\downarrow}^{1} = \mathbf{I}_2$, where $\mathbf{I}_2$ is the 2×2 identity matrix) and zero incident amplitudes at the bottom of the model (2×2 matrix $\boldsymbol{\psi}_{\uparrow}^{n+1} = \mathbf{0}_2$), equations (6.16) become

$$\begin{bmatrix} \mathbf{I}_2 \\ \bar{\mathbf{R}}_{\uparrow\downarrow} \end{bmatrix} = \begin{bmatrix} \mathbf{T}_{1,n}^{\downarrow\downarrow} & \mathbf{T}_{1,n}^{\downarrow\uparrow} \\ \mathbf{T}_{1,n}^{\uparrow\downarrow} & \mathbf{T}_{1,n}^{\uparrow\uparrow} \end{bmatrix} \begin{bmatrix} \bar{\mathbf{T}}_{\downarrow} \\ \mathbf{0}_2 \end{bmatrix}, \tag{6.17}$$

where the 2×2 matrices $\bar{\mathbf{R}}_{\uparrow\downarrow}$ denotes the upward reflection and $\bar{\mathbf{T}}_{\downarrow}$ the downward transmission responses of the stack of layers. From equation (6.17), I obtain $\bar{\mathbf{T}}_{\downarrow} = \left(\mathbf{T}_{1,n}^{\downarrow\downarrow}\right)^{-1}$ and finally $\bar{\mathbf{R}}_{\uparrow\downarrow} = \mathbf{T}_{1,n}^{\uparrow\downarrow}\bar{\mathbf{T}}_{\downarrow}$.

To calculate the wavefield within any layer caused by an arbitrary incident (downgoing) field $\boldsymbol{\psi}_{\downarrow}^{1}$, I first determine the upgoing field in layer 1 as $\boldsymbol{\psi}_{\uparrow}^{1} = \bar{\mathbf{R}}_{\uparrow\downarrow}\boldsymbol{\psi}_{\downarrow}^{1}$. Further, I define a matrix operation $\mathbf{C} = \mathbf{A} \oplus \mathbf{B}$ applicable to the elastic (uppermost and lowermost) layers and constructing matrix **C** with rows 1 and $2N + 1$ (downgoing P- and S waves) taken from matrix **A** and rows 2 and $2N + 2$ (upgoing waves) from matrix **B**. By using this operation, the full $4N$-component two-way wavefield within layer 1 equals $\boldsymbol{\psi}^{1} = \left(\mathbf{I}_2 \oplus \bar{\mathbf{R}}_{\uparrow\downarrow}\right)\boldsymbol{\psi}_{\downarrow}^{1}$, and equation (6.14) gives all wavemode amplitudes below boundary l:

$$\boldsymbol{\psi}^{l+1} = \mathbf{T}_{1,l}^{-1}\left(\mathbf{I}_2 \oplus \bar{\mathbf{R}}_{\uparrow\downarrow}\right)\boldsymbol{\psi}_{\downarrow}^{1}. \tag{6.18}$$

6.4.3 Boundary conditions

To evaluate the forward and inverse propagators (equation (6.15)), matrix $\mathbf{T}_l$ needs to be determined for each boundary l (Figure 6.1). All types of linear boundary conditions (BC) involving two layers interacting at this boundary can be written as

$$\mathbf{B}_l^{\text{bottom}}\boldsymbol{\psi}^l = \mathbf{B}_{l+1}^{\text{top}}\boldsymbol{\psi}^{l+1}. \tag{6.19}$$

where $\mathbf{B}_l^{\text{bottom}}$ and $\mathbf{B}_{l+1}^{\text{top}}$ are $2N\times 2N$ matrices representing contributions of layers l and $l+1$, respectively. Additional constraints required in some cases (such as the open, closed and VE ones) are represented by relations for individual layers:

$$\mathbf{C}_l\boldsymbol{\psi}^l = \mathbf{0}. \tag{6.20}$$

The linear-equation matrices $\mathbf{B}_l^{\text{bottom}}$, $\mathbf{B}_{l+1}^{\text{top}}$, and $\mathbf{C}_l$ can be determined in two ways. First, in the most general case, if mechanical laws (given by some Lagrangian L_l and dissipation function D_l) are known for the boundary, these matrices can be obtained by adding L_l and D_l to equations (6.1) and solving for $\boldsymbol{\psi}^l$ or $\boldsymbol{\psi}^{l+1}$ while treating the field on the other side of the boundary as given (Appendix B). For example, a partially permeable boundary l can be described by an additional term $D_l = \dot{\mathbf{u}}_n^T\mathbf{d}_l\dot{\mathbf{u}}_n/2$ in the second equation (6.1), where $\dot{\mathbf{u}}_n$ is the component of macroscopic velocity orthogonal to the boundary, and $\mathbf{d}_l$ is an additional material property representing the inverse fluid mobility across the boundary. This boundary model would explain the physical meaning of the "experimentally undrained" BC by Pimienta et al. (2015a, 2016).

Although the above rigorous method using functions L_l and D_l is certainly preferable, it requires considering the physics of boundary effects, which is currently either poorly known or extremely complex because of the small-scale geologic heterogeneity. As a simple alternative to this method, in the following, I only consider mathematical BC equations often used in wave mechanics. For example, Pimienta et al. (2016) used such equations for modeling their "experimentally-undrained" boundary conditions. In these BCs, each equation in the linear system (6.19) represents some fixed combination of the components i of displacement and/or traction vectors within the layers l and l+1, evaluated at the same point $\vec{r}$ at the boundary: $\overline{a}u^{\text{bottom}}_{l,Ji} + \overline{b}\tau^{\text{bottom}}_{l,Ji} = \underline{a}u^{\text{top}}_{l+1,Ji} + \underline{b}\tau^{\text{top}}_{l+1,Ji}$, where $\underline{a}$, $\underline{b}$, $\overline{a}$, and $\overline{b}$ are some fixed weights selected for the displacement/traction combinations below and above the boundary. To represent such an equation, one row of each of matrices $\mathbf{B}^{\text{bottom}}_{l}$ and $\mathbf{B}^{\text{top}}_{l+1}$ should contain similar combinations of the displacement and traction matrices given in Appendix B. By selecting $J = 1$, $i = x$ or z, $\underline{a} = \overline{a} = 1$, and $\underline{b} = \overline{b} = 0$, two equations of continuity for the observable displacements are obtained. The corresponding two rows of matrices $\mathbf{B}^{\text{bottom}}_{l}$ and $\mathbf{B}^{\text{top}}_{l+1}$ equal (equation (6.7a) and Appendix B)

$$\left(\mathbf{B}^{\text{bottom}}_{l}\right)_{|m} = \left(\mathbf{U}^{l}_{m}\left(z_l, 0\right)\right)_{J=1,\ i=x,z}, \quad \left(\mathbf{B}^{\text{top}}_{l+1}\right)_{|m} = \left(\mathbf{U}^{l+1}_{m}\left(z_l, 0\right)\right)_{J=1,\ i=x,z} \tag{6.21a}$$

for $m = 1, 2, \ldots 4N$, where notation $\mathbf{A}_{|m}$ means the m^{th} column of matrix $\mathbf{A}$, and notation $\mathbf{b}_{J=p,\ i=x,z}$ for a model-spatial vector $\mathbf{b}$ means its p^{th} model-space component corresponding to the spatial components x and z. Similarly, the second pair of equations (6.19) represents the continuity of observable traction and is given by (Appendix B)

$$\left(\mathbf{B}_{l}^{\text{bottom}}\right)_{|m} = \left(\Theta_{m}^{l}\left(z_{l},0\right)\right)_{J=1,\ i=x,z}, \quad \left(\mathbf{B}_{l+1}^{\text{top}}\right)_{|m} = \left(\Theta_{m}^{l}\left(z_{l},0\right)\right)_{J=1,\ i=x,z}. \tag{6.21b}$$

At this point, it is convenient to focus on the specific case of $N = 2$ for SLS rheologies of the layers. Equations (6.21) for the observable deformations give only four out of eight ($4N$) BCs required in order to relate $\boldsymbol{\psi}^{l+1}$ to $\boldsymbol{\psi}^{l}$, and consequently constraints on the internal variables ($J = 2$) are also required. In VE calculations (e.g., Fuchs and Muller, 1971; Ursin and Stovas, 2002), such constraints are not stated explicitly but implied by assuming that the amplitudes of non-VE (zero-wavenumber) wavemodes equal zero. This constraint can be implemented by selecting matrix $\mathbf{C}_l$ equal

$$\left(\mathbf{C}_{l}\right)_{ij} = \delta_{kj}, \tag{6.22}$$

where δ_{kj} is the Kronecker delta, $j = 1,\ldots,8$, and $k = 3$, 4, 7, and 8 for equation numbers $i = 1$, 2, 3, and 4, respectively.

Although the VE constraints (equations (6.22)) greatly simplify the wavefield, they are artificial and impossible to implement by mechanical laws operating at the boundaries. Considering only physically-implementable BCs between different rock types (and hence allowing different natures of internal variables), it appears that the simplest BCs would be analogs of the open- and closed-pore conditions for pore fluid. A closed-boundary (Dirichlet) condition would mean that the SLS internal variable equals zero on both boundaries of layer l, which can be implemented by a four-row matrix $\mathbf{C}_l$:

$$\left(\mathbf{C}_l\right)_{|m} = \begin{pmatrix} \left(\mathbf{U}_m^l\left(z_{l-1},0\right)\right)_{J=2,\ i=x,z} \\ \left(\mathbf{U}_m^l\left(z_l,0\right)\right)_{J=2,\ i=x,z} \end{pmatrix}. \tag{6.23}$$

Alternately, an open-boundary (von Neumann) condition would mean zero traction at the boundary, which can be represented by the following four-row matrix:

$$\left(\mathbf{C}_l\right)_{|m} = \begin{pmatrix} \left(\boldsymbol{\Theta}_m^l\left(z_{l-1},0\right)\right)_{J=2,\ i=x,z} \\ \left(\boldsymbol{\Theta}_m^l\left(z_l,0\right)\right)_{J=2,\ i=x,z} \end{pmatrix}. \tag{6.24}$$

Linear combinations of BCs (6.23) or (6.24), such as "empirically undrained" (Pimienta et al., 2015a, 2016), or continuity can similarly be applied to selected boundaries. Some of these BCs were illustrated by Morozov and Deng (2018b), and I only consider the simple end-member cases (equations (6.23) and (6.24)) here.

Because of the quasi-static (massless) character of the internal-deformation modes (subsection 6.4.1), wave modes $m = 3$ and 7 are not constrained by the "open" condition. This lack of constraint occurs because these modes affect neither the strain nor traction (equations (B.4)). These variables also do not affect any observables, which means that they represent a "gauge invariance" of the formulation (Morozov and Deng, 2018b). Similarly, in the VE case, an additional non-boundary type condition is imposed on the wavefield requiring that the secondary wave modes have zero amplitudes. These gauge and VE constraints can be imposed by adding additional equations

$$\psi_m^l = 0 \tag{6.25}$$

with $m = 3$ or 7, which is a subset of the VE condition (equation (6.22)). Note that applying the open- vs. closed-boundary condition for the SLS internal variable within the uppermost and bottom layers (which are considered elastic) reduces to changing their elastic-wave velocities, analogously to considering the drained vs. undrained cases in poroelastic rock.

With matrices $\mathbf{B}_l^{\text{bottom}}$, $\mathbf{B}_{l+1}^{\text{top}}$, and $\mathbf{C}_l$ specified, the propagator matrices $\mathbf{T}_l$ and $\mathbf{T}_l^{-1}$ (equation (6.15)) can be found from equation (6.19) as

$$\mathbf{T}_l = \left(\mathbf{B}_l^{\text{bottom}}\Big|_{\mathbf{C}_l}^{-1}\right)\mathbf{B}_{l+1}^{\text{top}}, \quad \text{and} \quad \mathbf{T}_l^{-1} = \left(\mathbf{B}_{l+1}^{\text{top}}\Big|_{\mathbf{C}_{l+1}}^{-1}\right)\mathbf{B}_l^{\text{bottom}}, \tag{6.26}$$

where notation $\mathbf{A}\big|_{\mathbf{C}}^{-1}$ stands for a pseudo-inverse of matrix $\mathbf{A}$ evaluated with an additional constraint matrix $\mathbf{C}$. Evaluations of these matrix products are described as follows.

6.5 Synthetic Waveforms

The matrix propagator in the preceding section allows modeling synthetic waveforms in practically all useful linear rheologies. For brevity, I only consider a layered structure of the general "VE" type (similar to those used by Day and Minster (1984) and Ursin and Stovas (2002)) and compare the results to those in Biot's poroelastic layering. Waves in layered poroelastic media were considered by many authors (e.g., White, 1975; Carcione, 1996; Gurevich et al., 1997; Carcione and Picotti, 2006), who showed that wave attenuation in such media mostly arises from scattering and boundary-flow effects (i.e., by WIFF).

In order to evaluate the non-VE effects in a realistic 1-D layered structure, I use P-, S-wave, and density logs in the zone of Weyburn oil reservoir (Figure 6.2). Well-log data were

blocked to about 50-cm layers within the reservoir and 1-m layers outside of it. The ZD moduli $M_{\mathrm{ZD}l}$ and $\mu_{\mathrm{ZD}l}$ for each SLS layer were determined from wave velocities and densities (Figure 6.2a). The layers outside of the reservoir zone (gray lines in Figure 6.2e) are considered elastic and described by SLS structures with $\delta K_l = \delta\mu_l = 0$ (equation (6.8)) with "VE" constraints imposed on the internal variables. The VE constraints are implemented by forcing all non-VE mode amplitudes to equal zero (equation (6.22)). With such selections, only a single elastic-wave mode (for P or S waves) is allowed within each layer outside of the reservoir, the internal displacements are zero, and the ZD and ZP moduli are equal: $K_{\mathrm{ZD}l} = K_{\mathrm{ZP}l}$ and $\mu_{\mathrm{ZD}l} = \mu_{\mathrm{ZP}l}$.

To parameterize the velocity-dispersion and attenuation properties of reservoir layers, I assume that these effects are caused by DUT effects, i.e. that the SLS attenuation peaks occur at frequencies $f_{\mathrm{D/U}}$ in equation (6.11). The significance of this mechanism for the present structure is illustrated in Figure 6.2e, showing that within the Weyburn reservoir, the condition $f < f_{\mathrm{D/U}}^{P}$ is satisfied within the more permeable Vuggy zone (yellow shading in Figure 6.2e). For Marly zone, f is somewhat larger but close to both $f_{\mathrm{D/U}}$. Therefore, DUT effects are expected to be observed within reservoir layers, and particularly within the Vuggy zone. Note that with reservoir layering thinner than 0.5-m selected in the model (Figure 6.2e), both $f_{\mathrm{D/U}}$ frequencies would be higher, and the entire reservoir would be within the DUT regime.

The velocity-dispersion values $Q^{-1}\left(f_{\mathrm{D/U}}\right)$ (equation (6.12)) corresponding to DUTs within layers are principally determined by the properties of their boundaries. These properties are unknown, and for this simulation, the values of $Q^{-1}\left(f_{\mathrm{D/U}}\right)$ were randomly selected within intervals $Q_{Ml}^{-1} \in \left[0.02, 0.06\right]$ for P waves and $Q_{\mu l}^{-1} \in \left[0.03, 0.09\right]$ for S waves (Figure 6.2d).

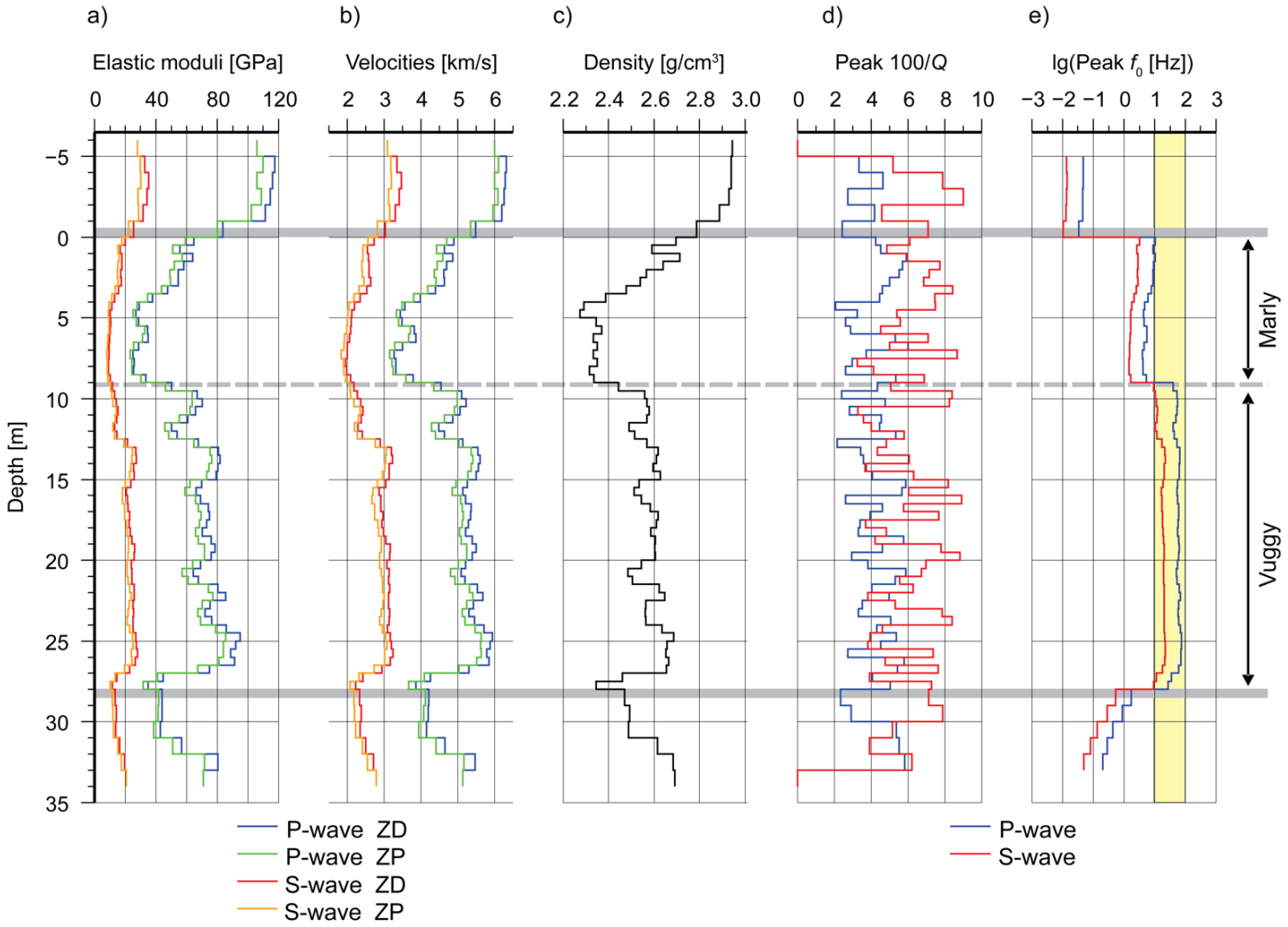

Figure 6.2. Material properties in the 1-D blocked-log model used for numerical simulations. Depths are relative to the top of the reservoir. The Marly and Vuggy zones within the reservoir are indicated by gray lines. Material-property panels show: a) ZD- and ZP-type elastic moduli for P (M) and S waves (μ) (legend), b) the corresponding P- and S-wave velocities, c) densities, d) peak values of $100/Q$, and e) characteristic drained/undrained transition frequencies for P and S waves (legend). In panel e), the seismic frequency band (10–100 Hz) is highlighted by yellow shading.

In the following, the model shown in Figure 6.2 is designated as "SLS," and I also created its "Elastic" counterpart consisting of the same structure with viscosities η_M and η_μ set equal zero (equation (6.8)). Note that within the reservoir, this elastic structure is still two-component, and consequently it possesses two (ZP and ZD) elastic moduli and is sensitive to boundary conditions between layers.

In order to investigate the VE and non-VE effects in the "SLS" and "Elastic" structures, I generated downgoing P- or S-waves of unit amplitudes above the reservoir and performed wave modeling by assuming different internal-variable boundary conditions (BC) between the layers. In the first test, VE constraints were applied to all layers (equation (6.22)). In the following, these types of wavefields are denoted "SLS-VE" and "Elastic-VE." These wavefields correspond to predictions of the conventional VE model and of its elastic equivalent. However, although "VE" conditions are easy to implement, they are still non-physical – they are applied directly to the resulting wavefield and are impossible to implement by stress-displacement constraints on the boundaries of the layers (Morozov and Deng, 2018b).

Similar to the cases "SLS-VE" and "Elastic-VE," six additional cases "Elastic-open," "Elastic-closed," "Elastic-continuity," "SLS-open," "SLS-closed," and "SLS-continuity" were generated by replacing VE constraints with the corresponding BCs for the internal SLS variables within each layer. Figures 6.3 and 6.4 show depth variations of several key observables modeled at normal incidence, for incident harmonic P or S waves at frequency 45.1 Hz, which is close to the dominant frequency in Weyburn reflection dataset. Most of these observables are close when evaluated with "VE," "open," and "continuity" BCs but strongly different when "closed" BCs are used. Once again, this contrast is expected from poroelasticity (Dunn, 1987), and similar

observations in a one-layer model were made by Morozov and Deng (2018b). Differences in the BCs produce "dispersion" of the complex-valued empirical moduli defined as

$$M_z = \frac{\sigma_{1zz}}{\varepsilon_{1zz}} \quad \text{and} \quad M_x = \frac{\sigma_{1zx}}{\varepsilon_{1zx}} \tag{6.27}$$

for incident P and S waves, respectively (Figures 6.3e and 6.4e). These variations are similar to the difference between the "Elastic" and "SLS" models and are stronger pronounced in the empirical inverse quality factors $Q_{z,x}^{-1} \equiv -\tan\left(\arg M_{z,x}\right)$ (Figures 6.3f and 6.4f). These empirical inverse Q-factors are broadly variable within and between layers from zero to about 0.12, particularly for "closed" BCs. Closer inspection shows that these Q^{-1} values can be both positive and negative), as it was also observed by Morozov and Deng (2018b).

Note that although similar random peak-Q^{-1} values were used within the entire models (Figure 6.2d), the resulting phase-lag Q^{-1} for the VE, "open," and "continuity" BCs are mostly concentrated within the Vuggy zone (Figures 6.3f and 6.4f), where they are of the same level as the peak Q^{-1} (Figure 6.2d). The deformations of the internal variables (note again their analogy to pore-fluid flows) are also significantly lower within the Marly zone (Figures 6.3a, c and 6.4a, c). These differences are caused by low permeability within the Marley zone, which causes higher DUT frequencies (Figure 6.2e).

Even in the absence of internal viscosity, the "Elastic" model is two-component and therefore behaves similarly to SLS layering (Figure 6.5; compare to Figure 6.3). The two notable differences are: 1) stronger variation of the empirical modulus due to changing BCs (Figure 6.5e), and 2) much lower phase-lag Q^{-1} for "closed" BC (Figure 6.5f). Note that for "closed"

BCs, the phase-lag Q^{-1} still does not equal automatically zero, varies between negative and positive values within layers, and jumps across layer boundaries (Figure 6.5f).

Finally, recall that the SLS rheologies of the layers in the model of this Chapter were constructed to implement the DUT attenuation mechanism, in which the fluid flow at low frequencies penetrates the entire layer (section 6.4; Pimienta et al., 2015a, 2015b, 2016). This mechanism is described by nonzero matrix **d** (equation (6.1)) and represents a basic case of WIFF in a poroelastic rock (White, 1975; Gurevich et al., 1997) or WIID for a more general rock. Therefore, I also tested this frictional mechanism directly, by adding the following matrix **d** to the "Elastic-continuity" model:

$$\mathbf{d} = \begin{bmatrix} 0 & 0 \\ 0 & 1/\gamma \end{bmatrix}, \tag{6.28}$$

where $\gamma = f_{\mathrm{D/U}} H^2 / (4M)$ (inverse of equation (6.11)) is the mobility corresponding to the frequency $f_{\mathrm{D/U}}$ selected for each layer.

As shown in Figure 6.6, although the layers containing matrices $\mathbf{d} \neq \mathbf{0}$ are not SLS (i.e. non-VE), the resulting modulus-dispersion effects (and therefore seismic reflectivity) are similar to those in the SLS-layered model (Figure 6.3). At the same time, the movements of internal variables within layers are significantly different for these models. Because of the secondary wave modes, the amplitudes of internal stresses range from zeros on the boundaries to large values within the layers (Figure 6.6d). Similarly, within each layer, the phase-lag Q^{-1} values vary sharply from near-zero to about 0.01 to 0.04 near its boundary (Figure 6.6f). The variations of these apparent Q^{-1}s are strongly different from those in other models (Figure 6.3f to 6.5f).

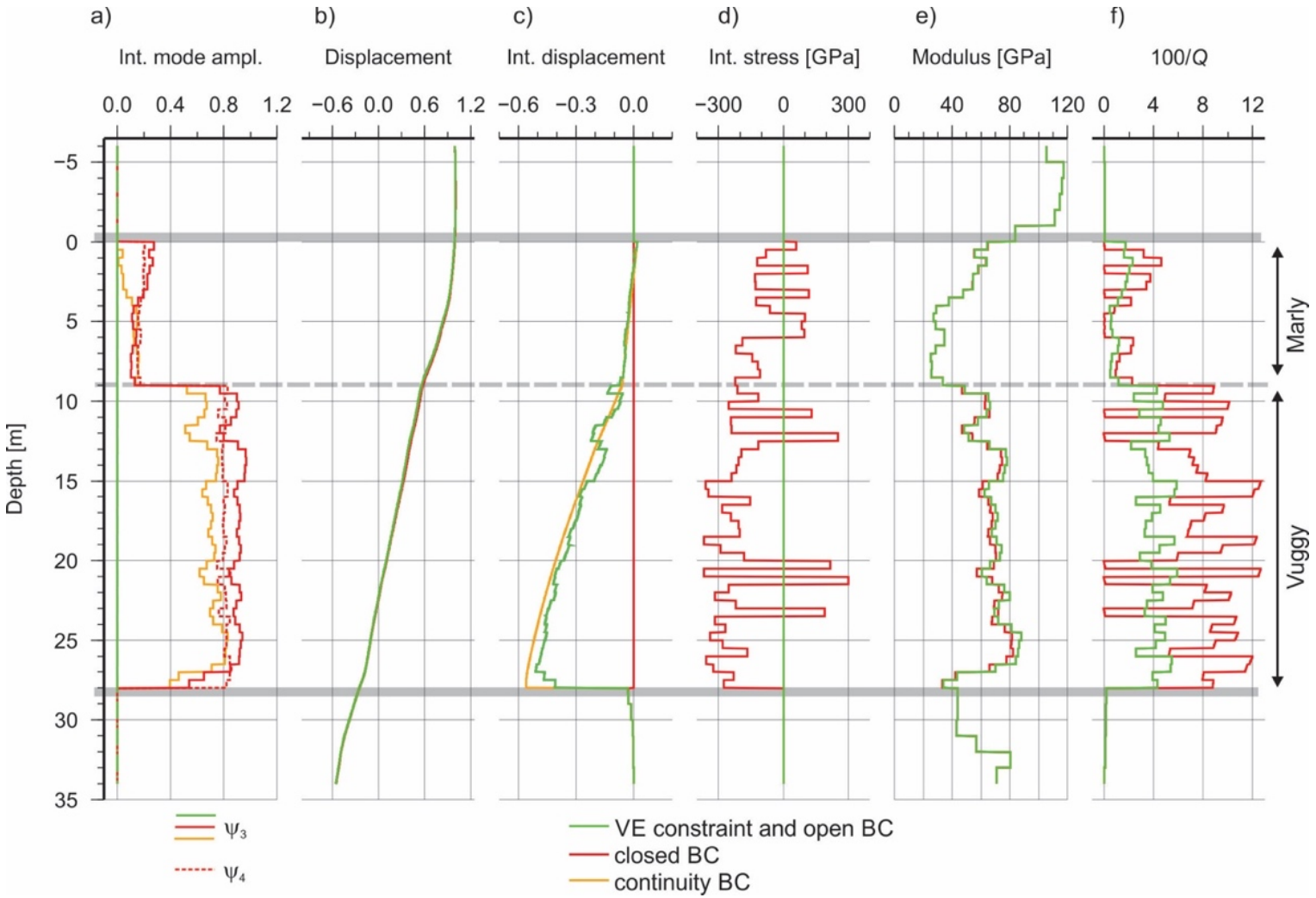

Figure 6.3. Depth dependencies of observable fields in model "SLS" for a vertically-incident P wave at frequency 45.1 Hz: a) amplitudes of internal modes, b) vertical displacement u_{1z}, c) internal vertical displacement u_{2z}, d) internal stress σ_{2zz}, e) empirical modulus $|M_z|$ (equation (6.27)), f) inverse phase-lag $100/Q_z$, where $Q_z \equiv -1/\tan[\arg M_z]$. Model types and internal boundary conditions (BC) are indicated in the legends. The curves for continuity BC often overlap with VE ones.

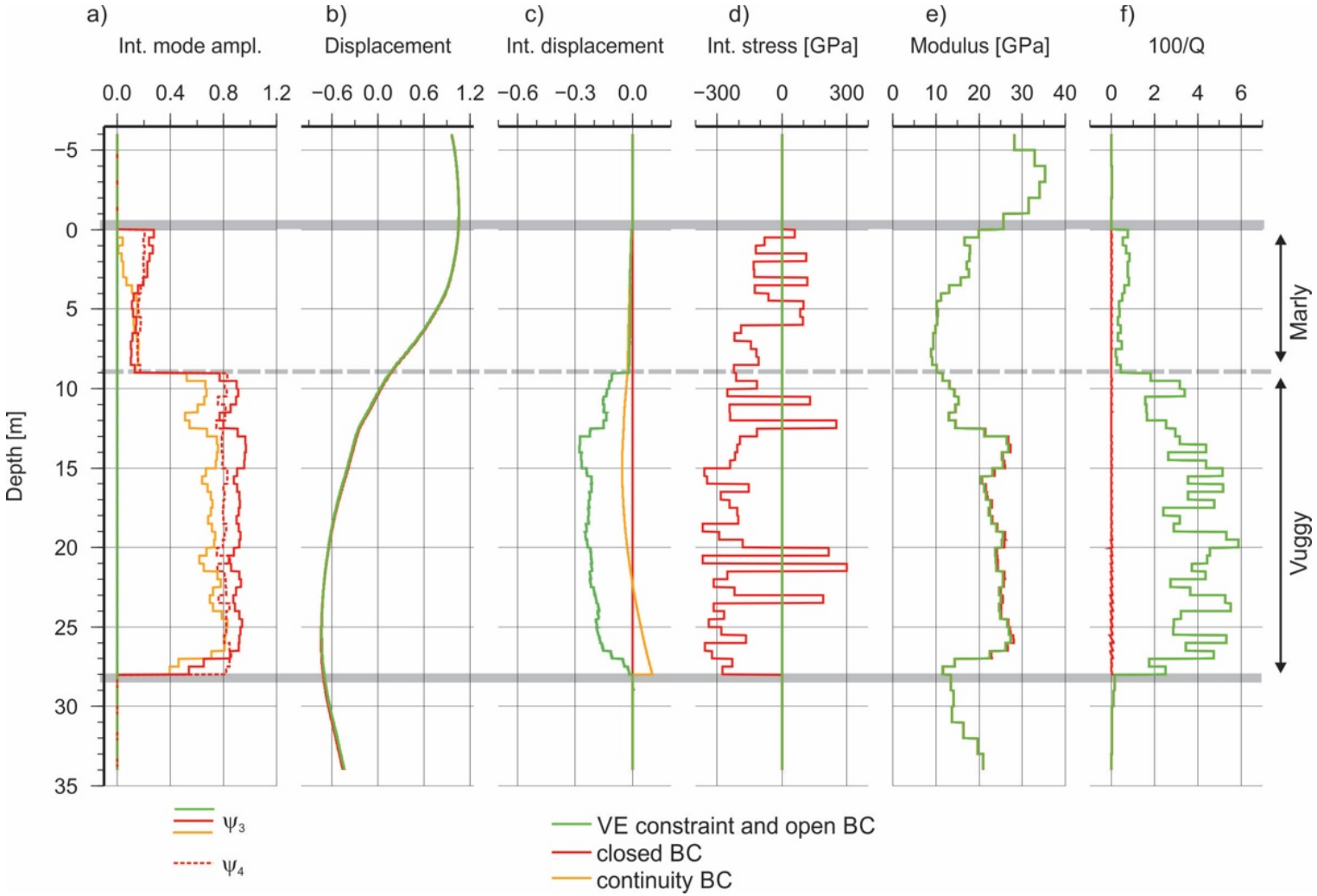

Figure 6.4. Depth dependencies of observable fields in model "SLS" for a vertically-incident S wave at frequency 45.1 Hz. Plot panels as in Figure 6.3, with horizontal-component displacements and stresses used instead of vertical ones.

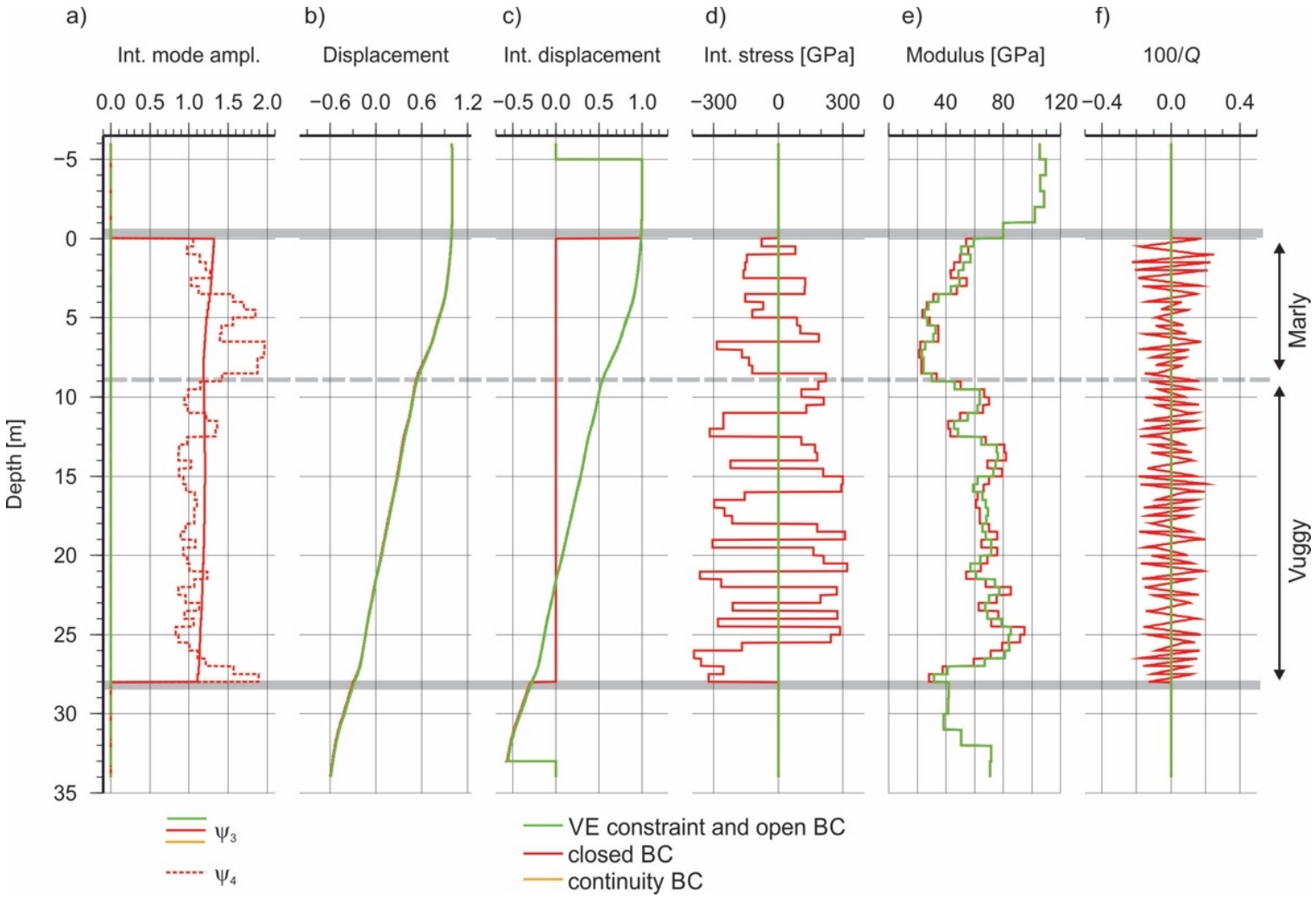

Figure 6.5. Depth dependencies of observable fields in model “Elastic” for a vertically-incident P wave at frequency 45.1 Hz, plotted as in Figure 6.3.

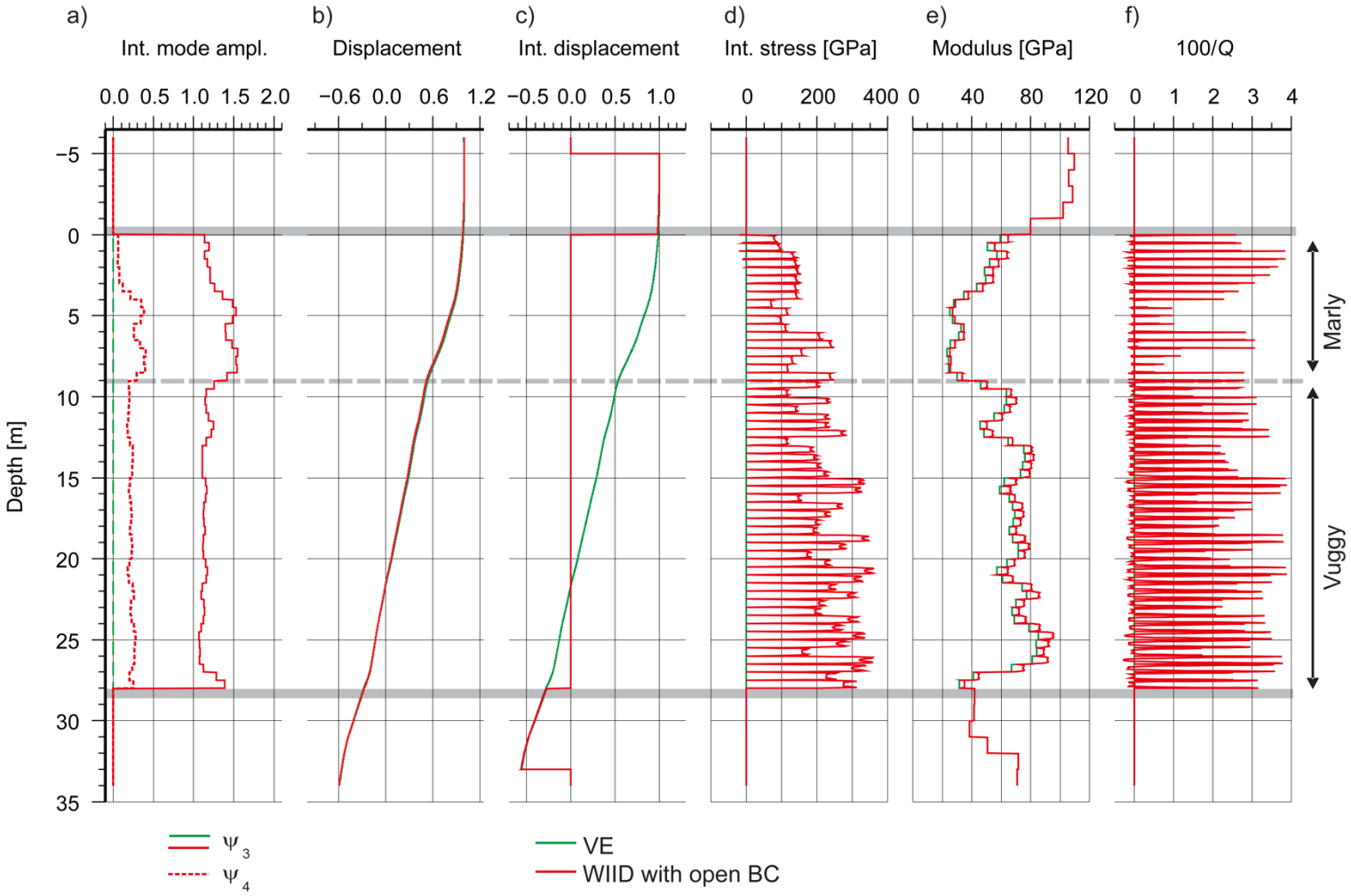

Figure 6.6. Depth dependencies of observable fields in model "Elastic-WIID" for a vertically-incident P wave at frequency 45.1 Hz, plotted as in Figures 6.3 to 6.5.

Finally, inverse Fourier transform of the harmonic modes modeled in any of the models produces the seismograms for reflected, transmitted, or mode-converted waves. For example, Figure 6.7 shows the reflection response on top of the reservoir to a band-limited P-wave pulse, evaluated for models "Elastic" and "SLS" at three ray parameters and for several types of anelastic boundary conditions. As any effects of moderate anelasticity ($Q \sim 30$) with this thin reservoir, the differences between elastic and anelastic seismograms are moderate at dominant frequency. However, the different anelastic BCs have clearly different effects on the reflected seismograms (Figure 6.7).

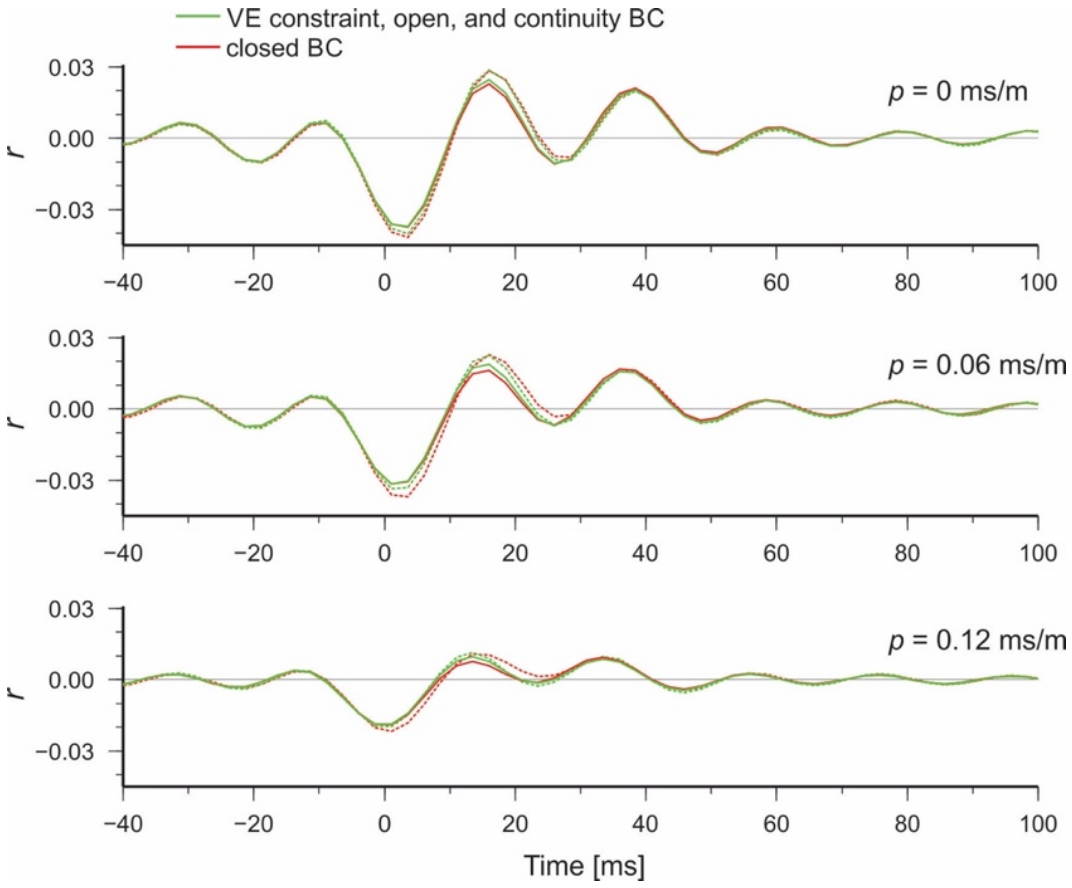

Figure 6.7. Reflected seismograms for incident P-wave pulses of amplitudes one with ray parameters p = 0, 0.06, and 0.12 ms/m (labels). Boundary-condition (BC) selections are given by line colors (legend). Dashed and solid lines show the simulations in models "Elastic" and "SLS," respectively.

6.6 *Q*-factors

Effects of anelastic structures on seismic records are usually measured and reported in terms of quality (Q) factors. However, the Q-factors measured in different observations need to be interpreted and compared carefully, because they may be specific to each measurement and not simply related to any unique property of the medium (Morozov and Baharvand Ahmadi, 2015). For this reason, I denote the measured quantities as "apparent" inverse Q-factors Q_{app}^{-1}. In this section, I illustrate several types of Q_{app}^{-1} arising from the synthetic records modeled in the layered structure of Figure 6.2.

In principle, an unambiguous "in-situ" Q_{app}^{-1} can be obtained from a hypothetical measurement of stress/strain phase lags (equation (6.27)) at every point within the subsurface (Figures 6.3f, 6.4f, 6.5f, and 6.6f). This type of Q is often used to interpret subresonant strain/stress phase lag measurements with rock samples in the laboratory (e.g., Lakes, 2009; Tisato and Quintal, 2013; Pimienta et al., 2015a, 2015b). The detailed spatial variations of this Q_{app}^{-1} also resemble the Q^{-1} patterns produced by full-waveform inversions (FWI, e.g., Prieux et al., 2013). However, quantitatively, the phase lags occurring in the model of this Chapter, in the laboratory, and in FWI are not easy to compare, because each of them depends on the detail of the respective measurement procedure (layering, BCs, wave types, incidence angles, size of the sample, experimental corrections, and FWI parameterization and regularization approaches). It is therefore hardly practical to treat these Q^{-1}s as properties of layer materials and to compare quantitatively. Note that such Q^{-1} can be nonzero (and sometimes negative) within purely elastic layering (Figure 6.5f), and therefore it can be interpreted as a specific case of the "scattering Q^{-1}" related to two-component nature of the layers and to the selected anelastic BCs between them.

In contrast to the in-situ Q^{-1} that can only be measurable hypothetically within real seismic wavefield (Figures 6.3f, 6.4f, 6.5f, and 6.6f), practical attenuation measurements use different definitions of Q^{-1} based on transmitted seismic waves, such as in ultrasonic laboratory experiments or vertical seismic profile (VSP). Before discussing these definitions in the following paragraphs, note that they always also contain two hypothetical elements:

H1) Comparisons of measurements in different wavefields, one of which is often unrealizable (such as an "elastic equivalent" for a given subsurface structure), and

H2) Some assumed theoretical relation between these wavefields (such as geometric spreading or presence/absence of small-scale heterogeneity).

Because of these inherent hypotheses, it is similarly difficult to compare the values of Q^{-1} produced by different methods.

In attenuation observations in seismic waves, the measured quantity is usually the spatial ($\alpha(f)$) or temporal ($\chi(f)$) attenuation coefficient, from which Q_{app}^{-1} is further inferred. For example, $\chi(f)$ is often measured from the ratio of time-averaged spectral-power fluxes for waves entering ($P_{\text{in}}(f)$) and leaving ($P_{\text{out}}(f)$) the attenuation zone (e.g., White, 1992):

$$\chi(f) = \gamma + \pi Q_{\text{app}}^{-1} f, \quad \text{where} \quad \chi(f) \equiv -\frac{1}{t}\ln\left[\frac{1}{G}\sqrt{\frac{P_{\text{out}}(f)}{P_{\text{in}}(f)}}\right]. \tag{6.29}$$

In these relations, G is the relative geometric spreading factor between the "in" and "out" wavefields, and t is the difference in propagation times between them. The right-hand side of the

first equation (6.29) simply represents an isolation of the limit $\gamma \equiv \lim_{f \to 0} \chi\left(f\right)$, and higher-order variations of $\chi(f)$ with f are included in a frequency-dependent $Q_{\text{app}}^{-1}\left(f\right)$. The term γ describes the frequency-independent differences of the real energy-flux ratios from those included in the geometrical-spreading model G. Morozov (2008) called this term "geometric attenuation" and showed how it arose in many attenuation measurements. In exploration-data attenuation studies, such term was used in attenuation measurements by Blias (2012) and Baharvand Ahmadi and Morozov (2013). However, in (earthquake) observational studies, this term is often omitted, which results in $Q_{\text{app}}\left(f\right)$ spuriously increasing with frequency (Morozov, 2008b).

For a layered medium, the values of γ and Q_{app}^{-1} also depend on the ray parameter. For example, at vertical incidence, frequency dependencies of $\chi(f)$ for several models are shown in Figure 6.8, evaluated by taking $P_{\text{in}}(f)$ for downgoing waves above the reservoir zone and $P_{\text{out}}(f)$ below this zone. Because transmission losses are not included in the selected form of G, a nonzero and increasing with frequency $\chi(f)$ is obtained for models "Elastic" and "SLS" (Figure 6.8). As it is intuitively expected, at any frequency, the attenuation within a reservoir consisting of "SLS" layers is greater than in an "Elastic" one. In addition to these general trends, note the oscillations in the $\chi(f)$ dependencies caused by tuning within the layered structure, particularly at frequencies near 70–80 Hz (Figure 6.8a).

The Q^{-1} measured in elastic models is usually interpreted as the scattering attenuation (e.g., Gurevich et al., 1997):

$$Q_{\text{scatt}}^{-1} = Q_{\text{app}}^{-1}\Big|_{\text{Elastic}}, \tag{6.30}$$

where the subscript in the right-hand side indicates the model in which the Q_{app}^{-1} is obtained (dashed lines in Figure 6.8). Note that this Q_{scatt}^{-1} is only a part of the total scattering attenuation $\chi_{\text{scatt}}\left(f\right)=\gamma_{\text{scatt}}+\pi Q_{\text{scatt}}^{-1}f$ (equation (6.29); Figure 6.8a). When evaluating this attenuation coefficient, I take $G=\sqrt{Z_{\text{out}}/Z_{\text{in}}}$ (where Z_{in} and Z_{out} are the impedances for the corresponding waves) and evaluate t (equation (6.29)) from ray theory. Note that these selections are subjective and represent the hypothesis H2) mentioned above. With different estimates for the "background" G, parameter γ would change, but determining accurate values of G in realistic structures can be difficult and ambiguous (Morozov, 2008b). In particular, for the model reservoir, the frequency-dependent theoretical transmission coefficient for a stack of elastic layers could be included in G, but it would remain uncertain whether the layers should be considered in their ZD or ZP states, or their combinations.

The empirical Q_{scatt}^{-1} evaluated with the selected G shows an increasing trend and significant variations with frequency (Figure 6.8b), which can be separated into a smooth dependence $\bar{Q}_{\text{scatt}}^{-1}\left(f\right)$ usually expected from scattering on small-scale heterogeneities and the remaining "fluctuation Q^{-1}" (Morozov and Baharvand Ahmadi, 2015):

$$Q_{\text{scatt}}^{-1}\left(f\right)=\bar{Q}_{\text{scatt}}^{-1}\left(f\right)+Q_{\text{fluct}}^{-1}\left(f\right). \tag{6.31}$$

In Figure 6.8b, dashed gray lines show a similar near-constant level of $\bar{Q}^{-1}\approx 0.05$ for the "SLS-closed" wavefield.

Quantities $\chi(f)$, γ, and fQ_{app}^{-1} are often small, and when multiple mechanisms of attenuation are considered, they are additive for different mechanisms. By using this additivity, for model "SLS," an "intrinsic" attenuation contribution Q_{int}^{-1} can be determined from the following relation:

$$Q_{\text{app}}^{-1}\Big|_{\text{SLS}} = Q_{\text{app}}^{-1}\Big|_{\text{Elastic-VE}} + Q_{\text{int}}^{-1}, \tag{6.32}$$

and similarly for $\chi(f)$ and γ. The corresponding values of $\chi_{\text{int}}\left(f\right)$ and $Q_{\text{int}}^{-1}\left(f\right)$ are shown in Figure 6.9. However, note that the interpretation of this quantity is also tricky, because it involves subtraction of measurements made in two structures ("SLS" and "Elastic") that never coexist in reality. In each of these structures, Q_{app}^{-1} is produced by numerous physical factors which can be hardly compared and guaranteed to be equal. In particular, it is unclear whether the same type of internal BCs should be used for both the "SLS" model (representing a real structure) and for its hypothetical "Elastic-VE" counterpart. With both internal BCs being "closed," the values of Q_{int}^{-1} are larger in the present case (Figure 6.9), but they can be lower for poroelastic rock (Dunn, 1987) and for different layering (Morozov and Deng, 2018b). Thus, the $Q_{\text{int}}^{-1}\left(f\right)$ inferred from relation (6.32) is a complex and subtle property, in contrast to its expected meaning of an intuitive measure of mechanical-energy absorption. At the same time, relatively simple general trends corresponding to $Q_{\text{int}}^{-1}\left(f\right) \approx const$ can be seen in $\chi_{\text{int}}\left(f\right)$ dependencies (gray dashed lines in Figure 6.9), with complex "fluctuation Q" variations on top of them.

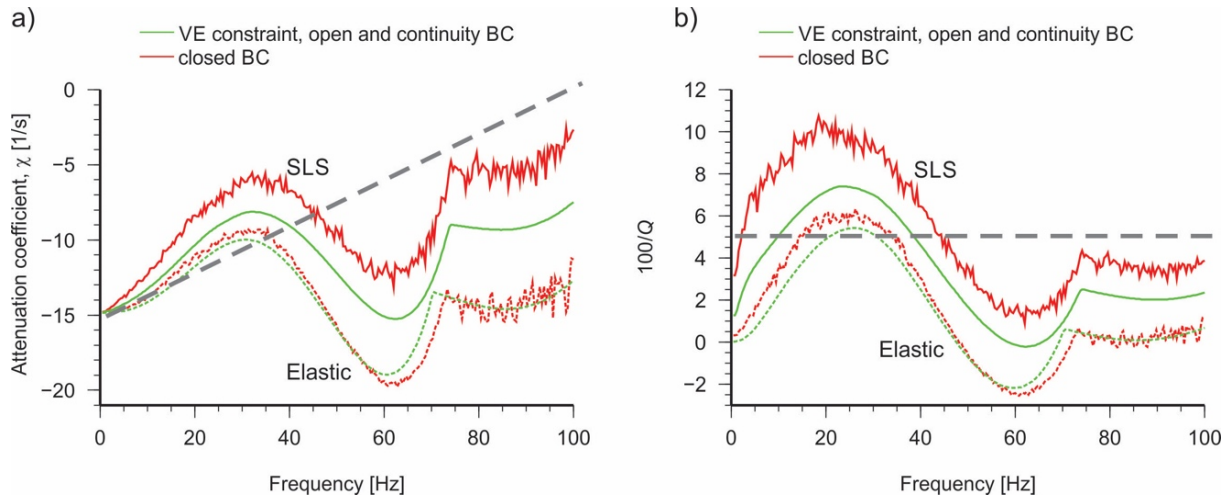

Figure 6.8. Frequency-dependent scattering attenuation Q^{-1} (equation (6.29)) derived from the spectra of P waves transmitted through the reservoir zone: a) temporal attenuation coefficient $\chi_{\text{scatt}}(f)$, b) Q_{scatt}^{-1} inferred from it by estimating the geometric attenuation term $\gamma_{\text{scatt}} = -14.82\ \text{s}^{-1}$. Solid and dashed lines represent the "SLS" and "Elastic" models, respectively. Gray dashed lines show an interpreted linear trend with constant $\bar{Q} \approx 20$ for the "SLS-closed" model.

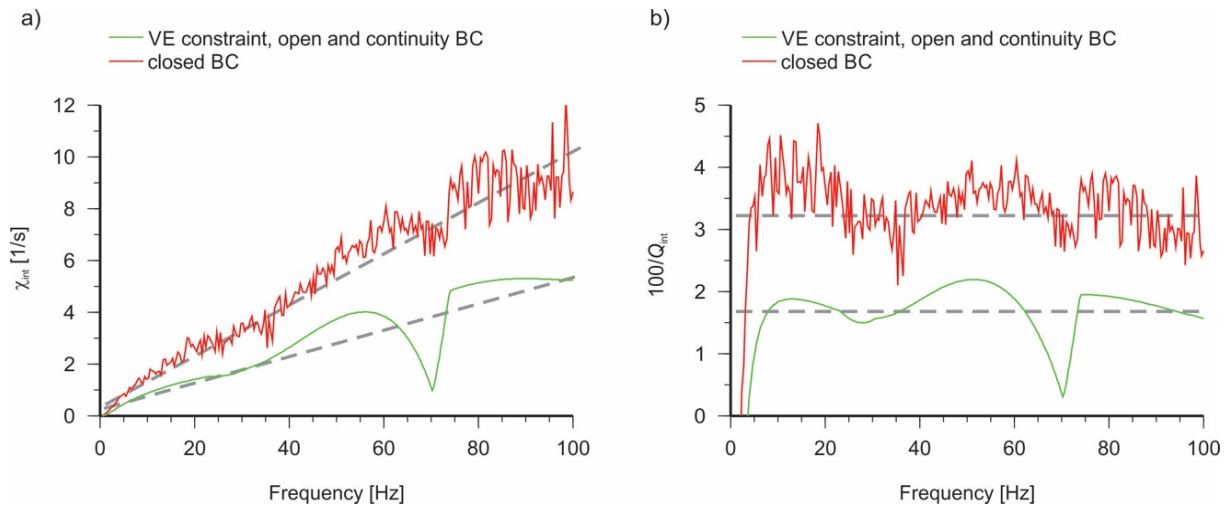

Figure 6.9. Intrinsic-attenuation measures evaluated by subtracting attenuation coefficients in models "SLS" and "Elastic" (equation (6.32)): a) attenuation coefficient χ_{int}, b) inverse Q-factor Q_{int}^{-1} obtained by taking $\gamma_{\text{int}} = 0.3\ \text{s}^{-1}$. Plot panels and legends are as in Figure 6.8. Gray dashed lines show interpreted linear trends with constant $\bar{Q}_{\text{int}}^{-1}$.

In the "WIID" example, the "intrinsic" contribution to $\chi(f)$ can be associated with the WIID effect, and equation (6.32) becomes

$$Q_{\text{app}}^{-1}\Big|_{\text{WIID}} = Q_{\text{app}}^{-1}\Big|_{\text{Elastic-continuity}} + Q_{\text{WIID}}^{-1}\,. \tag{6.33}$$

Note that when evaluating Q_{WIID}^{-1} from this equation, a different "Elastic" model needs to be used compared to equation (6.32). Quantity Q_{WIID}^{-1} and the full attenuation coefficient χ_{WIID} are shown in Figure 6.10. These quantities are analogous to WIFF attenuation effects in wet porous rock (Gurevich et al., 1997; Tisato and Quintal, 2013).

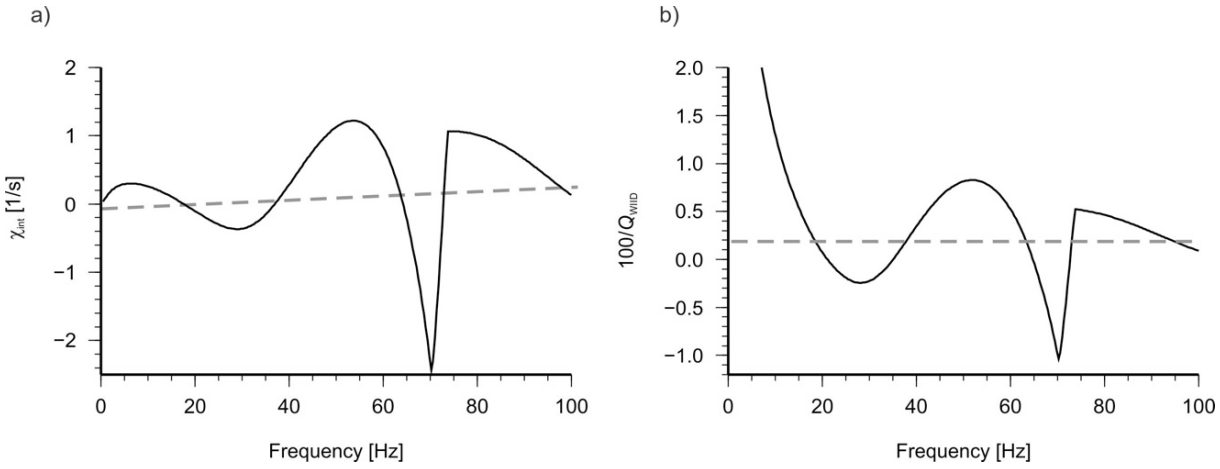

Figure 6.10. "WIID" attenuation measures evaluated by subtracting attenuation coefficients in models "Elastic-WIID" and "Elastic-open" (equation (6.33)): a) attenuation coefficient χ_{int}, b) inverse Q-factor Q_{WIID}^{-1} after taking $\gamma_{\text{int}} = -0.15\ \text{s}^{-1}$. Gray dashed lines show interpreted linear trends in $\chi_{\text{int}}(f)$ with constant $\overline{Q}_{\text{WIID}}^{-1}$.

With variable velocities, densities and combinations of ZD and ZP moduli in the model (Figure 6.2), frequency dependencies of the resulting Q^{-1} in Figure 6.2–6.10 show broad attenuation spectra similar to those of the generalized SLS (GSLS). Thus, this model suggests

that near-constant Q or broad peaks in "relaxation spectra" often assumed for explaining seismic and laboratory attenuation observations (Liu et al., 1976; Lakes, 2009) can be produced by contributions from multiple heterogeneities and/or layers traversed by the seismic wave. In this superposition, boundary conditions between the heterogeneities should be particularly important, and numerous internal variables related to small-scale heterogeneities should almost invariably produce broad attenuation spectra.

6.7 Discussion

In this section, the general significance of parameterizing seismic attenuation models by constant or frequency-dependent Q-factors is discussed. On one hand, the Q is one of the most important seismic indicators of physical properties of the medium. Reduced Q values are usually found for waves passing through zones containing hydrocarbons, fluids, pockets of partial saturation, partial melts, or zones of increased heterogeneity. However, the preceding sections also show that unfortunately, although many Q-factors can be inferred from the wavefields, none of them represents a reliable cumulative measure of medium anelasticity.

There are two general reasons for such skepticism about the Q-factor. First, there exist too many scattering and absorption effects (many more than assumed in the VE model) that can explain any given $Q(f)$ and the associated velocity-dispersion spectra. For any combination of internal boundary conditions (BC), these spectra can always be modeled (section 6.5), but they turn out to be different for different wave types and propagation directions within the same medium. The ordinary (usually well-known) and internal BCs (unknown and usually not even recognized) have major effects on the observed $Q(f)$ spectra, and it is hardly possible to infer a meaningful effective Q^{-1} of a layered rock by some kind of averaging of the Q-factors of the

layers, as it is sometimes attempted (e.g., Qadrouh et al., 2018). In order to average these effects out and produce a DEVM, the averaging REV should be large (Milani et al., 2016a), and it should be located far from any reflecting boundaries. This means that Q-factors cannot be uniquely attributed to the individual layers of a layered model (Figure 6.2) or to parts of a small sample in a laboratory experiment. A rigorous $Q(f)$ can only be defined from stress-strain measurements, but as the WIID model shows (Figure 6.6f), it can be extremely variable within layers and not scalable to the mesoscopic scale.

The second reason for doubting the Q parameterization of anelasticity is that it is tailored for only a very specific theory (VE), which modifies the equations of mechanics by introducing "material-memory" relations. A major drawback of this theory is in its focus on only deformations of a single-component, quasi-uniform medium and no other mechanical processes. This model does not consider the internal structure of the rock, ignores the effects of permeability (body-wave friction) and does not explain, for example, such basic phenomena as quasi-static flows within a reservoir layer. In low-frequency laboratory experiments, such effects are represented by the "drained-undrained transition" (DUT; Pimienta et al., 2016; Morozov and Deng, 2018a). By contrast, the model in this Chapter (equation 6.1) aims at explaining *all* mechanical experiments with a given rock (Morozov and Deng, 2016a), but it contains no material properties that could be uniquely associated with a Q.

A popular use of the Q model consists in deriving the peak values of $Q^{-1}\left(f\right)$ from the difference of the low- and high-frequency asymptotes of the velocity spectra ($\chi(f)$) (e.g., Carcione and Picotti, 2006; Chen et al., 2018; Qadrouh et al, 2018). However, note that as shown in equation 6.12, the peak Q^{-1} is actually a purely elastic property and does not mean the

existence of internal friction, i.e. absorption of mechanical energy. An observation of velocity dispersion simply indicates the existence of internal variables and multiple forms of elastic deformations. For example, the Q^{-1}_{peak} is present in the "Elastic" model as a difference between the ZD and ZP moduli (Figure 6.5e), but it differs from the phase-lag Q^{-1} (Figure 6.5f).

Another common use of the Q model consists in partitioning the observed Q^{-1} into scattering, intrinsic, WIFF (WIID), and sometimes other types of Q (e.g., Gurevich et al., 1997; Tisato and Quintal, 2013; Morozov and Baharvand Ahmadi, 2015). However, note again that all of these quantities and relations between them (e.g., equation (6.32) or (6.33) in section 6.6) are only valid for quasi-uniform media and far from any material-property contrasts. When applied to realistic layering (section 6.6) or laboratory samples (Morozov, 2015; Morozov and Deng, 2018a), these empirical relations become very case-specific and can hardly be portable to other areas.

Thus, although many forms of frequency-dependent and spatially-variable "quality-factors" are used in the attenuation research today, they should be interpreted with care. Researchers are encouraged to utilize rigorous mechanics when interpreting rock-physics and seismic experiments with heterogeneous anelastic media. Some time ago, White (1986) made similar recommendations for fluid-saturated porous rock.

6.8 Conclusions

The viscoelastic (VE) model broadly used for modeling seismic waves uses assumed and approximate equations, disregards body-force internal friction, assumes absence of non-VE deformation modes, and disregards boundary conditions in layered and heterogeneous media.

Nevertheless, similarly to the mechanics of fluid-saturated porous rocks, non-VE wave modes and frictional forces should exist. Similar to poroelasticity, Darcy-type (body-force) friction and anelastic boundary conditions between layers and meso- and macroscopic-scale heterogeneities should cause dominant effects on seismic-wave attenuation and velocity dispersion. For physically-consistent modeling of anelastic effects, first-principle equations of physics are required.

Rigorous modeling of wave propagation in a model of a layered oil reservoir was performed by first-principle macroscopic continuum mechanics without VE approximations. Transmission, reflected, and mode converted waves were modeled with several types of boundary conditions between the anelastic properties of the layers. Several types of attenuation coefficients and empirical (apparent) Q-factors were derived from modeled wavefields. These Q-factors include two forms of the elastic Q (scattering, and fluctuation), and intrinsic Q, which can be further subdivided into Q-factors associated with specific models. The often-observed near-constant Q or broad attenuation peaks can be explained by wave propagation through multiple layers with variable properties, and particularly variable Darcy-type friction and anelastic boundary conditions on material-property contrasts.

CHAPTER 7

CONCLUISONS AND RECOMMENDATIONS FOR FUTURE RESEARCH

This dissertation presented three relatively independent studies related to seismic wave propagation and reflections in the area of Weyburn oilfield. The specific principal goals of these studies were:

1) Proposing a simple and effective source-waveform estimation method for use in reflection seismic processing;

2) A new method of time-lapse (TL) acoustic-impedance (AI) analysis for Weyburn CO_2 sequestration project, including:

   a) developing a waveform-calibration approach;

   b) evaluating TL reflectivity differences;

   c) evaluating TL AI differences;

   d) analyzing TL variations of some physical properties due to CO_2 injection in Weyburn Field between 1999 and 2002;

3) Developing a new method for rigorous modeling of wave propagation in layered media by first-principle continuum mechanics without VE approximations, application of this method to Weyburn reservoir, and again making observations about the Q factors which may be significant in many other studies.

All of these goals were satisfactorily achieved in Chapters 3 to 6. In the following sections 7.1 to 7.3, I give three groups of conclusions separately for each of the above topics. All the above approaches in this dissertation are innovative, and in the case of topic 3), some of the results may even be highly controversial from the viewpoint of the current paradigm. Therefore, substantial further research is suggested by each of these topics. Some directions of such possible future research are suggested in section 7.4.

7.1 Conclusions for Source Waveform Estimation

A simple and effective source-waveform estimation method is proposed based on iterative identification of the strongest and sparse reflections in seismic records. Based on a number of tests using synthetic well-log models and real data, the main conclusions for this method are as follows:

1) The approach is stable with respect to noise and parameter variations, and it allows accurately estimating the source waveforms without well-log control and sophisticated statistical hypotheses.

2) The optimization approach allows correcting for coherent noise consisting in a possible spurious (de)amplification and time shifts of the low-frequency components of the records. For the forward model with time-shift filter considered, such coherent-noise effects are reduced by optimizing the resulting source waveform in terms of its practically-important properties. However, the results of this optimization cannot be viewed as inversion for parameters of such (de)amplification.

3) If the Q-factor is known for seismic waves in the study area, corrections for the effects of attenuation and velocity dispersion (non-stationarity of the source waveform) can be included in the approach. By using this resulting source waveform estimated at zero time, time-dependent waveforms can be predicted at any reflection time.

4) Tentatively, from a limited test with Weyburn seismic reflection data, the method also allows estimating the Q factor in the data.

7.2 Conclusions Related to Time-Lapse Seismic Monitoring

The waveform calibration consisting of time shifting, amplitude corrections and spectral shaping effectively eliminates the differences between the monitor and baseline traces outside of the reservoir interval so that accurate consistency of stacked images is achieved. Instead of direct subtraction of different seismic datasets, the TL reflectivity differences are evaluated through measurements performed during the waveform calibration. The TL AI analysis includes constraining a spatially-variable, low- frequency AI by using interval-velocity models, velocity-density relations and well log data, and a method for evaluating the AI difference from reflectivity difference and baseline AI. The key observations from the TL analysis of the Weyburn datasets are:

1) For both TL reflectivity difference and AI difference, they are stronger for monitor 2002 than for monitor 2001 and correlated with well-injection patterns. This is consistent with the progress of CO_2 injection.

2) The measured time shifts are about 0.5 – 1.5 ms, which indicate a P-wave velocity reduction up to 12% due to CO_2 injection.

3) Reductions of the AI in Marly is about 2 to 4.5% and around 3% in Vuggy, which are interpreted as caused by increases in CO_2 content and/or reservoir pore pressure.

4) Compared to AI decrease up to 15% estimated from P-wave velocity reduction, it is expected that the Frobisher carbonates beneath the reservoir may also be affected by the injected CO_2.

7.3 Conclusions for Seismic Wave Modeling

In Chapter 6, I argue that the widely used viscoelastic (VE) model is physically inconsistent when applied to model seismic wavefields in anelastic structures with sub-wavelength layering, such as the Weyburn reservoir. I proposed another approach for seismic wave modeling using first-principle continuum mechanics. Instead of the so-called correspondence principle and representing the anelasticity of the medium by a single, frequency-dependent factor Q, this modeling considers the body-force internal friction and boundary conditions (BC) in layered and heterogeneous media, which should cause dominant effects on seismic-wave attenuation and velocity dispersion. This rigorous modeling of seismic wave propagation was performed in a model of layered thin oil reservoir in the Weyburn Field with different types of BC (VE-type constraint, continuity, open, and closed). The key detailed conclusions from this modeling are:

1) Within the Weyburn reservoir, the drained-undrained transition (DUT) frequencies are comparable, and for Vuggy zone, they generally exceed the seismic frequencies. This means that this reservoir is in the DUT regime, and many layers may contain secondary waves across their whole thicknesses. In this case, non-VE effects should be essential in wave synthetics and in observations.

2) Most modeled observables are close when evaluated with “VE constraint”, “continuity” and “open” BCs but strongly different when using “closed” BC. Thus, boundary conditions between layers cause strong effects on wave propagation, and in particular on anelastic effects.

3) Many types of attenuation coefficients were modeled from wave synthetics, including the geometric, scattering, and fluctuation $\chi(f)$. Frequency-dependent arts of these $\chi(f)$ yield the corresponding empirical (apparent) Q-factors. These empirical Q-factors are strongly and complexly variable with frequency due to the tuning effects between layers. All Qs depend on boundary conditions assumed between layers.

4) In addition to the above empirical Q-factors, VE Q-factors were also determined from the modeled stress-strain ratios. These Q-factors may be strongly variable within each layer. The inverse VE Q^{-1} values strongly depend on boundary conditions assumed between layers and may range from near-zero to the average maximum values in the models.

5) One of the most important conclusions from this modeling is that, as suggested by the obtained broad attenuation spectra, the often-observed near-constant Q or broad attenuation peaks can be produced by contributions from multiple heterogeneities and layers traversed by the seismic wave. Thus, the Generalized Standard Linear Solid often used in the software for simulating seismic waves can be formed by multiple layers, each of which behaving as a Standard Linear Solid, with a single attenuation peak. BCs and numerous internal variables related to small-scale heterogeneities or thin layers are particularly important in this superposition.

7.4 Directions of Future Research

In this section, I outline several promising extensions and directions of the research topics of this Dissertation, in the order of their listing at the beginning of this Chapter. First, regarding the source-waveform estimation proposed in this dissertation, as shown in Chapter 3 the optimization procedure called *Estimation B* was unsuccessful in the recovery of the parameters of coherent noise, which consisted in amplification of the low-frequency part of the signal. However, I think that the *Estimation B* procedure may still be useful and can be studied further. Two potential approaches for its improvement can be tried. One approach could be to determine a new optimization criterion instead of the "width-amplitude" and "width-phase" optimizations used in Chapter 3. Another improvement of this method could be in using a better optimization approach. Instead of using the simple but rather inefficient grid-search approach which is restricted by the grid size, other methods such as random search or Bayesian optimization could be worth testing. Improved optimization methods may allow using more than two parameters and give an enhanced source waveform and coherent-noise reduction.

Another recommended research direction in the area of source-waveform estimation is the investigation of other applications of the estimated source waveform. Section 3.6 shows that this waveform-estimation approach can be used for estimating the Q factor in reflection seismic records and/or for optimizing the procedure of Q-compensation. Only an initial feasibility test for such estimation is shown in Chapter 3; however, its results appear to be very promising and deserve further research. With regard to this Q estimation, it is necessary to establish the degree of its accuracy and ability to determine depth and frequency dependencies of the Qs, and also

what type of Q (for example, intrinsic or scattering) can be measured best, and how this measurement is sensitive to the statistical and deterministic properties of well logs.

In the second large topic of TL seismic monitoring, there is also a substantial field of future development. One of the main topics worth further studying is extending the TL AI approaches of Chapter 5 to elastic impedance (EI). The AI equals the product of P-wave velocity and density only under the strict condition of normal incidence, whereas the EI broadly extends the seismic impedance to variable incidence angles or ray-parameter values. By accounting for oblique-incidence effects, the EI incorporates shear-wave and mode-conversion effects and therefore adds useful new information to the AI. Unfortunately, the EI is a non-rigorous concept, and several practical approximations were proposed by Connolly (1999), Whitcombe (2002), Santos and Tygel (2004) (the latter was also called the reflection impedance, or RI), and Ma and Morozov (2007). I performed initial calculations for these types of EI (Figure 7.1) based on the velocity and density logs of well 102042300614, In Figure 7.1, the S-wave velocity was measured within a limited range around the reservoir zone (Marly and Vuggy), and outside of this range, I estimated the S-wave velocities from the P-wave ones by using Castagna's et al. (1985) equation.

To apply the different EIs to the Weyburn TL 3-D 3-C or other seismic datasets, I suggest the following approximate work sequence:

1) Process the seismic datasets to achieve different angle and/or ray-parameter stacks.

2) Evaluate the reflectivity difference between monitors and baseline for different angle and/or ray-parameter stacks by the methods of Chapter 4.

3) Calculate EI for baseline dataset through the inversion method proposed for AI in Chapter 5.

4) Evaluate the TL EI from the reflectivity difference in step 2) and baseline EI in step 3).

The obtained TL EI can provide further indications for the time-lapse analysis of the present Weyburn project and/or other TL seismic monitoring projects. In addition to the three types of EIs suggested above, it should be useful to continue exact, rigorous elastic P/SV impedances, which is the matrix quantity proposed by Morozov (2010). This EI can accurately describe both the P- and S-wave reflectivities and could also be inverted and interpreted in the same way as the AI. However, inverting it from seismic data requires knowledge of the P/P and S/S reflectivities and P/S mode conversions, which are not available from the data. Morozov (2010) suggested that this matrix quantity can be derived by λ, μ, and ρ (elastic moduli and density of the material, often referred to as LMR) inversion or directly from amplitude variations of reflectivity with offset (AVO).

Finally, the third topic of wave modeling in anelastic media is completely new and suggests an enormous number of further extensions and follow-up research. In particular, production-quality (3-D, implemented in C++ and/or Fortran, and integrated with other tools) software for frequency- and time-domain (in particular, finite-difference) modeling of seismic waves in layered and more complex media needs to be created. The types and properties of internal variables in different materials and media need to be studied. Anelastic mechanical material properties for rock, such as solid viscosities, elastic and viscous coupling have also been not studied, with only first estimates made by Deng and Morozov (2018b) and Morozov and Deng (2018a). Mechanical properties of rock also need to be studied by numerical modeling,

similar, for example, to Tisato and Quintal (2013) and Rubino and Holliger (2013), but using rigorous mechanics instead of viscoelastic hypotheses, DEVM approximations, and frequency-dependent material properties. Boundary conditions between layers and heterogeneities need to be measured and modeled. Effects of small-scale fracturing of the reservoirs need to be included, which can probably be done by using the concepts of "damage rheology" (Lyakhovsky and Ben-Zion, 2013) and nonlinear Lagrangian mechanics (Coulman et al., 2013; Deng and Morozov, 2018a).

On the application side of the wavefield modeling in Chapter 6, in future studies, amplitude and apparent-Q variations with offset need to be studied in detail for different rock and saturation-fluid types, and for different boundary conditions between layers. It would also be useful to analyse acoustic and elastic impedances resulting from such models and thus validate and calibrate the observations in Chapters 4 and 5. If rigorous continuum-mechanics models such as described in Chapter 6 are created, these models should be possible to use not only for wave simulation but also in any other applications, such as modeling laboratory experiments with rock samples (Morozov and Deng, 2018a) and simulations of fluid flows within reservoirs. These properties of the model also offer a broad range of connections with numerous existing and future studies.

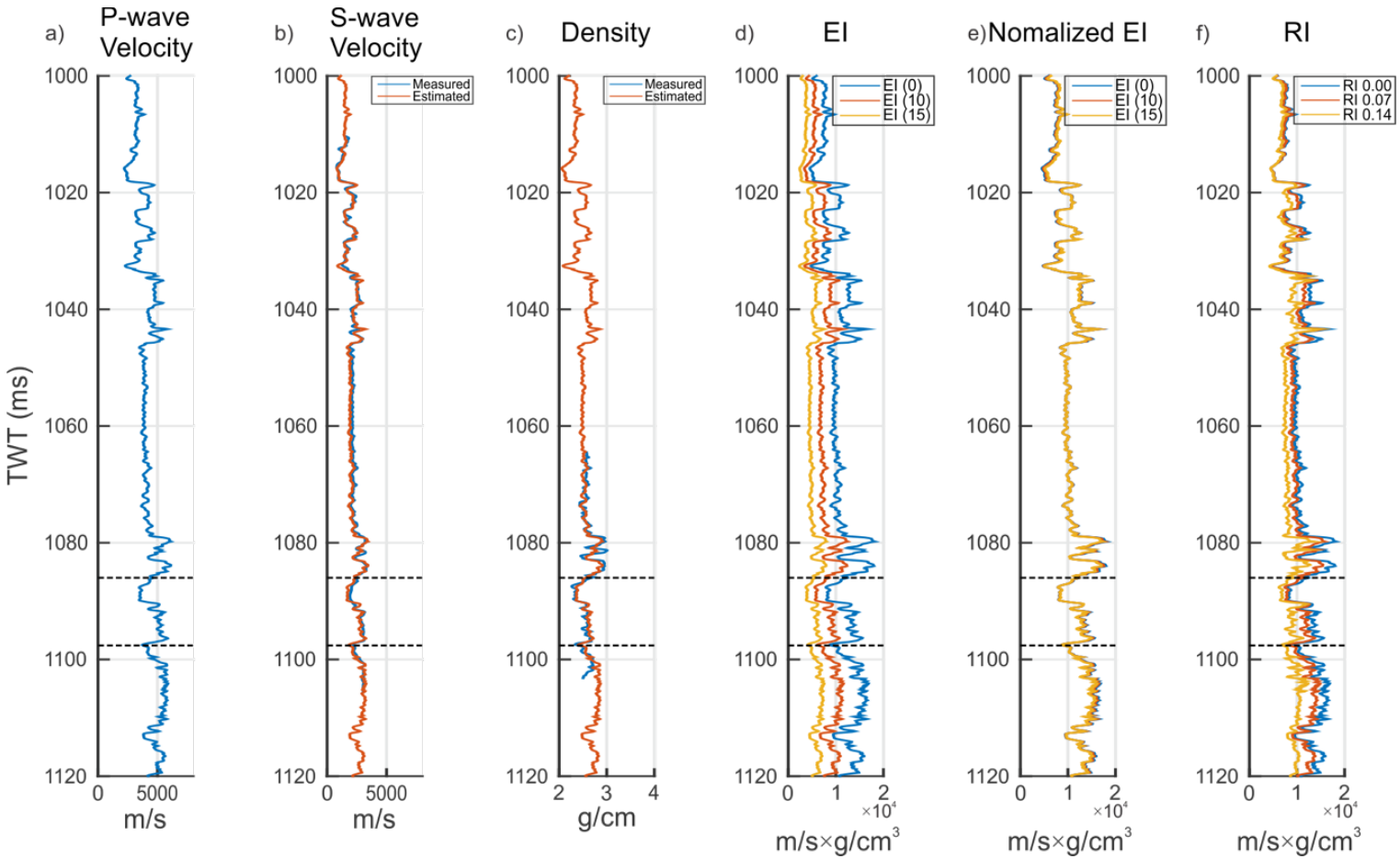

Figure 7.1. Three types of EI calculated from well logs: a) P-wave velocity log; b) measured and estimated S-wave velocity log (blue and red lines); c) measured and estimated density log (blue and red lines); d) Connelly's (1999) EI for the degree of 0, 10 and 15; e) Whitcombe's (2002) normalized EI for the degree of 0, 10 and 15; f) RI (Santos and Tygel, 2004) for the ray parameter p of 0, 0.07, and 0.14 ms/m. Grey dashed lines in each panel show the top and bottom of the reservoir zone (Marly and Vuggy).

LIST OF REFERENCES

Aki, K., and P. G. Richards, 2002, Quantitative seismology, 2nd ed.: University Science Books.

Angeleri, G. P., 1983, A statistical approach to the extraction of the seismic propagating wavelet: Geophysical Prospecting, **31**, 726–747, doi: 10.1111/j.1365-2478.1983.tb01082.x.

Aquistore Working Group, 2016, Aquistore project annual report: Petroleum Technology Research Centre, http://aquistore.ca/+pub/AQ%20Annual%20Report%202016%20Final.pdf, last accessed 30 September 2019.

Arts, R., O. Eiken, A. Chadwick, P. Zweigel, L. Van der Meer, and B. Zinszner, 2004, Monitoring of CO_2 injected at Sleipner using time-lapse seismic data: Energy, **29**, 1383–1392, doi: 10.1016/j.energy.2004.03.072.

Ba, J., W. Xu, L. Y. Fu, J. M. Carcione, and L. Zhang, 2017, Rock anelasticity due to patchy saturation and fabric heterogeneity: A double double-porosity model of wave propagation: Journal of Geophysical Research: Solid Earth, **122**, 1949–1976, doi: 10.1002/2016JB013882.

Baharvand Ahmadi, A., 2016, Analysis of time-lapse 3-D VSP data for seismic monitoring of CO_2 flood in Weyburn Field, Saskatchewan: Ph.D. thesis, University of Saskatchewan.

Baharvand Ahmadi, A., L. Gao, J. Ma, and I. B. Morozov, 2011, CO_2 saturation vs. pressure effects from time-lapse 3-D P-S surface and VSP seismic data,

http://seisweb.usask.ca/Reports/Weyburn_USask_Report_Apr2011.pdf, last accessed 1 November 2018.

Baharvand Ahmadi, A., and I. Morozov, 2013, Anisotropic frequency-dependent spreading of seismic waves from first-arrival vertical seismic profile data analysis: Geophysics, **78**, no. 6, C41–C52, doi: 10.1190/geo2012-0401.1.

Biot, M.A., 1956, Theory of propagation of elastic waves in a fluid-saturated porous solid, II. Higher-frequency range: Journal of the Acoustical Society of America, **28**, 168–178, doi: 10.1121/1.1908241.

Blias, E., 2012, Accurate interval *Q*-factor estimation from VSP data: Geophysics, **77**, no. 3, WA149-WA156, doi: 10.1190/geo2011-0270.1.

Brown, L. T., 2002, Integration of rock physics and reservoir simulation for the interpretation of time-lapse seismic data at Weyburn Field, Saskatchewan: M.S. thesis, Colorado School of Mines.

Buland, A., and H. Omre, 2003, Bayesian wavelet estimation from seismic and well data: Geophysics, **68**, 2000–2009, doi: 10.1190/1.1635053.

Buland, A., and Y. El Ouair, 2006, Bayesian time-lapse inversion: Geophysics, **71**, no. 3, R43–R48, doi: 10.1190/1.2196874.

Bunge, R. J., 2000, Midale reservoir fracture characterization using integrated well and seismic data, Weyburn Field, Saskatchewan: M.S. thesis, Colorado School of Mines.

Carcione, J. M, 1996, Wave propagation in anisotropic, saturated porous media: Plane-wave theory and numerical simulation: Journal of the Acoustical Society of America, **99**, 2655–2666, doi: 10.1121/1.414809.

Carcione, J. M., 2007, Wave fields in real media: Wave propagation in anisotropic anelastic, porous, and electromagnetic media. 2nd ed.: Elsevier.

Carcione, J. M. and S. Picotti, 2006, P-wave seismic attenuation by slow-wave diffusion: Effects of inhomogeneous rock properties: Geophysics, **71**, no. 3, O1–O8, doi: 10.1190/1.2194512.

Castagna, J. P., M. L. Batzle, and R. L. Eastwood, 1985, Relationships between compressional-wave and shear-wave velocities in clastic silicate rocks: Geophysics, **50**, 571-581, doi: 10.1190/1.1441933.

Castagna, J., S. Sun, and R. Siegfried, 2003, Instantaneous spectral analysis: Detection of low-frequency shadows associated with hydrocarbons: The Leading Edge, **22**, 120–127, doi: 10.1190/1.1559038.

Chabyshova, E., and G. Goloshubin, 2014, Seismic modelling of low-frequency "shadows" beneath gas reservoirs: Geophysics, **79**, no. 6, D417–D423, doi: 10.1190/geo2013-0379.1.

Chen, H., K. A. Innanen, and T. Chen, 2018, Estimating P- and S-wave inverse quality factors from observed seismic data using an attenuative elastic impedance: Geophysics, **83**, no. 2, R173–R187, doi: 10.1190/geo2017-0183.1.

Connolly, P., 1999, Elastic impedance: The Leading Edge, **18**, 438–452, doi: 10.1190/1.1438307.

Cooke, D. A., and W. A. Schneider, 1983, Generalized linear inversion of reflection seismic data: Geophysics, **48**, 665–676, doi: 10.1190/1.1441497.

Coulman, T., W. Deng, and I. B. Morozov, 2013, Models of seismic attenuation measurements in the laborator: Canadian Journal of Exploration Geophysics, **38**, 51–67.

Dadashpour, M., M. Landrø, and J. Kleppe, 2008, Nonlinear inversion for estimating reservoir parameters from time-lapse seismic data: Journal of Geophysical Engineering, **5**, 54–66, doi: 10.1088/1742-2132/5/1/006.

Dai, Y.-S., R.-R. Wang, C. Li, P. Zhang, and Y.-C. Tan, 2016, A time-varying wavelet extraction using local similarity: Geophysics, **81**, no. 1, V55–V68, doi: 10.1190/geo2015-0317.

Danielson, V., and T. V. Karlsson, 1984, Extraction of signatures from seismic and well data: First Break, **2**, 15–21, doi: 10.3997/1365-2397.1984008.

Day, S., and J. B. Minster, 1984, Numerical simulation of attenuated wavefields using a Pade approximant method: Geophysical Journal International, **78**, 105–118, doi: 10.1111/j.1365-246X.1984.tb06474.x.

Declercq, N. F., R. Briers, J. Degrieck, and O. Leroy, 2005, The history and properties of ultrasonic inhomogeneous waves: IEEE Transactions on ultrasonics, ferroelectrics, and frequency control, **52**, 776–791, doi: 10.1109/TUFFC.2005.1503963.

Deng, W., and I. B. Morozov, 2016, Solid viscosity of fluid-saturated porous rock with squirt flows at seismic frequencies: Geophysics, **81**, No. 4, D381–D390, doi: 10.1190/geo2015-0406.1.

Deng, W., and I. B. Morozov, 2018a, Causality relations and mechanical interpretation of band-limited seismic attenuation: Geophysical Journal International, **215**, 1622–1632, doi: 10.1093/gji/ggy354.

Deng, W., and I. B. Morozov, 2018b, Mechanical interpretation and generalization of the Cole-Cole model in viscoelasticity: Geophysics, **83**, No. 6, MR345–MR352, doi: 10.1190/geo2017-0821.1.

Druzhinin, A, and C. MacBeth, 2001, Robust cross-equalization of 4D-4C PZ migrated data at Teal South: 71th Annual International Meeting, SEG, Expanded Abstracts, 1670–1673, doi: 10.1190/1.1816439.

Dunn, K.-J., 1987, Sample boundary effect in acoustic attenuation of fluid-saturated porous cylinders: Journal of the Acoustical Society of America, **81**, 1259–1266, doi: 10.1121/1.394529.

Edgar, J. A., and M. van der Baan, 2011, How reliable is statistical wavelet estimation?: Geophysics, **76**, no. 4, V59–V68, doi: 10.1190/1.3587220.

Fomel, S., and L. Jin, 2009, Time-lapse image registration using the local similarity attribute: Geophysics, **74**, no. 2, A7–A11, doi: 10.1190/1.3054136.

Fuchs, K. and G. Müller, 1971, Computation of synthetic seismograms with the reflectivity method and comparison with observations: Geophysical Journal International, **23**, 417–433, doi: 10.1111/j.1365-246X.1971.tb01834.x.

Gao, L., 2016, Shear-wave and spatial attributes in time-lapse 3-D/3-C seismic and potential-field datasets: Ph.D. thesis, University of Saskatchewan.

Gao, L., and I. B. Morozov, 2011, AVO analysis of 3-D/3-C datasets from Weyburn CO_2 Storage and Monitoring Project: 2011 CSPG CSEG CWLS Conference, CSPG/CSEG/CWLS, Abstracts, https://www.geoconvention.com/conference/abstract-archives/2011-abstracts.html, last accessed 1 November 2018.

Gardner, G. H. F., L. W. Gardner, and A. R. Gregory, 1974, Formation velocity and density—the diagnostic basics for stratigraphic traps: Geophysics, **39**, 770–780, doi: 10.1190/1.1440465.

Geertsma, J., and D. C. Smit, 1961, Some aspects of elastic wave propagation in fluid-saturated porous solids: Geophysics, **26**, 169–181, doi: 10.1190/1.1438855.

Grana, D., and T. Mukerji, 2015, Bayesian inversion of time-lapse seismic data for the estimation of static reservoir properties and dynamic property changes: Geophysical Prospecting, **63**, 637–655, doi: 10.1111/1365-2478.12203.

Gurevich, B., V. B. Zyrianov, and S. L. Lopatnikov, 1997, Seismic attenuation in finely layered porous rocks: Effects of fluid flow and scattering: Geophysics, **62**, 319-324, doi: 10.1190/1.1444133.

Hale, D., 2009, A method for estimating apparent displacement vectors from time-lapse seismic images: Geophysics, **74**, no. 5, V99–V107, doi: 10 .1190/1.3184015.

Herawati, I., and T. L. Davis, 2002, The use of time-lapse P-wave impedance inversion to monitor a CO_2 flood at Weyburn Field, Saskatchewan: M.S. thesis, Colorado School of Mines.

Holliger, K., 1996, Upper-crustal seismic velocity heterogeneity as derived from a variety of P-wave sonic logs: Geophysical Journal International, **125**, 813–829, doi: 10.1111/j.1365-246X.1996.tb06025.x.

Kazemi, N., and M. D. Sacchi, 2014, Sparse multichannel blind deconvolution: Geophysics, **79**, no. 5, V143–V152, doi: 10.1190/geo2013-0465.1.

Kennett, B. L. N., 1983, Seismic wave propagation in stratified media: Cambridge University Press.

Knopoff, L., 1964, Q: Reviews of Geophysics, **2**, 625–660, doi: 10.1029/RG002i004p00625.

Korn, G., and T. Korn, 2000, Mathematical Handbook for Scientists and Engineers, 2nd ed.: Dover.

Lakes, R., 2009, Viscoelastic materials: Cambridge University Press.

Lancaster, S., and D. Whitcombe, 2000, Fast-track 'coloured' inversion: 70th Annual International Meeting, SEG, Expanded Abstracts, 1572–1575, doi: 10.1190/1.1815711.

Landau L.D. and E. M. Lifshitz, 1986, Theory of elasticity, 3rd ed.: Elsevier.

Landrø, M., 2001, Discrimination between pressure and fluid saturation changes from time-lapse seismic data: Geophysics, **66**, 836–844, doi: 10.1190/1.1444973.

Latimer, R. B., R. Davison, and P. van Riel, 2000, An interpreter's guide to understanding and working with seismic-derived acoustic impedance data: The Leading Edge, **19**, 242–256, doi: 10.1190/1.1438580.

Lazear, G. D., 1993, Mixed-phase wavelet estimation using fourth-order cumulants: Geophysics, **58**, 1042–1051, doi: 10.1190/1.1443480.

Lindseth, R. O., 1979, Synthetic sonic logs—A process for stratigraphic interpretation: Geophysics, **44**, 3–26, doi: 10.1190/1.1440922.

Lines, L. R., and T. J. Ulrych, 1977, The old and the new in seismic deconvolution and wavelet estimation: Geophysical Prospecting, **25**, 512–540, doi: 10.1111/j.1365-2478.1977.tb01185.x.

Lines, L. R., and S. Treitel, 1985, Wavelets, well logs and Wiener filters: First Break, **3**, 9–14, doi: 10.3997/1365-2397.1985014.

Liu, H. P., D. L. Anderson, and H. Kanamori, 1976, Velocity dispersion due to anelasticity: Implications for seismology and mantle composition: Geophysical Journal of the Royal Astronomical Society, **47**, 41–58, doi: 10.1111/j.1365-246X.1976.tb01261.x.

Longbottom, J., A. T. Walden, and R. E. White, 1988, Principles and application of maximum kurtosis phase estimation: Geophysical Prospecting, **36**, 115–138, doi: 10.1111/j.1365-2478.1988.tb02155.x.

Lumley, D. E., 2001, Time-lapse seismic reservoir monitoring: Geophysics, **66**, 50–53, doi: 10.1190/1.1444921.

Lumley, D. E., 2010, 4D seismic monitoring of CO_2 sequestration: The Leading Edge, **29**, 150–155, doi: 10.1190/1.3304817.

Lyakhovsky, V., and Y. Ben-Zion, 2013, Damage–breakage rheology model and solid-granular transition near brittle instability: Journal of the Mechanics and Physics of Solids, **64**, 184–197, doi: 10.1016/j.jmps.2013.11.007i.

Ma, J., and I. B. Morozov, 2007, The exact elastic impedance for P-SV wave: 77th Annual International Meeting, SEG, Expanded Abstracts, 288–292, doi: 10.1190/1.2792428.

Ma, J., and I. B. Morozov, 2010, AVO modeling of pressure-saturation effects in Weyburn CO_2 sequestration: The Leading Edge, **29**, 178–183, doi: 10.1190/1.3304821.

Mavko, G., and D. Jizba, 1991, Estimating grain-scale fluid effects on velocity dispersion in rocks: Geophysics, **56**, 1940–1949, doi: 10.1190/1.1443005.

McKenzie, D., 1984, The generation and compaction of partially molten rock: Journal of Petrology, **25**, 713–765, doi: 10.1093/petrology/25.3.713.

Milani, M., J. G. Rubino, T. M. Müller, B. Quintal, E. Caspari, and K. Holliger, 2016a, Representative elementary volumes for evaluating effective seismic properties of heterogeneous poroelastic media: Geophysics, **81**, no. 2, D169–D181, doi: 10.1190/geo2015-0173.1.

Milani, M., L. Monachesi, J. I. Sabbione, J. G.Rubino. and K. Holliger, 2016b, A generalized effective anisotropic poroelastic model for periodically layered media accounting for both

Biot's global and interlayer flows: Geophysical Prospecting, **64**, 1135–1148, doi: 10.1111/1365-2478.12406.

Morozov, I. B., 2008a, Open-source software framework integrates data analysis: Eos, Transaction, American Geophysical Union, **89**, 261-262, doi: 10.1029/2008EO290002.

Morozov, I. B., 2008b, Geometric attenuation, frequency dependence of *Q*, and the absorption band problem: Geophysical Journal International, **175**, 239–252, doi: 10.1111/j.1365-246X.2008.03888.x.

Morozov, I. B., 2010, Exact elastic P/SV impedance: Geophysics, **75,** no. 2, C7–C13, doi: 10.1190/1.3318268.

Morozov, I. B., 2015, Effective moduli and Poisson's ratios in poroelasticity: Canadian Journal of Exploration Geophysics, **40**, 21–34.

Morozov, I. B., 2019, Mechanics of seismic *Q*: Recorder, **44**, no.1, 20-24.

Morozov, I. B., and L. Gao, 2009, Multi-vintage, pre-stack calibration of 3-C 3-D time-lapse seismic data: 2009 CSPG CSEG CWLS Conference, https://www.geoconvention.com/conference/abstract-archives/2009-abstracts.html, last accessed 1 November 2018.

Morozov, I. B., and J. Ma, 2009, Accurate poststack acoustic-impedance inversion by well-log calibration: Geophysics, **74**, no. 5, R59–R67, doi: 10.1190/1.3170687.

Morozov, I. B. and A. Baharvand Ahmadi, 2015, Taxonomy of Q: Geophysics, **80**, no. 1, T41–T49, doi: 10.1190/geo2013-0446.1.

Morozov, I. B. and W. Deng, 2016a, Macroscopic framework for viscoelasticity, poroelasticity, and wave-induced fluid flows—Part 1: General linear solid: Geophysics, **81**, no. 1, L1–L13, doi: 10.1190/geo2014-0171.1.

Morozov, I. B. and W. Deng, 2016b, Macroscopic framework for viscoelasticity, poroelasticity, and wave-induced fluid flows—Part 2: Effective media: Geophysics, **81**, no. 4, D405–D417, doi: 10.1190/geo2014-0404.1.

Morozov, I. B. and W. Deng, 2018a, Inversion for Biot-consistent material properties in subresonant oscillation experiments with fluid-saturated porous rock: Geophysics, **83**, no. 2, MR67–MR79, 10.1190/geo2017-0511.1.

Morozov, I. B. and W. Deng, 2018b, Internal boundary conditions in heterogeneous anelastic media: Geophysical Journal International, **215**, 2047–2059, doi: 10.1093/gji/ggy387.

Morozov, I. B., W. Deng, and L. Lines, 2018a, Ultrasonic wave propagation and reflections in "heavy oil" (Crisco): Canadian Journal of Exploration Geophysics, **43**, 1–12.

Morozov, I. B., M. Haiba, and W. Deng, 2018b, Inverse attenuation filtering: Geophysics, **83**, no.2, V135–V147, doi: 10.1190/geo2016-0211.1.

Müller, T.M., B. Gurevich, and M. Lebedev, 2010, Seismic wave attenuation and dispersion resulting from wave-induced flow in porous rocks—A review: Geophysics, **75**, no. 5, 75A147−75A164, doi: 10.1190/1.3463417.

Murphy, W. L., K. W. Winkler, and R. L. Kleinberg, 1986, Acoustic relaxation in sedimentary rocks: Dependence on grain contacts and fluid saturation: Geophysics, **51**, 757-766, doi: 10.1190/1.1442128.

Oldenburg, D. W., S. Levy, and K. P. Whittal, 1981, Wavelet estimation and deconvolution: Geophysics, **46**, 1528–1542, doi: 10.1190/1.1441159.

Pimienta, L., J. Fortin, and Y. Guéguen, 2015a, Bulk modulus dispersion and attenuation in sandstones: Geophysics, **80**, no. 2, D111–D127, doi: 10.1190/geo2014-0335.1.

Pimienta, L., J. Fortin, and Y. Guéguen, 2015b, Experimental study of Young's modulus dispersion and attenuation in sandstones: Geophysics **80**, no. 5, L57–L72, doi:10.1190/GEO2014-0532.1.

Pimienta, L., J.V.M. Borgomano, J. Fortin, and Y. Guéguen, 2016, Modelling the drained/undrained transition: effect of the measuring method and the boundary conditions: Geophysical Prospecting, **64**, 1098–1111, doi: 10.1111/1365-2478.12390.

Prieux, V., R. Brossier, S. Operto, and J. Virieux, 2013, Multiparameter full waveform inversion of multicomponent OBC data from Valhall field. Part 1: imaging compressional wavespeed, density and attenuation: Geophysical Journal International, **194**, 1640–1664, doi: 10.1093/gji/ggt177.

Qadrouh, A.N., J. M. Carcione, J. Ba, D. Gei, and A. M. Salim, 2018, Backus and Wyllie averages for seismic attenuation: Pure and Applied Geophysics, **175**, 165–170, doi: 10.1007/s00024-017-1676-x.

Ricker, N., 1953, The form and laws of propagation of seismic wavelets: Geophysics, **18**, 10–40, doi: 10.1190/1.1437843.

Rickett, J. E., and D. E. Lumley, 2001, Cross-equalization data processing for time-lapse seismic reservoir monitoring: A case study from the Gulf of Mexico: Geophysics, **66**, 1015–1025, doi: 10.1190/1.1487049.

Robinson, E. A., 1957, Predictive decomposition of seismic traces: Geophysics, **22**, 767–778, doi: 10.1190/1.1438415.

Ross, C. P., G. B. Cunningham, and D. P. Weber, 1996, Inside the crossequalization black box: The Leading Edge, **15**, 1233–1240, doi: 10.1190/1.1437231.

Rubino, J., and K. Holliger, 2013, Research note: Seismic attenuation due to wave-induced fluid flow at microscopic and mesoscopic scales: Geophysical Prospecting, **61**, 882-889, doi: 10.1111/1365-2478.12009.

Russell, B., 1988, Introduction to seismic inversion methods: SEG.

Russell, B., and D. Hampson, 1991, Comparison of post-stack seismic inversion methods: 61st Annual International Meeting, SEG, Expanded Abstracts, 876–878, doi: 10.1190/1.1888870.

Sacchi, M. D., D. R. Velis, and A. H. Comínguez, 1994, Minimum entropy deconvolution with frequency-domain constraints: Geophysics, **59**, 938–945, doi: 10.1190/1.1443653.

Sahay, P. N., 2008, On the Biot slow S-wave: Geophysics, **73**, no. 4, N19–N33, doi: 10.1190/1.2938636.

Santos, L. T., and M. Tygel, 2004, Impedance-type approximations of the P-P elastic reflection coefficient: Modeling and AVO inversion: Geophysics, **69**, 592-598, doi: 0.1190/1.1707079.

Solazzi, S.G., J. G. Rubino, T. Müller, M. Milani, L. Guarracino, and K. Holliger, 2016, An energy-based approach to estimate seismic attenuation due to wave-induced fluid flow in heterogeneous poroelastic media: Geophysical Journal International, **207**, 823–832, doi: 10.1093/gji/ggw302.

Stammeijer, J. G. F, and P. J. Hatchell, 2014, Standards in 4D feasibility and interpretation: The Leading Edge, **33**, 134–140, doi: 10.1190/tle33020134.1.

Tarantola, A., 2005, Inverse problem theory and methods for model parameter estimation: SIAM.

Tisato, N., and B. Quintal, 2013, Measurements of seismic attenuation and transient fluid pressure in partially saturated Berea sandstone: evidence of fluid flow on the mesoscopic scale: Geophysical Journal International, **195**, 342–351, doi: 10.1093/gji/ggt259.

Ulrych, T. J., 1971, Application of homomorphic deconvolution to seismology: Geophysics, **36**, 650–660, doi: 10.1190/1.1440202.

Ursin, B. and A. Stovas, 2002, Reflection and transmission responses of a layered isotropic viscoelastic medium: Geophysics, **67**, 307–323, doi: 10.1190/1.1451803.

van der Baan, M., 2008, Time-varying wavelet estimation and deconvolution by kurtosis maximization: Geophysics, **73**, no. 2, V11–V18, doi: 10.1190/1.2831936.

Velis, D. R., and T. J. Ulrych, 1996, Simulated annealing wavelet estimation via fourth-order cumulant matching: Geophysics, **61**, 1939–1948, doi: 10.1190/1.1444109.

Wang, Y., 2008, Seismic inverse *Q* filtering: Blackwell.

Wang, Y., and I. B. Morozov, 2016, Constraining acoustic impedance inversion by seismic-processing velocities: 78th Conference and Exhibition, EAGE, Extended Abstracts, P612, doi: 10.3997/2214-4609.201601439.

Wang, Y., and I. B. Morozov, 2017, Time-lapse acoustic impedance variations after CO2 injection in Weyburn Field: 87th Annual International Meeting, SEG, Expanded Abstracts, 5890–5894, doi: 10.1190/segam2017-17752011.1.

Wang, Y., W. Deng and I. B. Morozov, 2018, A simple wavelet-estimation approach for well-log to seismic tying: GeoConvention 2018, CSPG/CSEG/CWLS, Abstracts, https://www.geoconvention.com/archives/2018/207_GC2018_A_Simple_Wavelet-Estimation_Approach_for_Well-Log%20to_Seismic_Tying.pdf, last accessed 1 May 2019.

Wang, Y., and I. B. Morozov, 2018, Waveform calibration of time-lapse seismic data: GeoConvention 2018, CSPG/CSEG/CWLS, Abstracts, https://www.geoconvention.com/archives/2018/204_GC2018_Waveform_Calibration_of_Time-Lapse_Seismic_Data.pdf, last accessed 1 May 2019.

Wang, Y., and I. B. Morozov, 2019, Modeling Seismic Waves in Layered Anelastic Media – beyond the Viscoelastic Approach: GeoConvention 2019, CSPG/CSEG/CWLS,

Abstracts, https://www.geoconvention.com/uploads/2019abstracts/GC2019_136_Modeling_Seismic_Waves_in_Layered_Anelastic_Media.pdf, last accessed 7 July 2019.

Wang, Y., and I. B. Morozov, submitted I, A simple approach to non-stationary source waveform estimation in seismic records, submitted to Geophysics, in revision.

Wang, Y., and I. B. Morozov, submitted II, Time-lapse acoustic impedance variations during CO_2 injection in Weyburn oilfield, Canada, submitted to Geophysics, accepted.

Wang, Y., and I. B. Morozov, submitted III, Seismic responses of layered linear anelastic solids – Wave-induced internal deformations beyond the viscoelastic model, submitted to Geophysics, in revision.

Wegelin, A., 1984, Geology and reservoir properties of the Weyburn Field, southeastern Saskatchewan, in J. A. Lorsong, and M. A. Wilson, eds., Oil and gas in Saskatchewan: Saskatchewan Geological Society Special Publication Number 7, 71–82.

Whitcombe, D. N., 2002, Elastic impedance normalization, Geophysics, **67**, 60-62, doi: 10.1190/1.1451331.

White, J. E., 1975, Computed seismic speeds and attenuation in rocks with partial gas saturation: Geophysics, **40**, 224–232, doi: 10.1190/1.1440520.

White, J. E., 1986, Biot-Gardner theory of extensional waves in porous rods: Geophysics, **51**, 742–745, doi: 10.1190/1.1442126.

White, R. E., 1992, The accuracy of estimating Q from seismic data: Geophysics, **57**, 1508–1511, doi: 10.1190/1.1443218.

White, D. J., 2008, Geophysical Monitoring in the IEA GHG Weyburn-Midale CO_2 Monitoring and Storage Project: 78th Annual International Meeting, SEG, Expanded Abstracts, 2846-2849, doi: 10.1190/1.3063936.

White, D. J., 2009, Monitoring CO_2 storage during EOR at the Weyburn-Midale Field: The Leading Edge, **28**, 838–842, doi: 10.1190/1.3167786.

White, D. J., for the Weyburn Geophysical Monitoring Team, 2011, Geophysical monitoring of the Weyburn CO_2 flood: Results during 10 years of injection: Energy Procedia **4**, 3628–3635, doi: 10.1016/j.egypro.2011.02.293.

White, D. J., 2013, Seismic characterization and time-lapse imaging during seven years of CO_2 flood in the Weyburn field, Saskatchewan, Canada: International Journal of Greenhouse Gas Control, **16**, suppl. 1, S78–S94, doi: 10.1016/j.ijggc.2013.02.006.

White, D. J., K. Hirsche, T. Davis, I. Hutcheon, R. Adair, G. Burrowes, S. Graham, R. Bencini, E. Majer, and S. C. Maxwell, 2004a, Theme 2: Prediction, monitoring and verification of CO_2 movements, in M. Wilson, and M. Monea, eds., IEA GHG CO_2 Monitoring and Storage Project summary report 2000–2004: Petroleum Technology Research Centre, 73–148.

White, D. J., G. Burrowes, T. Davis, Z. Hajnal, K. Hirsche, I. Hutcheon, E. Majer, B. Rostron, and S. Whittaker, 2004b, Greenhouse gas sequestration in abandoned oil reservoirs: The International Energy Agency Weyburn pilot project: GSA Today, **14**, no. 7, 4–10, doi: 10.1130/1052-5173(2004)014<004:GGSIAO>2.0.CO;2.

White, D. J., C. D. Hawkes, and B. J., Rostron, 2016, Geological characterization of the Aquistore CO_2 storage site from 3D seismic data: International Journal of Greenhouse Gas Control, **54**, 330–344, doi: 10.1016/j.ijggc.2016.10.001.

Wiggins, R., 1978, Minimum entropy deconvolution: Geoexploration, **16**, 21–35, doi: 10.1016/0016-7142(78)90005-4.

Yao, Q., D. Han, F. Yan, and L. Zhao, 2015, Modeling attenuation and dispersion in porous heterogeneous rocks with dynamic rock modulus: Geophysics, **80**, no. 3, D183–D194, doi: 10.190/geo2013-0410.1.

Yuan, S., S. Wang, Y. Luo, W. Wei, and G. Wang, 2019, Impedance inversion by using the low-frequency full-waveform inversion result as an a priori model: Geophysics, **84** no. 2, R149–R164, doi: 10.1190/geo2017-0643.1.

APPENDIX A

MINIMUM-PHASE TRANSFORMATION AND WAVEFORM PROXIMITY TO MINIMUM PHASE

For a given waveform $w(t)$, let me define its minimum-phase equivalent $w_{\min}(t)$ as another waveform with the same amplitude spectrum $A(\omega)$ but minimum-phase character. The phase spectrum $\phi_{\min}(\omega)$ for this waveform equals

$$\phi_{\min}(\omega) = -\mathbf{H}\{\ln A(\omega)\}, \tag{A.1}$$

where **H** is the Hilbert transform. Consequently, the minimum-phase equivalent of $w(t)$ is

$$w_{\min}(t) = \mathbf{F}^{-1}\left\{Ae^{i\phi_{\min}}\right\} = \mathbf{F}^{-1}\left\{Ae^{-i\mathbf{H}\{\ln A\}}\right\}, \tag{A.2}$$

where $\mathbf{F}^{-1}$ denotes the inverse Fourier transform. The maximum-phase equivalent $w_{\max}(t)$ can be similarly obtained by reversing the sign of "i" in equation (A.2).

Let us further define the total energy in the wave form $w(t)$ ($t \in [-T/2, T/2]$) as $S = \int_{-T/2}^{T/2} E(t)\,dt$, where $E(t) = \int_{-T/2}^{t} A^2(\tau)\,d\tau$, and similarly $S_{\min}$ and $S_{\max}$ for $w_{\min}(t)$ and $w_{\max}(t)$. Then, a measure of "proximity" of $w(t)$ to $w_{\min}(t)$ suitable for inclusion in the objective functions (3.6) can be evaluated as

$$Y = \frac{S_{\max} - S}{S_{\min} - S_{\max}}. \tag{A.3}$$

This quantity varies between –1 when $w(t)$ is minimum-phase and 0 when it is maximum-phase.

APPENDIX B

DISPLACEMENT, STRAIN, AND STRESS MATRICES FOR WAVE MODES

From equations (6.4) and (6.7) in the text, the displacements, strains, and stresses for the different components of the medium can be expressed in terms of the corresponding wavenumber and polarization vectors:

$$\mathbf{U}_m^l\left(\vec{r}\right)=\begin{pmatrix} n_z\mathbf{u}_m \\ n_x\mathbf{u}_m \end{pmatrix} e^{i\vec{k}\vec{r}}\,, \tag{B.1a}$$

$$\mathbf{E}_m^l\left(\vec{r}\right)=\begin{bmatrix} \mathbf{I}\partial_z & 0 \\ 0 & \mathbf{I}\partial_x \\ \mathbf{I}\dfrac{\partial_x}{2} & \mathbf{I}\dfrac{\partial_z}{2} \end{bmatrix}\mathbf{U}_m^l=\begin{pmatrix} ik_z n_z\mathbf{u}_m \\ ik_x n_x\mathbf{u}_m \\ \dfrac{ik_x n_z+ik_z n_x}{2}\mathbf{u}_m \end{pmatrix} e^{i\vec{k}\vec{r}}\,, \tag{B.1b}$$

$$\mathbf{\Sigma}_m^l\left(\vec{r}\right)=\begin{bmatrix} \mathbf{M}^* & \boldsymbol{\lambda}^* & 0 \\ \boldsymbol{\lambda}^* & \mathbf{M}^* & 0 \\ 0 & 0 & \boldsymbol{\mu}^* \end{bmatrix}\mathbf{E}_m^l=\begin{pmatrix} ik_z n_z\mathbf{M}^*\mathbf{u}_m+ik_x n_x\boldsymbol{\lambda}^*\mathbf{u}_m \\ ik_x n_x\mathbf{M}^*\mathbf{u}_m+ik_z n_z\boldsymbol{\lambda}^*\mathbf{u}_m \\ \dfrac{ik_x n_z+ik_z n_x}{2}\boldsymbol{\mu}^*\mathbf{u}_m \end{pmatrix} e^{i\vec{k}\vec{r}}\,, \tag{B.1c}$$

where **I** denotes the $N\times N$ identity matrix, the layer number l and time-dependent factors $e^{-i\omega t}$ are implied, and vectors $\vec{k}$ (upward or downward, P- or S-wave) and $\vec{n}$ (for P or S waves) are determined by the mode number m. In these relations, $\boldsymbol{\lambda}_l^*\equiv\boldsymbol{\lambda}_l-i\omega\boldsymbol{\eta}_\lambda$, where $\boldsymbol{\lambda}_l=\mathbf{K}_l-2\boldsymbol{\mu}_l/3$ is

the Lamé modulus, and $\boldsymbol{\eta}_{\lambda l} = \boldsymbol{\eta}_{Kl} - 2\boldsymbol{\eta}_{\mu l}/3$ is the corresponding viscosity. From equation (B.1c), the surface traction vector (used in boundary conditions in section 6.4 is also given by the stress tensor components $\boldsymbol{\sigma}_{zz}$ and $\boldsymbol{\sigma}_{zx}$.

When using secondary wave modes with $k_z = 0$, a different set of basis functions can be selected instead of equation (6.4):

$$\vec{\mathbf{u}}_m\left(t,\vec{r}\right) = \begin{cases} \mathbf{u}_m \vec{n}_m e^{-i\omega t + i\vec{k}\vec{r}} & \text{for } m = 1,\ 2,\ 5, \text{ or } 6, \\ \mathbf{u}_m \vec{n}_m & \text{for } m = 3 \text{ or } 7, \\ \mathbf{u}_m \vec{n}_m \hat{k} z & \text{for } m = 4 \text{ or } 8, \end{cases} \tag{B.2}$$

where the secondary modes contain only internal displacements: $\mathbf{u}_3 = \mathbf{u}_4 = \mathbf{u}_7 = \mathbf{u}_8 = \begin{pmatrix} 0 & 1 \end{pmatrix}^T$.

In these functions, the characteristic wavenumber $\hat{k}$ is used to achieve consistent dimensionality and comparable values of all components of $\vec{\mathbf{u}}_m$. This value is selected equal $\hat{k} = |k_z|$ for traveling waves. It can be easily seen that these functions for secondary waves satisfy equations (6.1) and (6.5) with $\vec{k} = \mathbf{0}$. Physically, basis functions $\vec{\mathbf{u}}_3$ and $\vec{\mathbf{u}}_4$ represent quasi-static deformations of the SLS with $\sigma_{Jij} = const$ for the internal variable (J = 2). Again similar to poroelasticity, such deformations are similar to changing fluid content within the entire layer, and $\dot{\vec{u}}_{mJ}$ (with J = 2) is the "flow" (velocity) of the internal variable. For their use in boundary conditions and reflection/transmission coefficients, I only need the displacements, strains, and stresses (equations (B.1)) for the modified basis functions. For m = 3 or 7, these modified observables are

$$\mathbf{U}_m^l(\vec{r}) = \begin{bmatrix} n_z\mathbf{u}_m \\ n_x\mathbf{u}_m \end{bmatrix}, \quad \mathbf{E}_m^l(\vec{r}) = \begin{bmatrix} 0 \\ 0 \\ 0 \end{bmatrix}, \quad \text{and} \quad \mathbf{\Sigma}_m^l(\vec{r}) = \begin{bmatrix} 0 \\ 0 \\ 0 \end{bmatrix}, \tag{B.3a}$$

and for m = 4 or 8:

$$\mathbf{U}_m^l(\vec{r}) = \begin{bmatrix} n_z z\mathbf{u}_m \\ n_x z\mathbf{u}_m \end{bmatrix}, \quad \mathbf{E}_m^l(\vec{r}) = \begin{bmatrix} n_z\mathbf{u}_m \\ \mathbf{0} \\ \frac{n_x}{2}\mathbf{u}_m \end{bmatrix}, \quad \text{and} \quad \mathbf{\Sigma}_m^l(\vec{r}) = \begin{bmatrix} n_z\mathbf{M}^*\mathbf{u}_m \\ n_z\boldsymbol{\lambda}^*\mathbf{u}_m \\ \frac{n_x}{2}\boldsymbol{\mu}^*\mathbf{u}_m \end{bmatrix}. \tag{B.3b}$$

The surface traction vector (used in boundary conditions) is also readily obtained by matrix product:

$$\begin{pmatrix} \boldsymbol{\tau}_z \\ \boldsymbol{\tau}_x \end{pmatrix}(\vec{r}) = \sum_{m=1}^{4N} \Theta_m^l(\vec{r})\psi_m^l, \quad \text{where} \quad \Theta_m^l = \begin{bmatrix} 1 & 0 & 0 \\ 0 & 0 & 1 \end{bmatrix}\mathbf{\Sigma}_m^l. \tag{B.4}$$

APPENDIX C

MATRIX INVERSE WITH CONSTRAINTS

In equations (6.26), matrix product $\mathbf{Y} = \mathbf{A}\big|_{\mathbf{C}}^{-1}\mathbf{B}$ is defined as a matrix satisfying relations $\mathbf{AY} = \mathbf{B}$ and $\mathbf{CY} = \mathbf{0}$ simultaneously, where matrix $\mathbf{A}$ may be non-square or singular. Rearranging the columns of matrices **B** and **Y** into single vectors, the constrained solution can be obtained by minimizing the following data error with respect to vector **Y**:

$$\Phi = \left(\mathbf{B} - \mathbf{AY}\right)^H \left(\mathbf{B} - \mathbf{AY}\right) + \boldsymbol{\lambda}^H \mathbf{CY}\,, \tag{C.1}$$

where $\boldsymbol{\lambda}$ is a vector of N_λ Lagrange multipliers, N_λ is the number of constraint equations (rows in matrix **C**), and '^{H}' denotes the Hermitian conjugate. Quantities $\boldsymbol{\lambda}$ can be viewed as unknowns, and the minimization equations $\partial\Phi/\partial\mathbf{Y} = \mathbf{0}$ and $\partial\Phi/\partial\boldsymbol{\lambda} = \mathbf{0}$ give

$$\mathbf{K}\begin{pmatrix} \mathbf{Y} \\ \boldsymbol{\lambda} \end{pmatrix} = \begin{pmatrix} \mathbf{A}^H\mathbf{B} \\ \mathbf{0}^{N_c \times 1} \end{pmatrix}, \tag{C.2}$$

where

$$\mathbf{K} \equiv \begin{bmatrix} \mathbf{A}^H\mathbf{A} & \mathbf{C}^T \\ \mathbf{C} & \mathbf{0}^{N_\lambda \times N_\lambda} \end{bmatrix} \tag{C.3}$$

should be an invertible square matrix, and notation $\mathbf{0}^{N\times M}$ denotes a zero matrix with N rows and M columns. From equation (C.2), the desired Y and the values of Lagrange multipliers $\boldsymbol{\lambda}$ are

$$\begin{pmatrix} \mathbf{Y} \\ \boldsymbol{\lambda} \end{pmatrix} = \mathbf{K}^{-1} \begin{pmatrix} \mathbf{A}^T\mathbf{B} \\ \mathbf{0}^{N_\lambda \times 1} \end{pmatrix}. \tag{C.4}$$